Forschungszentrum Jülich
in der Helmholtz-Gemeinschaft

Institut für Chemie und Dynamik der Geosphäre
Institut II: Troposphäre

Studies of Aldehydes in an Atmosphere Simulation Chamber

Jens Boßmeyer

Jül-4218

Studies of Aldehydes in an Atmosphere Simulation Chamber

Jens Boßmeyer

Berichte des Forschungszentrums Jülich ; 4218
ISSN 0944-2952
Institut für Chemie und Dynamik der Geosphäre
Institut II: Troposphäre Jül-4218
D 16 (Diss., Heidelberg, Univ., 2006)

Zu beziehen durch: Forschungszentrum Jülich GmbH · Zentralbibliothek, Verlag
D-52425 Jülich · Bundesrepublik Deutschland
☎ 02461 61-5220 · Telefax: 02461 61-6103 · e-mail: zb-publikation@fz-juelich.de

Abstract

In the course of this thesis, a DOAS instrument using a multiple reflection system of the White design was installed at the atmosphere simulation chamber SAPHIR (Forschungszentrum Jülich, Germany). The DOAS instrument allowed to detect NO_3 at SAPHIR for the first time. A loss process of NO_3 was identified in the dry chamber and characterised with a lifetime of (42±4) min. Apart from that, the chamber was used in three ways. (1) The DOAS could be compared to other detection methods under controlled conditions, which was done for the trace gases NO_2, O_3, $HONO$, H_2O, benzene and m-xylene. The agreement between DOAS and the other methods was very good (13 % maximum deviation in the absolute value, correlation coefficients higher than 0.92). (2) The DOAS could be compared to time profiles of trace gas injections (of benzaldehyde, toluene and $HCHO$) into the chamber, which were calculated from the sample weight and from fundamental chamber properties. The agreement between the DOAS and the calculations was also good (19 % maximum deviation, R higher than 0.94). Thus, the scaling of the differential absorption cross section of $HCHO$ used in the DOAS evaluations was confirmed. (3) Measurements of the DOAS and other instruments could be used to validate current chemistry models. The OH reactivity in the sunlit chamber was derived from DOAS measurements of benzene and m-xylene and matched a direct OH measurement excellently. Moreover, the $HCHO$ yield from the ethene-ozone reaction was studied. A discrepancy was observed between a model calculation and the measurement, which originated from the model assumptions made for kinetics of reaction intermediates in the ethene-ozone mechanism. Finally, absolute rate studies of the NO_3 reaction with ethanal (2.6±0.5), propanal (5.8±1.0), butanal (11.9±1.4) and benzaldehyde (2.2±0.6, all in cm^3s^{-1} at 300 K) corroborated the rate coefficients of current literature recommendations at near-ambient concentration levels. However, the measured yields of the product aldehydes in the NO_3 reactions with propanal and butanal disagreed with model calculations. This discrepancy originated from the model assumptions made for the kinetics of peroxyacyl nitrates in the degradation mechanism of the aldehydes.

Zusammenfassung

Im Zuge dieser Arbeit wurde ein DOAS-Instrument an der Atmosphären-Simulationskammer SAPHIR (Forschungszentrum Jülich) aufgebaut, das auf einem Vielfach-Reflektionssystem des White-Designs basiert. Das DOAS-Instrument ermöglichte erstmalig den Nachweis von NO_3 an der Kammer. Ein NO_3-Verlustprozess wurde in der trockenen Kammer beobachtet und mit einer Lebensdauer von (42±4) min charakterisiert. Davon abgesehen diente die Kammer für Experimente von dreierlei Art. (1) Das DOAS konnte unter kontrollierten Bedingungen mit anderen Nachweismethoden für die Spurengase NO_2, O_3, $HONO$, H_2O, Benzol und m-Xylol verglichen werden. Die Übereinstimmung des DOAS mit den anderen Methoden war sehr gut (Maximalabweichung 13 % im Absolutwert, Korrelationskoeffizienten größer als 0.92). (2) Das DOAS konnte mit Zeitreihen von Spurengaseingaben (von Benzaldehyd, Toluol and $HCHO$) in die Kammer verglichen werden, die auf Basis der Probenmenge und fundamentaler Kammereigenschaften berechnet wurden. Auch hier war die Übereinstimmung zwischen der Messung und den Berechnungen gut (Maximalabweichung 19 %, R größer als 0.94). Damit konnte die Skalierung des differentiellen Absorptionsquerschnittes von $HCHO$, der in der DOAS-Auswertung verwendet wird, bestätigt werden. (3) Messungen des DOAS und anderer Instrumente konnten zur Validierung aktueller Chemie-Modelle verwendet werden. Die OH-Reaktivität in der belichteten Kammer wurde aus DOAS-Messungen von Benzol und m-Xylol abgeleitet und stimmte hervorragend mit einer direkten OH-Messung überein. Weiterhin wurde die $HCHO$-Ausbeute in der Ethen-Ozon-Reaktion untersucht. Dies brachte eine Diskrepanz zwischen einer Modellrechnung und der Messung zutage, die auf Modellannahmen über kinetische Parameter von Zwischenprodukten im Ethen-Ozon-Mechanismus zurückgeführt wurde. Schließlich bestätigten Absolutbestimmungen der Reaktionskoeffizienten von NO_3-Reaktionen mit Ethanal (2.6±0.5), Propanal (5.8±1.0), Butanal (11.9±1.4) und Benzaldehyd (2.2±0.6, Angaben in cm^3s^{-1} bei 300 K) gegenwärtige Literaturempfehlungen für atmosphärische Bedingungen. Allerdings stimmten die gemessenen Ausbeuten von Produktaldehyden in den NO_3-Reaktionen mit Propanal und Butanal nicht mit Modellrechnungen überein. Dies wurde auf die Modellannahmen, die im Aldehyd-Abbaumechanismus über kinetische Parameter von Peroxyacyl-Nitraten gemacht wurden, zurückgeführt.

Contents

Chapter 1

Introduction

Main constituents of the dry atmosphere are molecular nitrogen ($\approx$ 78 %), molecular oxygen ($\approx$ 21 %) and the noble gas Argon ($\approx$ 1 %). Other compounds exist in traces of sometimes much less than 1000 parts per million air molecules, which have a great impact on atmospheric chemistry by their specific photochemical behaviour. The spatial distribution of trace gases in the atmosphere is not homogeneous, but reflects patterns of sources and sinks, which are often closely connected to the structure of the Earth's surface. Human impact on the atmosphere is particularly high in the boundary layer (up to 1 km above ground), where men, animals and plants are directly affected by changes in its composition. Therefore, tropospheric air chemistry studies gained more and more attention in the last decades. Some species like hydroxyl radicals (OH) or nitrate radicals ($\mathrm{NO_3}$) are highly reactive and show a distinct diurnal and nocturnal activity pattern. Other compounds like ozone ($\mathrm{O_3}$) are produced excessively in the boundary layer due to the photochemical processing of anthropogenically emitted species and have adverse effects on living organisms, with Los Angeles smog events being prominent examples [Finlayson-Pitts and Pitts 00].
Trace gas measurements in the field are used to determine the chemical and meteorological processes that govern air composition. These measurements are also used to validate numerical chemistry-transport-models, which, when available with sufficient accuracy, yield a picture of the composition of the atmosphere with comparatively low experimental effort. To the present day, the interpretation of field data by chemistry models often turns out to be difficult, since field measurements are usually affected by, for example, the movement of air parcels or the existence of local sources of gaseous species that are hard to account for. In order to obtain a profound understanding of pure chemical mechanisms, it is desirable to decouple them from all perturbations being possible only under controlled conditions in the laboratory. For that purpose, from the 1970ies on many smog chamber facilities were erected as photochemical reactors. According to *McNaught and Wilkinson* [97] a smog chamber is defined as a

> *large confined volume, in which sunlight or simulated sunlight is allowed to irradiate air mixtures of atmospheric trace gases (hydrocarbons, nitrogen oxides, sulfur dioxide, etc) which undergo oxidation.*

Due to the interaction of gas and condensed phase, most smog chamber studies are performed at reactant concentrations much higher than typically found in the atmosphere. However, at high non-natural concentrations in a gas volume processes like self reactions of molecules gain a relevance they would not have otherwise making the translation of the results of such studies to other concentration regimes questionable.
The atmosphere simulation chamber SAPHIR being operated on the campus of the Forschungszentrum Jülich since September 2000 was designed to perform chemical studies under typical tropospheric conditions including the exposure to daylight. Since first operation detection methods at SAPHIR have been improved and extended continuously. As part of this thesis, a differential optical absorption spectrometer (DOAS) was added to the SAPHIR set-up extending the list of observable compounds at the chamber. DOAS measurements of several trace gases were compared to, for one, data recorded concurrently by other detection methods, and, for another, to data calculated from basic properties of the simulation chamber. Furthermore, chemical systems were studied to verify the current state of knowledge of atmospheric chemistry.

Guide to this Thesis

In the following the main content of this thesis is outlined. In Chapter 2, the theoretical background of this thesis is presented. Differential optical absorption spectroscopy is the detection method, which was used to identify and quantify trace gases. Section 2.1 covers the mathematical basics of the DOAS method, particularly the Beer-Lambert law in section 2.1.1. Furthermore, sections 2.1.2 and 2.1.3 demonstrate how measured spectral data are corrected for background signals and how information of kind and abundance of an absorber is extracted. Experimental data are endowed with an accuracy, which defines their quality. Considerations how the accuracy of the DOAS retrieval is estimated are depicted in section 2.1.4. Sections 2.2.1, 2.2.2 and 2.2.3 address aspects of atmospheric chemistry that are the basics of the experimental works depicted in Chapter 5. First, the chemistry of aldehydes in the atmosphere is outlined (section 2.2.1). Although being emitted primarily, the main source of aldehydes is constituted by photochemical degradation of organic precursors. Formaldehyde ($HCHO$), the smallest and most abundant of the aldehydes, is generated in alkene-ozone reactions with high product yields. As a rather small molecule the shortest alkene, ethene (C_2H_4), provides chemical reaction pathways, which can be followed comparatively easy. Section 2.2.2

outlines the degradation paths and products that are expected in ethene degradation by O_3. Accepting the chemical simplicity, ethene is particularly suited to investigate the consistency of numerical chemistry models with experimentally recorded data. Therefore, model calculations of the ethene-ozone reaction making predictions about the yield of the carbonyl product $HCHO$ are presented. The last aspect of tropospheric chemistry treats NO_3 radicals (section 2.2.3). Although being overshadowed by O_3 and OH, NO_3 contributes a great part to the oxidising capacity of the atmosphere during nighttime. With the construction of a DOAS instrument during this thesis the requirement for NO_3 radical detection at the SAPHIR chamber was accomplished for the first time.
The experimental part of this thesis was performed exclusively at the atmosphere simulation chamber SAPHIR of the Forschungszentrum Jülich. SAPHIR is particularly convenient to study chemical systems under standard atmospheric conditions. Chapter 3 gives a technical description of SAPHIR and treats effects like dilution, the mixing characteristics, chamber sources of chemical compounds investigated to date and the instrumentation used to monitor relevant chemical and meteorological parameters.
Nowadays, the DOAS technique is acknowledged as one of the main working horses in generating data sets for use in atmospheric research. DOAS set-ups have been implemented in numerous ways, one of which utilises multiple reflection systems. Chapter 4 sums up the details of the DOAS instrument at SAPHIR, which was constructed in the course of this work. The characterisation of the newly established instrument is presented in section 4.5.
In Chapter 5 results of the experiments conducted for this thesis are discussed. After construction of the DOAS instrumental set-up at SAPHIR had been finished in spring 2004, experiments were performed aiming to compare the newly established DOAS to other already existing instruments towards NO_2, $HONO$, O_3 and H_2O (section 5.1). In 2005 two international intercomparison campaigns were carried out at SAPHIR to assess the quality of trace gas measurements with different techniques. The first dealt with oxygenated volatile organic compounds (OVOC campaign, section 5.2). The second covered hydrogen oxide radicals (HO_xCOMP). Not being able to detect the radicals directly the DOAS instrument provided valuable support data, from which an average OH concentration was derived (section 5.3). Extensive comparison studies of $HCHO$ using three instruments capable of $HCHO$ detection were carried out at SAPHIR (section 5.4). The way of the generation of gaseous $HCHO$ was investigated. One approach was to generate $HCHO$ by thermolysis of solid para-formaldehyde (section 5.4.1). Furthermore, the supposedly complete and accurate model of ethene oxidation exemplified the perspectives that chamber studies offer for the understanding of gas-phase kinetics. For that purpose, $HCHO$ was generated by the ethene-ozone reaction (section 5.4.2). Since operation of SAPHIR started in the year 2000, the newly built DOAS instrument allowed the

detection of highly reactive NO_3 radicals in the SAPHIR chamber for the first time. In section 5.5 the characteristic behaviour of NO_3 at SAPHIR is presented in two examples, one is a sink in the chamber (section 5.5.1), the other is the effect of atmospheric stray light reaching the interior of the chamber with closed shutters during daylight hours (section 5.5.2). The ability of measuring nitrate radicals allowed to study aldehyde chemistry in presence of NO_3 (section 5.6). At SAPHIR absolute rate studies of NO_3-aldehyde reactions with 4 aldehydes under near-atmospheric conditions (section 5.6.1) were performed. Furthermore, section 5.6.2 presents an analysis of product yields in the propanal-NO_3 and butanal-NO_3 experiments in comparison to model calculations based on the Master Chemical Mechanism (MCM) and outlines possible consequences for the assumptions in atmospheric chemistry models and for sampling detection methods.

Chapter 2

Fundamentals

This chapter presents the theoretical background of this work. In all experiments described in this thesis the DOAS method was involved. Therefore, in the first part the DOAS method is described. In the second section the relevance of trace gases in the atmosphere, which were investigated in this work, will be reviewed.

2.1 Differential Optical Absorption Spectroscopy

Differential optical absorption spectroscopy is a widely and successfully used remote sensing technique in order to detect chemical species, which exist in traces in the atmosphere [Platt 00]. DOAS is based on the wavelength dependent absorption of light by matter. The DOAS technique is a powerful tool, since its principle depends essentially only on the knowledge of the absorption cross section of a chemical species, which is a fundamental characteristic. It does not require periodical calibrations, which introduce additional uncertainties. Furthermore, it provides high selectivity, which reduces the effect of interferences with other present species. Achievements of the DOAS technique obtained in field measurements include among others the first direct detection of nitrous acid [Perner and Platt 79] as well as nitrate radicals [Platt et al 80] in ambient air, and more recently water dimers on a coastal side [Pfeilsticker et al 03], and bromine oxide emitted from volcanoes [Bobrowski et al 03]. The list of detectable compounds encompasses several hydrocarbons (eg $HCHO$, benzaldehyde), nitrogen (eg NO_2, $HONO$, NO_3) and halogen (eg BrO, IO, ClO) compounds. The mathematical background and the practical application are described in the following.

2.1.1 The Beer-Lambert Law

Light with an initial intensity $I_0(\lambda, l = 0)$ emitted by a suitable light source, eg a Xenon short arc lamp, passes through an air mass and is finally collected by a telescope. On the light path the initial light intensity is reduced by extinction processes like scattering and absorption. Scattering can be classified in two processes. Rayleigh scattering describes the scattering of photons on particles, the spatial dimension of which is smaller than the wavelength of the light. The Rayleigh scattering cross section depends strongly on the wavelength ($\propto \lambda^{-4}$). Mie scattering describes the scattering of photons on particles, which roughly have the same dimension as the wavelength of the light (ranging from $\propto \lambda^{-1}$ to λ^{-3} depending on the kind of particles). After a light path L, the Beer-Lambert law provides the observed light intensity for a set of given absorbers, where all structures are superposed.

$$I(\lambda, L) = \tag{2.1}$$
$$I_0(\lambda) \times \exp\left(-\sum_i \int_0^L \left(\sigma_{tot,i}(\lambda, p, T) \times c_i(l) + \varepsilon_{\mathrm{R}}(\lambda, l) + \varepsilon_{\mathrm{M}}(\lambda, l)\right) dl\right)$$

σ represents the absorption cross section of atmospheric molecules in cm^2, which is basically dependent on wavelength, temperature and pressure. Due to its weakness the latter dependency is usually neglected. c is the number density in cm^{-3} at position l of the total light path L in cm. ε_{R} and ε_{M} stand for the Rayleigh and Mie scattering coefficients in cm^{-1}, respectively.

The concentration of an absorber can be computed on an absolute scale by measuring the optical density, which is defined as the ratio of the observed to the initial intensity,

$$\tau(\lambda) = -\ln\left(\frac{I(\lambda)}{I_0(\lambda)}\right) \tag{2.2}$$

if it were not for the lack of knowledge about the scattering parameters mentioned above and the number of present absorbers. An additional, common obstacle of spectroscopic applications is that the initial intensity is not known. The DOAS method circumvents these obstacles by dividing the total absorption cross section σ in a high (σ') and low frequency (σ^b) part (Figure 2.1).

$$\sigma_{\mathrm{tot}}(\lambda, T) = \sigma^{\mathrm{b}}(\lambda, T) + \sigma'(\lambda, T) \tag{2.3}$$

As scattering processes cause mainly broadband spectral features, their contribution to the spectral signature is now gathered in σ^{b}. With

$$I_0'(\lambda) = I_0(\lambda) \times \exp\left(-\sum_i \int_0^L \left(\sigma_i^b(\lambda, p, T) \times c_i(l) + \varepsilon_{\mathrm{R}}(\lambda, l) + \varepsilon_{\mathrm{M}}(\lambda, l)\right) dl\right) \tag{2.4}$$

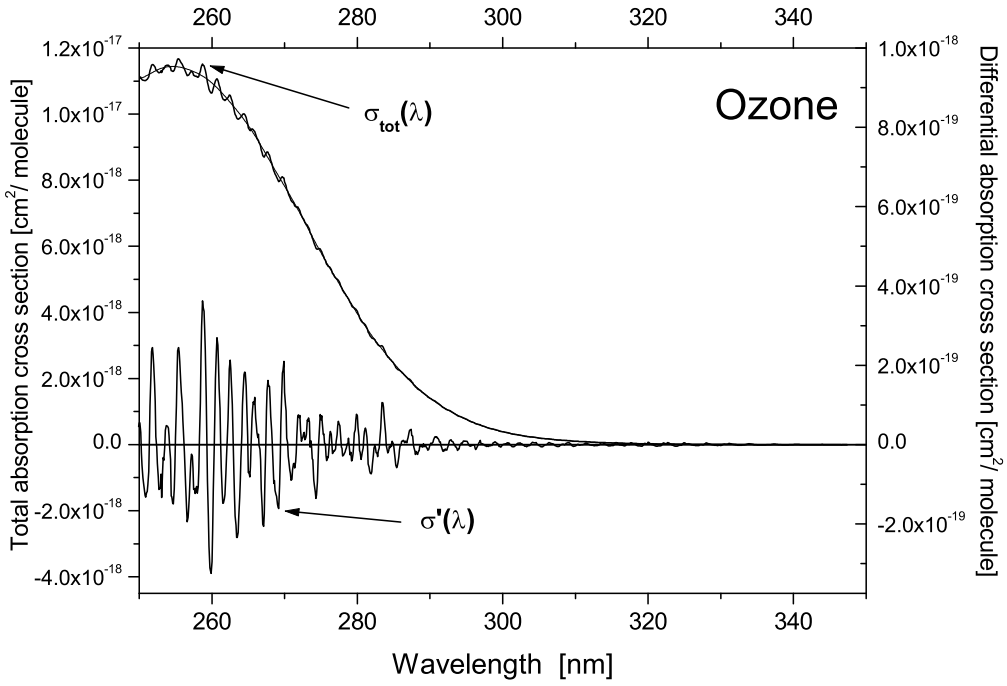

Figure 2.1: *Total ozone absorption cross section σ_{tot} as well as its broadband (σ^{b}) and differential (σ') parts.*

equation (2.1) is rearranged to

$$I(\lambda, L) = I'_0(\lambda) \times \exp\left(-\sum_i \int_0^L \sigma'_i(\lambda, T) \times c_i(l) \times dl\right) \tag{2.5}$$

Introducing the differential optical density

$$\tau'_{\mathrm{tot}}(\lambda) = -\ln\left(\frac{I(\lambda)}{I'_0(\lambda)}\right) \tag{2.6}$$

the concentration is calculated, whereby the possible different absorptions are separated.

$$\tau'_{\mathrm{tot}}(\lambda) = \sum_i \left(\int_0^L c_i(l) \times \sigma'_i(\lambda, T) \times dl\right) \tag{2.7}$$

$$\overline{c_i} = \frac{\tau'_i(\lambda)}{L \times \sigma'_i(\lambda, T)} \tag{2.8}$$

In equation (2.8) the integral was suspended, which means that the actual optical density obtained describes the average concentration ($\overline{c_i}$) along the light path L. As τ' is extracted from the spectrum and the path length is known very precisely in most cases, the only parameter that has to be provided is the differential absorption cross section. It is normally taken from the literature.

2.1.2 Background Correction

Photo diode arrays (PDAs with for example 512, 1024 or 2048 elements) are commonly used as light detectors in DOAS applications [Stutz 96]. During operation a voltage is applied to the diodes, which work as charged condensors with a capacity of several pF. When photons hit a diode, it is discharged by internal photoeffect. During the read out of a diode the missing charge is added by a charge sensitive preamplifier. The charge to reconstitute the initial voltage is proportional to the number of incoming photons and hence to the integral of the intensity over the integration time period.
PDAs possess two kinds of electronic background signals. For one, to every preamplified and integrated diode signal a positive offset voltage is added to avoid problems in the conversion from an analog into a digital signal, which could occur in low intensity measurements due to noise minima. For another, thermal excitation causes electron transitions in the diodes leading to a slow, temperature-dependent self discharge. Recorded spectra must be corrected for these two electronic background signals prior to the DOAS evaluation.
Another background signal in spectra measured by a multi-element PDA arises, because neither the individual pixel dimension nor the electronic pixel characteristics are homogeneous over an array of several hundred elements. These inhomogeneities of the pixels cause spectral structures, which could be mistaken for narrow-band absorptions of trace gases, and can amount to as much as 10^{-2} exceeding optical densities down to the order of 10^{-4}, which shall be detectable.
Mathematically described, a measured intensity spectrum looks like (no noise is considered here)

$$I = I_0 \times \exp(-\tau') \times P \times S_{\mathrm{P}} + B_{\mathrm{E}} + I_{\mathrm{S}}. \tag{2.9}$$

Here I_{S} denotes possible stray light. Stray light is mentioned here for completeness and will be described in more detail in section 4.5.3. B_{E} represents the electronic background, S_{P} the pixel inhomogeneity, P the broadband extinction due to Rayleigh-Mie scattering and the broadband absorption, τ' the differential optical density of narrow-band absorption (equation (2.7)) and I_0 the initial smooth intensity.
The common approach to account for the pixel inhomogeneity is to reference all measured spectra to a null spectrum, which contains no or negligible narrow-band trace gas signatures. Basically, the same contributions as in equation (2.9) appear in such a reference spectrum.

$$I_{\mathrm{ref}} = I_{0,\mathrm{ref}} \times \exp(-\tau'_{\mathrm{ref}}) \times P_{\mathrm{ref}} \times S_{\mathrm{P}} + B_{\mathrm{E}} + I_{\mathrm{S}}. \tag{2.10}$$

The mathematical procedure of spectra processing is shown in the following. First, electronic background and stray light, quantified in characteri-

sation experiments, are removed by subtraction.

$$I_{\text{corr}} = I_0 \times \exp(-\tau') \times P \times S_{\text{P}} \quad (2.11)$$

$$I_{\text{ref,corr}} = I_{0,\text{ref}} \times \exp(-\tau'_{\text{ref}}) \times P_{\text{ref}} \times S_{\text{P}} \quad (2.12)$$

Dividing the two equations removes the pixel inhomogeneity. Taking the logarithm yields

$$\ln\left(\frac{I_{\text{ref,corr}}}{I_{\text{corr}}}\right) = \ln\left(\frac{I_{0,\text{ref}}}{I_0}\right) + \tau' - \tau'_{\text{ref}} + \ln\left(\frac{P_{\text{ref}}}{P}\right). \quad (2.13)$$

The first term on the righthand side equals zero, since reference as well as measurement were taken using the same smooth light source. Any discrepancies between the initial intensities are accounted for with the last term on the righthand side. It represents the broadband extinction and is removed before the spectral fit by high-pass filtering. Hence, only the actual corrected measured signal remained on the left-hand side of the equation and the difference of narrow-band absorption in measurement and reference on the righthand side. Equation (2.13) contains the difference of differential optical density in measurement and reference spectrum $\tau' - \tau'_{\text{ref}}$. Therefore, the real differential optical density could be underestimated if the reference contained any absorption signature.
In order to obtain a reference spectrum, several methods have been suggested. One is a short cut system guiding the light from source to detector directly using a light path much shorter than in the real measurement. As L in equation (2.7) is very small, the effect of absorption will be small as well. Another way, which is applicable only with folded path systems, is to frequently alternate the light path length, eg from 960 to 320 m, so that an effective path length results from the subtraction of the two, 640 m in this example. Furthermore, the reference can be obtained by taking many spectra at slightly different wavelength-to-pixel mappings. Adding up these spectra as they are smoothes all narrow-band absorptions leaving only the instrumental characteristics. The actual analysis spectra are generated by shifting all spectra back to a common dispersion [Brauers et al 95].
A fourth way, which is only applicable under laboratory conditions (as provided by an atmosphere simulation chamber, cf Chapter 3), is to record a set of spectra in a clean atmosphere. In this thesis, a slight variation of the last method was used. The electronic background varies slightly with time leading to a degradation of the signal-to-noise ratio the further the measurements proceed from the time of the reference record. To mitigate this effect, whenever possible, all of the spectra taken during a measurement were added and used as reference. The resulting concentration-time profile was then zeroed on a measurement period, when the concentration of trace gases could be assumed negligible.

2.1.3 The Analysis Procedure

The analysis procedure of the DOAS method is based on fitting a modelled to a measured spectrum. The measured spectrum consists of light that was dispersed in the spectrograph and then projected onto the light detector, which is divided into an array of discrete picture elements.
According to *Stutz and Platt* [96] a function $F(i)$ is compiled in order to model the logarithm of the discrete measured intensity $J(i)$ (i being the pixel index)

$$F(i) = P_{\mathrm{r}}(i) + \sum_{j=1}^{m} a_j \times U_j(d_{j,0}, d_{j,1}, \dots)(i) \tag{2.14}$$

Input data to the procedure (U_j) are the absorption cross sections of the trace gases, eg taken from the literature. m represents the number of considered absorbers and the $d_{j,k}$ (k=1,2,3 ...) stand for the spectral alignment parameters containing the wavelength-to-pixel mapping. The scaling factors a_j are the results of the fit and represent the product $\tau_i' \times \sigma_i'^{-1}$, so that concentrations are computed simply by dividing the a_j's by the path length L, as indicated by equation (2.7).
The polynomial $P_{\mathrm{r}}(i)$ reflects the broadband structures found in a spectrum, due to eg Mie and Rayleigh scattering, the spectral sensitivity, and the broadband absorptions. It is the numerical representation of $I_0'(\lambda)$ (cf equation (2.4)).

$$P_{\mathrm{r}}(i) = \sum_{h=0}^{\gamma} c_h \times (i - i_{\mathrm{c}})^h \tag{2.15}$$

The parameter i_{c} represents the centre pixel of the spectral region. The scaling parameters a_j and the polynomial coefficients c_h are determined by fitting F to J linearly.
The analysis procedure aligns the cross section spectra $U_j(i)$ to the spectrum $J(i)$. Therefore, the procedure has to recalculate the cross section spectrum $U_j^*(i)$ using the wavelength-to-pixel mapping of the measured spectrum. This can be regarded as a shifting and stretching of the cross section spectrum in wavelength space using a cubic spline interpolation. Once the cross sections are aligned the actual analysis procedure is initiated. It is a combination of the Levenberg-Marquardt method that determines the $d_{j,k}$s and a linear least squares fit to derive the a_js and the c_ks. Both methods aim to minimise

$$\chi^2 = \sum_{i=i_{\mathrm{down}}}^{i_{\mathrm{up}}} [J(i) - F(i)]^2 \tag{2.16}$$

As mentioned above $J(i)$ is the measured spectrum at pixel position i and $F(i)$ the corresponding entry of the model spectrum. In order to gain a proper fit all possible absorption structures have to be accounted for beforehand, as missing absorbers would lead to enhanced fit residuals. Generally,

the procedure starts the calculation of the linear fit with initial values $d_{j,k}$. The results of this fit are used as input data in the following call of the non-linear Levenberg-Marquardt fit [Levenberg 44, Marquardt 63], which then performs one iteration only. Its results are used as input for the next call of the linear fitting method, which results are then re-fed into the non-linear fit etc. Thus, the alternating calls of each method are repeated as long as the stopping conditions are not fulfilled. Usually, the fit is stopped when the relative changes of χ^2 are lower than 10^{-4} indicating that the fit has converged. The fit is also interrupted if a specified number of iterations is exceeded or the non-linear fit becomes unstable.
For this kind of spectral analysis several programs exist, with which the mathematical procedures can be executed, eg MFC [Gomer et al 93] or WinDoas [Fayt and Roozendael 01]. Some of them are capable of recording spectra and can be operated from a script mode, which allows the adaptation of spectra recording, handling and fitting to specific needs. As it provides all features mentioned above, the software DOASIS * being developed at the Institut für Umweltphysik, University of Heidelberg, by Stefan Kraus was used in this thesis [Kraus and Geyer 01].

2.1.4 Error Estimation

During the DOAS evaluation the numerical fitting error is determined from the root mean square (RMS) of the residual. The residual reflects those structures in a spectrum that could not be described by the modelled spectrum. It basically depends on the instrumental noise and does not change significantly with time. In theory, the RMS of the residual reflects a confidence level of 68.4 % (1σ) and is responsible for the scatter of individual data points around a trend line. The amplitude of the scatter is represented by the residual only assuming that it consists of normally distributed noise. For the kind of instrumental set-up used here (cf Chapter 4) this assumption is not fulfilled [Stutz 96]. In order to estimate the measurement error correctly, the relation between numerical fitting error and data scatter was determined. The data scatter was calculated by high-pass filtering measured concentration-time profiles of HCHO and $\mathrm{O_3}$. The RMS of the data point scatter around the corresponding trend line in a given time interval was compared to the average numerical fitting error in the same range. The RMS exceeded the average fitting error consistently by a factor of two. Therefore, the estimated standard deviation of a data point given in this thesis is double the numerical error of the fit.
Apart from the error of the numerical fitting, which represents the precision of a measurement and is a statistically varying parameter, other sources can add systematic errors to the overall uncertainty (accuracy).

*Available at *http://www.iup.uni-heidelberg.de/bugtracker/projects/doasis/*

Table 2.1: *DOAS retrieval settings at SAPHIR. All species detected at a total path of 960 m (except the aromatics at 320 m; BENZAL: benzaldehyde, TOL: toluene, BENZ: benzene, MXYL: m-xylene).*

SPECIES	RANGE [nm]	CROSS SECTION, σ	ERR. [a] [%]	LOD [b] [ppbv]
Light path: 960 m				
NO_2	422–448	[Voigt et al 02]	2.7	0.6
O_3	313–330	[Voigt et al 01]	3.7	10
H_2O	625–699 [c]	[Rothman et al 05]	na	2×10^5
HONO	340–376	[Stutz et al 00]	5	0.3
HCHO	312–348	[Meller and Moortgat 00]	5	1
NO_3	617–670	[Sander 86]	15	0.02
Light path: 320 m				
BENZAL	273–286	[Etzkorn et al 99]	4.6	0.1
TOL	265–273	[Etzkorn et al 99]	2.7	1
BENZ	252–275	[Etzkorn et al 99]	7.2	0.36
MXYL	252–275	[Etzkorn et al 99]	3.5	0.28

[a] Of σ as stated in the reference
[b] Limit of detection, 95 % confidence limit
[c] Omitting the range from 668 to 692 nm to exclude an O_2-B band

One of these is the accuracy of the absorption cross sections. Typical accuracies amount to several percent (eg 4 % for the O_3 or 3 % for the NO_2 cross sections that were used in this thesis [Voigt et al 01, Voigt et al 02]). Another, albeit minor, error source using cross sections is their unrestricted validity only at certain temperatures (T) and pressures (p), which do not necessarily match atmospheric conditions of the current measurement. The stronger σ depends on T and p, the larger the contribution to the error will be. Other error contributions, caused by the instrumental set-up, and how these are considered in the analysis is discussed in section 4.5.5.

2.1.5 Processing Spectra

All DOAS evaluations performed during this thesis followed the same scheme. The recorded spectra were assigned a dispersion, which was determined using Hg emission lines. Hg peaks also served as instrument functions in order to adapt the high resolution literature cross sections to the resolution of the instrument. Measurement spectra were corrected for electronic background, pixel inhomogeneity and stray light (the latter when required). Finally, the fit was applied to a high-pass-filtered measurement

spectrum. A stretching of the cross sections during the fit was generally not included, since the instrument function was known very accurately. Shifting of the cross sections towards the measurement spectrum was allowed, limited to a range of several pixels to account for uncertainties in the wavelength-to-pixel mapping and slight drifts in the wavelength setting during the measurement period. As the wavelength calibration of literature cross sections can be assumed quite accurate, the optimum shift was applied to all absorbers simultaneously. Table 2.1 summarises the DOAS retrieval settings for compounds measured in the course of this thesis. Finally, Figures 2.2, 2.3 and 2.4 present examples of DOAS fits in wavelength intervals used in this thesis. The upper panel shows the measured spectrum already corrected for electronic background and pixel inhomogeneity.

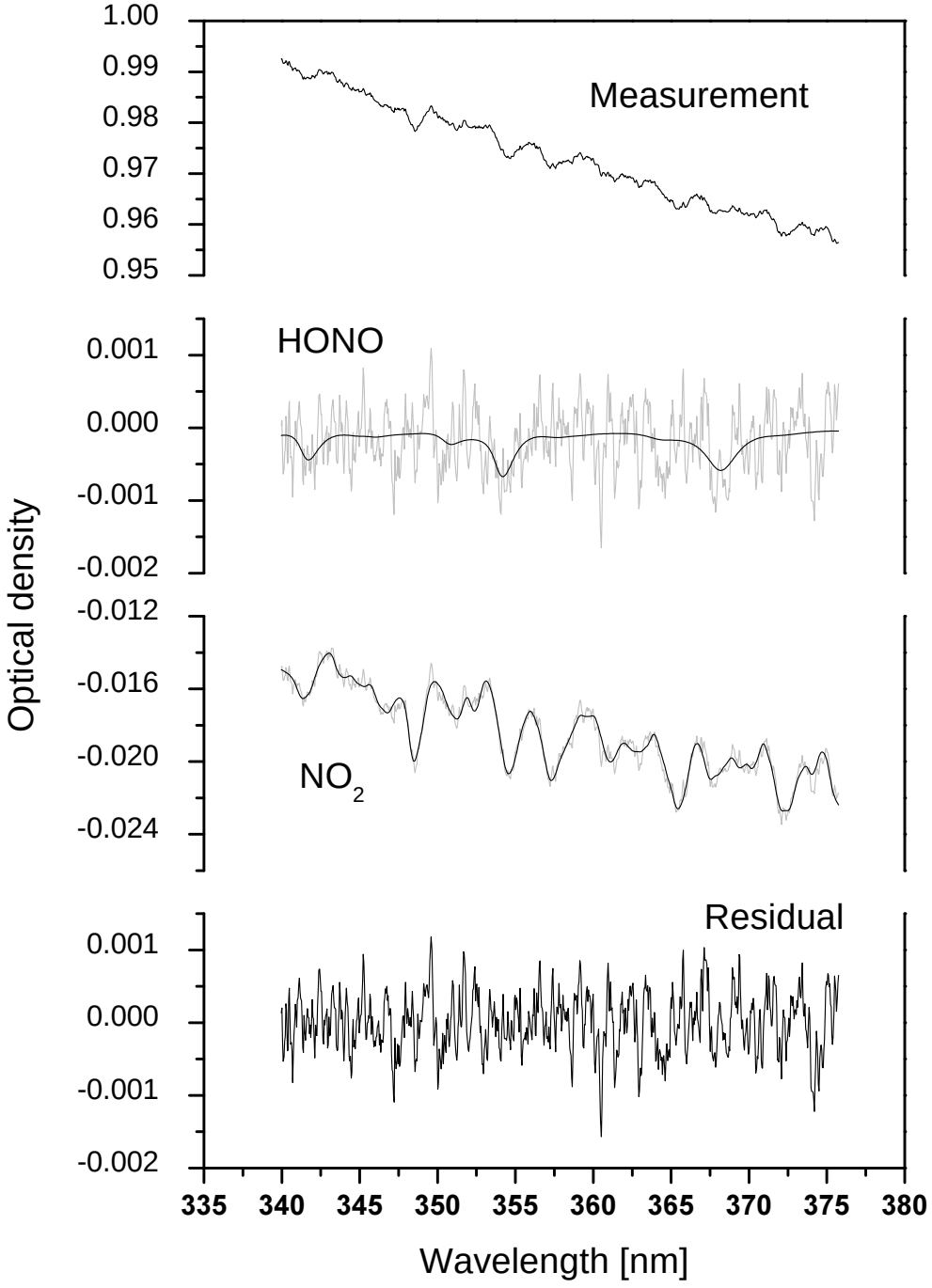

Figure 2.2: *Sample fit of HONO and NO_2 (black line: best fit). Spectrum recorded on 16 Jun 2004 at 16:37 UTC. The root mean square of the residual is 4×10^{-4}. The observed absorptions correspond to 0.5 ppbv (HONO) and 15 ppbv (NO_2). O_3 concentrations were not sufficient to be detected in that range.*

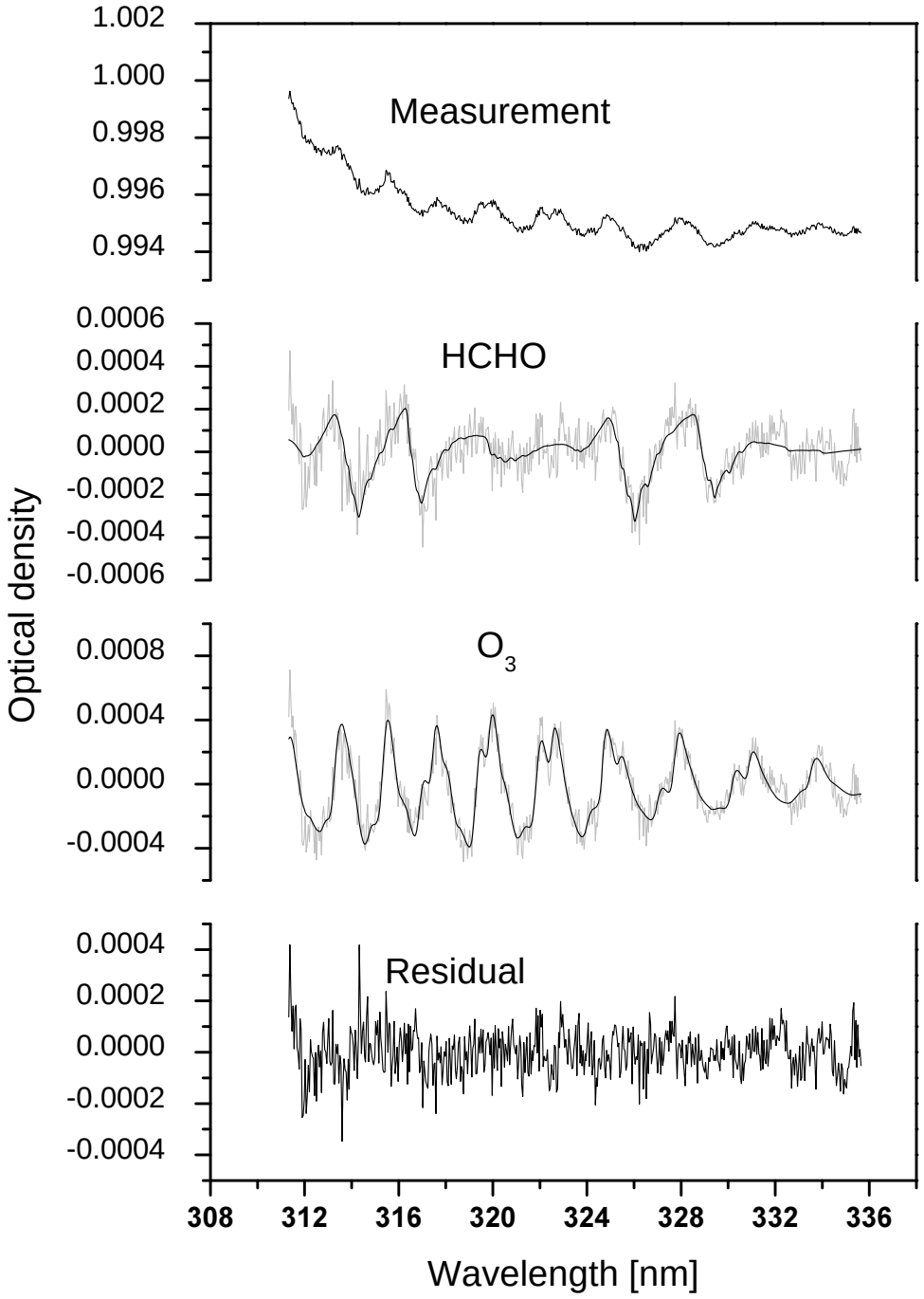

Figure 2.3: *Sample fit of HCHO and O_3. Spectrum recorded on 16 Feb 2005 at 11:38 UTC. RMS (residual) = 9×10^{-5}. Absorptions: 3.3 ppbv (HCHO), 34 ppbv (O_3).*

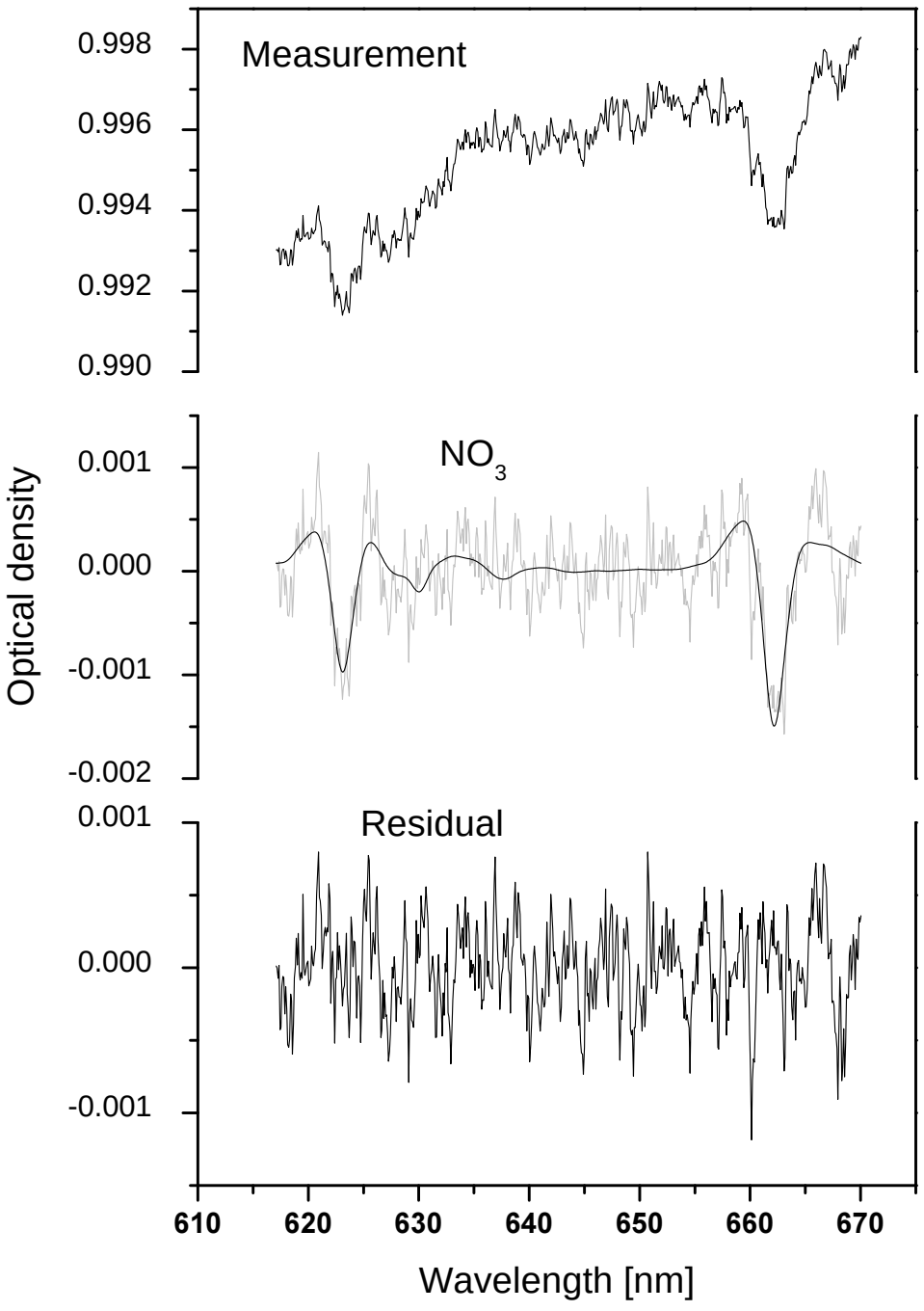

Figure 2.4: *Sample fit of NO_3. Spectrum recorded on 8 Sep 2005 at 13:57 UTC. RMS (residual) = 3×10^{-4}. Absorption: 70 pptv (NO_3). NO_2, H_2O and Fraunhofer structures were not strong enough to be observed in that range.*

2.2 Gas-Phase Chemistry of Selected Compounds

2.2.1 Aldehydes

Aldehydes are emitted by a variety of sources. They arise from incomplete fossil fuel combustion, are emitted by vegetation and are produced during biomass burning as well as photochemical oxidation of volatile hydrocarbons [Carlier et al 86]. The more carbon atoms an aldehyde contains, the less abundant it generally is in the atmosphere. Peak mixing ratios of formaldehyde, acetaldehyde, propionaldehyde, butyraldehyde and benzaldehyde can reach 60 ppbv, 18 ppbv, 3 ppbv, 1.4 ppbv and 1 ppbv in urban air, respectively [Finlayson-Pitts and Pitts 00]. As precursors of hydroperoxy radicals (HO_2) and peroxyacyl nitrates the two shortest aliphatic aldehydes, formaldehyde and acetaldehyde, are of particular interest for atmospheric research. The smallest and most abundant of the peroxyacyl nitrates, peroxyacetyl nitrate (PAN), is infamous for its adverse effects on man as well as plant health and was recognised as reservoir compound for NO_x (the sum of NO and NO_2).
The fate of aldehydes is governed by two reaction paths during daytime [Seinfeld and Pandis 97]. For one, they are photolysed. Two photolysis paths were observed for $HCHO$.

$$HCHO + h\nu \xrightarrow{45\%} H + HCO \tag{2.17a}$$

$$\xrightarrow{55\%} H_2 + CO \tag{2.17b}$$

The stated branching ratios for $HCHO$ photolysis are valid for clear sky and overhead sun conditions. The threshold wavelengths for reactions (2.17a) and (2.17b) are approximately 330 and 360 nm, respectively. Aldehydes containing more than one carbon atom are split into a formyl (HCO) and an alkyl radical (R, eg CH_3, C_2H_5).

$$RCHO + h\nu \longrightarrow HCO + R \tag{2.18}$$

These radicals recombine rapidly with molecular oxygen to yield alkyl peroxy radicals (RO_2), hydroperoxy radicals and carbon oxide (CO).

$$R + O_2 \xrightarrow{M} RO_2 \tag{2.19}$$

$$H + O_2 \xrightarrow{M} HO_2 \tag{2.20}$$

$$HCO + O_2 \longrightarrow HO_2 + CO \tag{2.21}$$

Consequently, aldehyde photolysis is a significant source of hydroperoxy radicals in the atmosphere. The HO_2 yield is unity, even for $HCHO$ photolysis regarding the equally sized branching ratios of the two paths (reactions

Table 2.2: *Rate coefficients (in $cm^3\ s^{-1}$) of reactions of 5 aldehydes with OH and NO_3 radicals (concentrations: $5\times10^8\ cm^{-3}$ NO_3, mean global average [Finlayson-Pitts and Pitts 00], and $1.6\times10^6\ cm^{-3}$ OH, 12 hour daytime average [Seinfeld and Pandis 97]) and corresponding lifetimes (in days) at 288 K. All coefficients taken from* IUPAC *[05] except benzaldehyde-NO_3 [Atkinson 91] and benzaldehyde-OH [Atkinson 86]. Photolysis frequencies (in s^{-1}) and corresponding lifetimes (in days) derived for a clear sky solar zenith angle of 45° from photochemical data given in* Jenkin et al *[97].*

RATE COEFF. LIFETIME	HCHO	CH_3CHO	C_2H_5CHO	C_3H_7CHO	C_6H_5CHO
k_{OH} [10^{-11}]	0.9	1.6	2.1	2.5	1.3
τ_{OH}	0.8	0.5	0.3	0.3	0.6
k_{NO_3} [10^{-15}]	0.6	2.2	6.5	9.4	2.6
τ_{NO_3}	39	11	3.6	2.5	9
$J_{h\nu}$ [10^{-5}]	5.9	0.3	1.3	2.1	1.3
$\tau_{h\nu}$	0.2	4.3	0.9	0.6	0.9

(2.17a) and (2.17b)). In presence of NO, the reaction of HO_2 and NO leads to the formation of highly reactive OH radicals

$$HO_2 + NO \longrightarrow OH + NO_2 \tag{2.22}$$

and also increases the production of O_3 when the product NO_2 is photolysed. Another daytime sink is the reaction with OH radicals, which proceeds via hydrogen atom abstraction, finally forming hydroperoxy and acyl peroxy radicals (RCO_3).

$$HCHO + OH + O_2 \longrightarrow HO_2 + CO + H_2O \tag{2.23}$$
$$RCHO + OH + O_2 \longrightarrow RCO_3 + H_2O \tag{2.24}$$

As efficient precursors of the oxidising agents O_3 and OH radicals aldehydes play a key role for the oxidising capacity of the atmosphere.
During nighttime, reaction with NO_3 radicals constitutes the main sink of aldehydes. However, the overall effect on the atmospheric aldehyde budget is rather small. Table 2.2 presents aldehyde lifetimes towards the NO_3 and OH reactions and a typical photolysis frequency. During summer season, when degradation by NO_3 radicals is not very efficient and other sinks only occur during daytime, $HCHO$ levels usually rise during the night, just to be degraded at dawn by photolysis and reaction with OH. The degradation path via NO_3 radicals resembles the hydrogen atom abstraction of the OH radicals [D'Anna and Nielsen 97]. Acyl radicals [†] are produced, which

[†]Formyl radicals in case of $R = H$, cf reactions (2.17a) and (2.21)

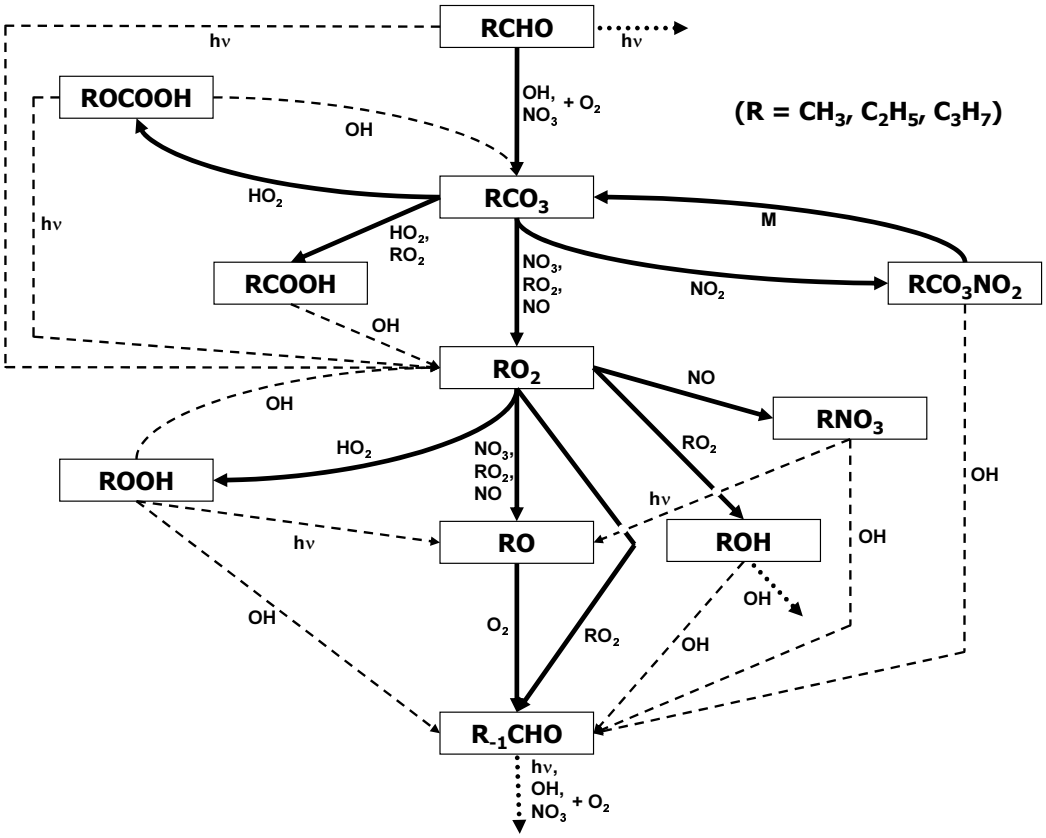

Figure 2.5: *Simplified scheme of C_2-C_4 aldehyde degradation initiated by hydroxyl/nitrate radicals and light according to the MCMv3 [Saunders et al 03]. Dashed arrows: degradation paths suppressed in a dark and low-OH environment in presence of NO_x and O_3. Dotted arrows: reactions not involved in the cascade mechanism. R: alkyl structure.*

quickly recombine with molecular oxygen to yield acyl peroxy radicals.

$$\mathrm{RCHO} + \mathrm{NO_3} \longrightarrow \mathrm{HNO_3} + \mathrm{RCO} \tag{2.25}$$

$$\mathrm{RCO} + \mathrm{O_2} \xrightarrow{\mathrm{M}} \mathrm{RCO_3} \tag{2.26}$$

Degradation of higher aldehydes provides a significant source of aldehydes containing less carbon atoms than the precursor. Thus, formaldehyde is generated in the course of acetaldehyde degradation, acetaldehyde in propionaldehyde degradation etc. In the presence of hydroxyl (and nitrate) radicals a longer aldehyde is expected to be cascaded down to the shortest aldehyde, which has the longest lifetime. Reaction pathways, currently proposed by atmospheric chemistry models, are shown in Figure 2.5. Acyl peroxy radicals react with $\mathrm{NO_2}$ to peroxyacyl nitrates ($\mathrm{RCO_3NO_2}$). As these can decompose back to acyl peroxy radicals, an equilibrium is established, which strongly depends on temperature.

$$\mathrm{RCO_3} + \mathrm{NO_2} \overset{\mathrm{M}}{\rightleftharpoons} \mathrm{RCO_3NO_2} \tag{2.27}$$

For example, the lifetime of peroxypropionyl nitrate ($R = C_2H_5$) is 28 h at 273 K and 68 min at 293 K [Mineshos and Glavas 91]. At low temperatures NO_2 is bound in peroxyacyl nitrates. At high temperatures, when peroxyacyl nitrates decompose, the NO_2 is released again. Apart from their role as reservoir the peroxyacyl nitrates also react with OH radicals to yield the next shorter aldehyde ($R_{-1}CHO$).

$$RCO_3NO_2 + OH \longrightarrow R_{-1}CHO + \text{other products} \tag{2.28}$$

However, the magnitude of the rate coefficient renders this reaction pathway unimportant in most cases [Seinfeld and Pandis 97]. At high temperatures, when conversion from acyl peroxy radicals to peroxyacyl nitrates is not favoured, or in the presence of NO, the radicals can react to alkyl peroxy radicals

$$RCO_3 + NO_3 \longrightarrow NO_2 + CO_2 + RO_2 \tag{2.29a}$$
$$RCO_3 + NO + O_2 \longrightarrow NO_2 + CO_2 + RO_2 \tag{2.29b}$$
$$RCO_3 + RO_2 \longrightarrow RO + CO_2 + RO_2 \tag{2.29c}$$

from where several paths lead to formation of the shorter aldehyde.
Under dark laboratory conditions, when the influence of photochemical and OH radical reactions is negligible, the centre vertical path presented in Figure 2.5 would be the only significant way for cascading down aldehydes. Carboxylic and per-carboxylic acids ($RCOOH$, $ROCOOH$), peroxyacyl nitrates, alkyl hydroperoxides ($ROOH$), alkyl nitrates (RNO_3) and alkyl hydroxides (ROH) on the side branches would act as reservoir species under these conditions.

2.2.2 The Reaction of Ethene and Ozone

Ethene (C_2H_4) is the simplest symmetrical alkene in the atmosphere. Due to its simple structure reaction mechanisms and products resulting from ethene degradation can be followed quite easily making it a well suited compound for process studies.
In the following the mechanism of the reaction of ethene and ozone is described [Atkinson 97, Neeb et al 98]. Some of the theoretically possible reaction paths, which are not important under atmospheric conditions, are neglected here. The initial reaction of ethene and ozone, whereby the latter adds to the double bond, forms the energy-rich primary ozonide (POZ), which rapidly decomposes into a primary carbonyl compound, $HCHO$ in this case, and an energy rich carbonyl oxide, which is called the Criegee intermediate, CH_2OO^*.

$$C_2H_4 + O_3 \longrightarrow POZ^* \longrightarrow CH_2OO^* + HCHO \tag{2.30}$$

The product yield of $HCHO$ is unity. The energy rich Criegee intermediates can decompose uni-molecularly or are stabilised by collision with air molecules.

$$CH_2OO^* \xrightarrow{M} CO_2 + H_2 \tag{2.31a}$$

$$\xrightarrow{M} CO + H_2O \tag{2.31b}$$

$$\xrightarrow{O_2} OH + HO_2 + CO \tag{2.31c}$$

$$CH_2OO^* \xrightarrow{M} CH_2OO \tag{2.32}$$

The branching ratio of the stabilisation of the Criegee intermediate reported in the literature ranges from 0.20 to 0.47 (a compilation of references is given in *Rodríguez-Bares* [03]). The relative OH formation yield lies in the range between 0.12 and 0.18, whereby an additional oxygen molecule is required.
The stabilised Criegee intermediate (CH_2OO) is expected to react with water vapour either to form hydroxymethyl hydroperoxide ($HOCH_2OOH$), which is removed from the gas-phase by decomposition on surfaces to formic acid plus water vapour, or to produce $HCHO$ and hydrogen peroxide.

$$CH_2OO + H_2O \xrightarrow{M} HOCH_2OOH \tag{2.33a}$$

$$\longrightarrow HCHO + H_2O_2 \tag{2.33b}$$

Experimental evidence suggests that the latter path is of minor importance. Aside from this, as potential reaction partners for stabilised Criegee intermediates NO, NO_2, CO, SO_2, O_3, lower aliphatic aldehydes, C_2H_4 and $HCOOH$ are proposed, though little is known about these reactions to date and they are assumed to be insignificant under atmospheric conditions [IUPAC 05].

The Ethene-Ozone Reaction in the MCMv3

Model studies are useful to validate current atmospheric chemistry models by experimentally monitoring reactants and products. To the present day, reactions of alkenes and O_3 have been investigated with respect to radical yield or yield of radical precursors. In that respect, the simplest aldehyde, $HCHO$, plays an important role, as it is formed in considerable amounts in almost all alkene-ozone reactions and affects the atmospheric HO_x budget. The MCM provides kinetics for atmospheric photochemistry simulations. In case of ethene the MCMv3 module consists of 96 reactions (Appendix A.1), which together with inorganic reactions adds up to 115. Following all these processes would be time consuming. In the laboratory a chemical

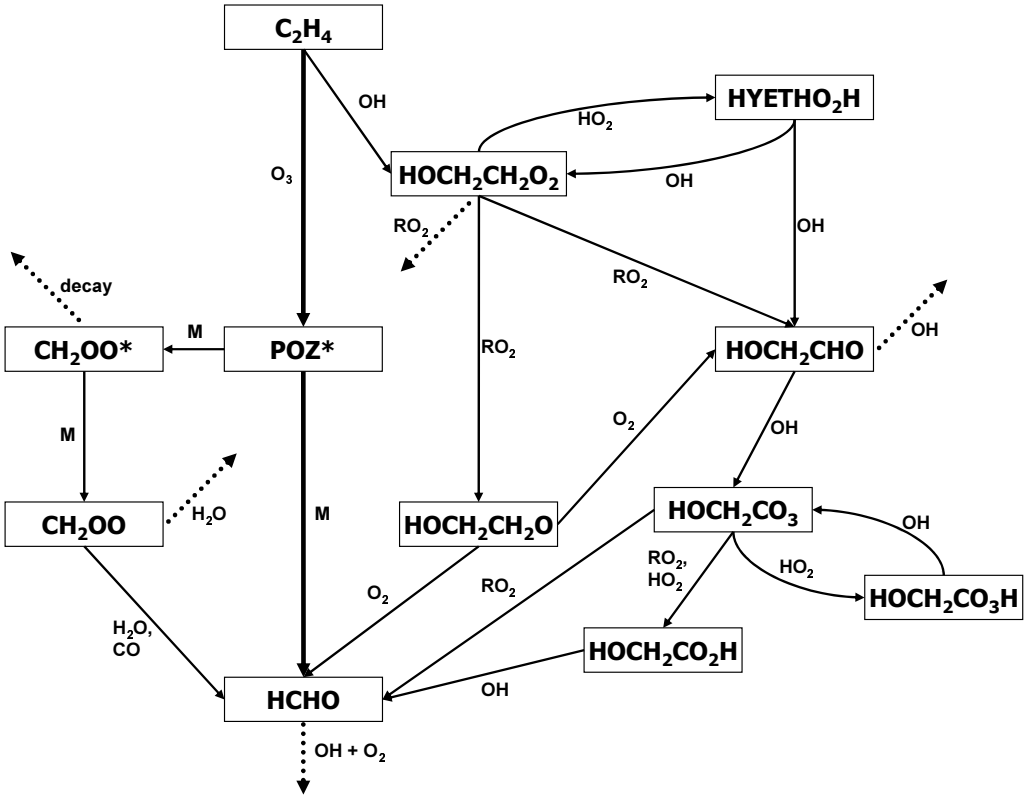

Figure 2.6: *Simplified scheme of HCHO production initiated by the ethene-ozone reaction according to the MCMv3 [Saunders et al 03]. Dotted arrows: degradation paths not resulting in HCHO formation. Interactions with light, nitrogen and sulfur compounds not shown. POZ: primary ozonide.*

system can be designed, in which only ethene and O_3 are present. Thus, the time evolution of reactants and products can be investigated with practicable effort. In a dark, NO_x free and sulfur free environment, the number of possible reactions is reduced to 41. Hydroxyl radicals are produced in secondary reactions in the ozonolysis [‡] of ethene. Therefore, the effect of OH radicals on the simple system, which would extend the number of relevant reactions significantly, have to be anticipated. If the effect of OH was reduced by a radical scavenger like CO the response of the system would be of particular interest. Focusing on the $HCHO$ yield, Figure 2.6 shows a schematic how ethene is converted into $HCHO$ either directly or indirectly. In the settings mentioned before, two chemical sinks exist for ethene, reaction with O_3 and reaction with OH radicals. $HCHO$ is formed as primary carbonyl directly from the ethene-ozone reaction, but is produced also via secondary pathways comprising radical initiated and two Criegee intermediate channels. Here, the only loss process of $HCHO$ would be the OH reaction. To test the response of the chemical system, a model run with initial mixing ratios of 150 ppbv ethene and 120 ppbv O_3 is presented. Generic

[‡]Reaction in which ozone oxidises an alkene forming carbonyl compounds

atmospheric data of temperature (T=278 K) and pressure (p=1013 hPa) were used. Calculations proceeded for a low absolute humidity of about 100 ppmv. All species included in the model were also subjected to a slow dilution (-3 % h^{-1}), which is a feature of the environmental chamber (cf section 3.1.1), in which the experiments for this thesis were carried out. The upper left panel of Figure 2.7 presents the model ouput of the reactants ethene and O_3 as well as the products $HCHO$ and CO, the latter being produced in the uni-molecular decay of the energy-rich Criegee intermediate. As the reaction of ethene and ozone proceeds quite slowly, the major part of the concentrations is diluted. The upper right panel of the same figure shows the radicals OH, HO_2 and RO_2. Net production of OH occurs only in the uni-molecular decay of the CH_2OO^*. HO_2 is mainly formed in the reaction of OH and O_3. The lower left panel of the figure shows conversion rates of all reactions that involve $HCHO$. From six possible production ways, the three most significant are

- the reaction of ethene and ozone (black),
- the reaction of stabilised Criegee intermediates and water vapour (blue), which rate coefficient is uncertain by at least a factor of 4 [IUPAC 05]
- and the collision initiated disintegration of a radical formed in the course of the OH initiated degradation of ethene (green).

The lower right panel of the figure shows all loss processes concerning ethene. Due to the tardiness of the ethene-ozone reaction, dilution is the main contribution (black). Nonetheless, the loss due to OH (blue) is about an order of magnitude lower than that due to O_3 (red). Subtracting the effect of dilution, for every ethene molecule degraded approximately one formaldehyde molecule is formed over the whole model time period of nine hours.
Model predictions of the $HCHO$ yield change considerably, when high level CO is added to the system in order to prevent the OH interference with the ethene chemistry. The model run was repeated applying an extra addition of 500 ppmv CO. Results are presented in Figure 2.8 the same way as in Figure 2.7. CO is a reservoir gas in the concentration range of 10^{16} cm^{-3}. The upper right panel of the figure shows that OH radicals are suppressed compared to the model without excess CO. Conversion rates of the lower left panel indicate that all radical initiated $HCHO$ production and destruction pathways are negligible. The ethene-ozone reaction (black) is still the most important direct $HCHO$ source. However, the reaction of stabilised Criegee intermediates and CO (red) gains higher importance and contributes considerably to the overall $HCHO$ yield. Using these settings the $HCHO$ yield approaches 1.37, as the branching ratio of the stabilisation

of the energy rich Criegee intermediates is 0.37. The only competitive reaction, that of CH_2OO and water vapour, turns out to be irrelevant in the 100 ppmv range applied in these calculations, which is a comparatively low humidity level for the atmosphere. The lower right panel of Figure 2.8 confirms the effective quenching of OH.
Model runs at high level CO imply that the $HCHO$ yield with respect to ethene conversion is boosted significantly due to the greater relevance of Criegee intermediate reactions. However, all processes involving Criegee intermediates are subject to high uncertainties. The reaction with CO had been proposed in a single relative-rate study [Su et al 80]. The uncertainty level of that reaction must be assumed high. So far, no evidence for the $CH_2OO - CO$ reaction was reported [Gutbrod et al 97] and extensive studies of these processes are still missing. As Criegee intermediates are difficult to detect, and the environment, in which they could be generated, is laborious to realise, validation of the proposed reactions remains a task for future studies.

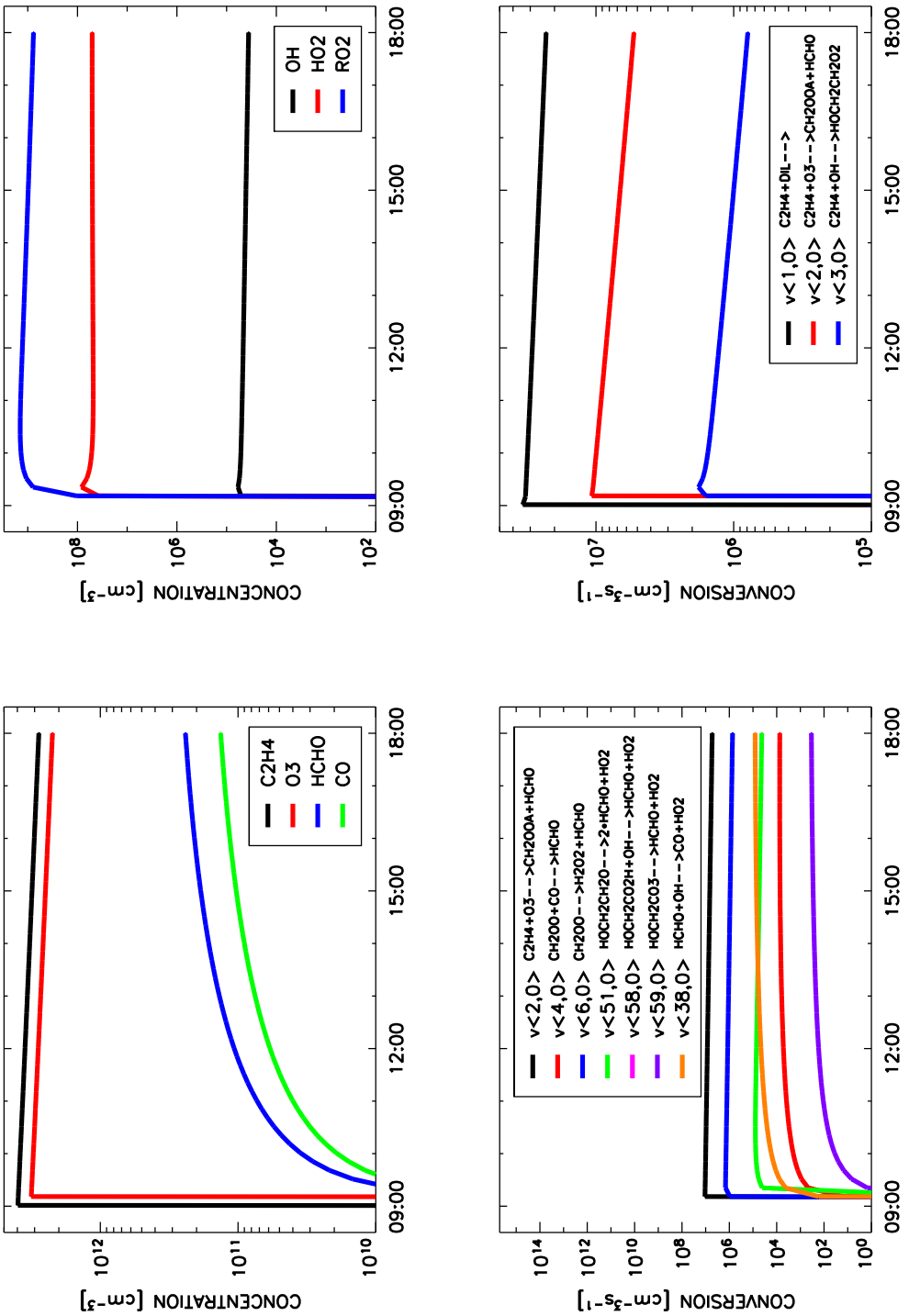

Figure 2.7: *Upper left panel: concentration-time profiles of the reactants ethene and ozone as well as the products HCHO and CO as calculated in the model. Upper right panel: product RO_2 and HO_x radicals. Lower left panel: conversion rates of all reactions involving HCHO. Lower right panel: conversion rates of all loss processes of ethene.*

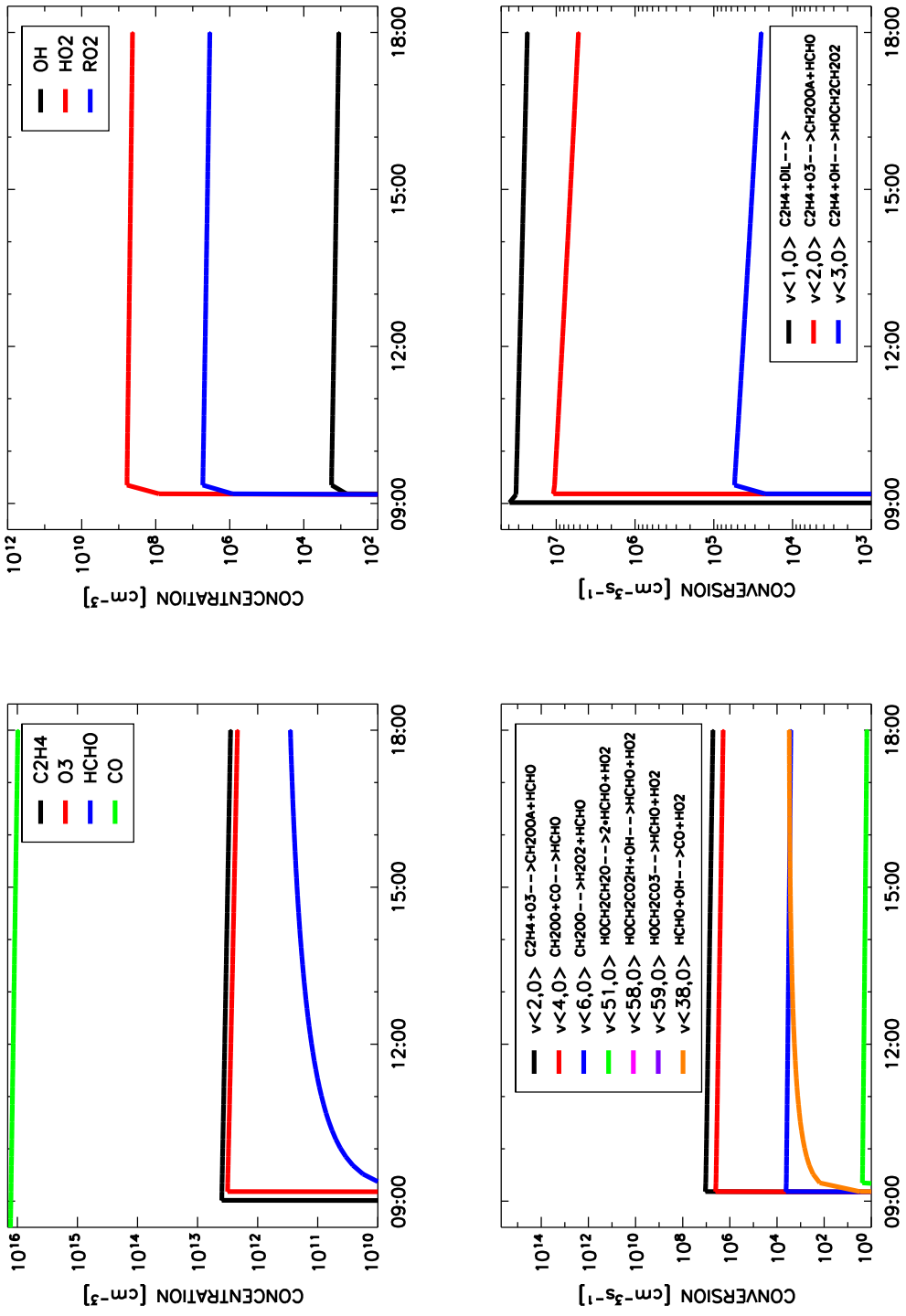

Figure 2.8: *Upper left panel: time profiles of ethene, ozone, HCHO and CO as calculated in the model. Upper right panel: RO_2 and HO_x radicals. Lower left panel: conversion rates of all reactions involving HCHO. Lower right panel: conversion rates of all loss processes of ethene.*

2.2.3 Nitrate Radicals

Next to O_3 and OH radicals NO_3 is the third relevant atmospheric oxidising agent. Nitrate radicals are formed in the presence of NO_x and O_3. NO_x is emitted in the troposphere either from anthropogenic or natural sources, whereas O_3 is formed only photochemically in polluted air. Reactions presented below show the fate of NO_x leading to NO_3 radical formation [Wayne et al 91].

$$NO + O_3 \longrightarrow NO_2 + O_2 \tag{2.34}$$

$$NO_2 + O_3 \longrightarrow NO_3 + O_2 \tag{2.35}$$

Although the rate coefficient of reaction (2.35) is rather small (3.5×10^{-17} cm^3s^{-1} at 298 K [IUPAC 05]), it is the only relevant production pathway in the troposphere, since the precursors O_3 and NO_2 are normally present in sufficiently large quantities. Generally, mixing ratios of NO_3 radicals range from few pptv in remote regions to several hundred pptv in heavily polluted air. In some cases NO_3 radicals abound such, that they compete with OH for being the main oxidant of atmospheric hydrocarbons [Finlayson-Pitts and Pitts 00].
The fate of NO_3 radicals is determined by photolysis, gas-phase reactions with a multitude of compounds and reactions at the interface of gas and condensed phase. Photolysis at wavelengths below 630 nm splits NO_3 back into NO_x and O_x [Geyer 00].

$$NO_3 + h\nu \xrightarrow{10\%} NO + O_2 \tag{2.36a}$$

$$\xrightarrow{90\%} NO_2 + O \tag{2.36b}$$

A typical photolysis frequency under clear sky conditions and a solar zenith angle smaller than 70° would be 0.2 s^{-1} leading to an almost instant destruction of NO_3 radicals during daylight hours.
Furthermore, in presence of gas-phase NO, NO_3 radicals are rapidly degraded according to

$$NO_3 + NO \longrightarrow NO_2 + NO_2 \tag{2.37}$$

with a k of 2.6×10^{-11} cm^3s^{-1} at 298 K [IUPAC 05]. Photolysis and reaction with NO convert NO_3 radicals back into NO_x. Since O_3 normally exceeds NO_x these two pathways lead to a null cycle continuously regenerating NO_3. Other possible organic gas-phase reactants include aromatics, alkenes, terpenes, alkanes and aldehydes (for the latter see section 2.2.1). A simplified scheme of NO_3 radical interaction with other compounds is summarised in Figure 2.9. Aldehyde reactions proceed via hydrogen atom abstraction to form nitric acid and acyl radicals [D'Anna and Nielsen 97]. Nitric acid formation and ensuing degradation constitutes a significant sink of atmo-

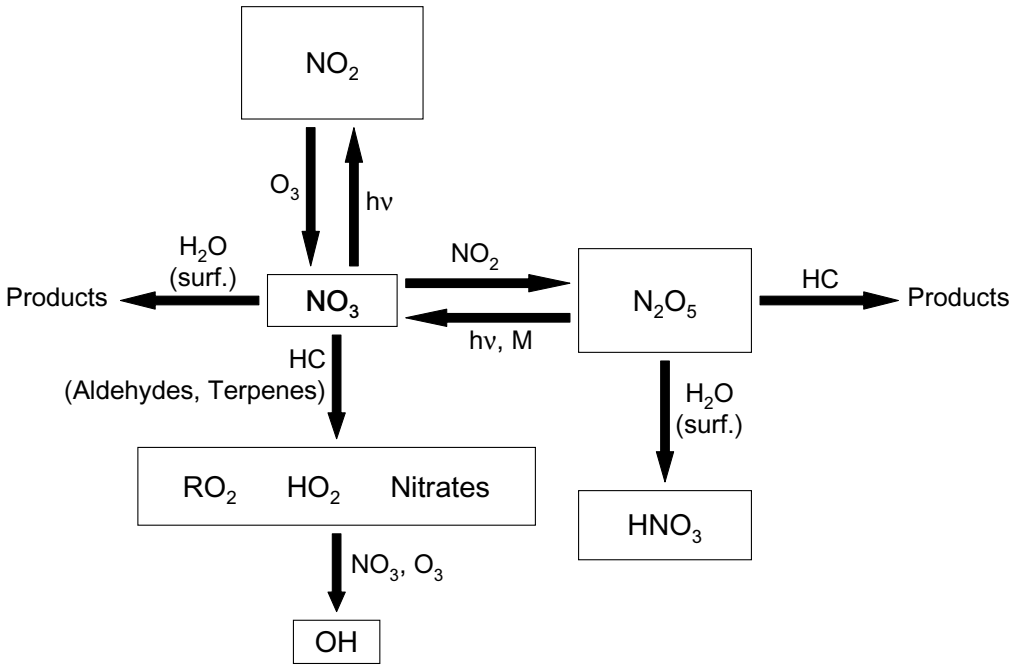

Figure 2.9: *Simple scheme of NO_3 radical reactions with other gas-phase compounds in the troposphere adapted from* Wayne et al *[91]. HC: hydrocarbon; surf.: surface reaction*

spheric NO_3. NO_3 was also reported to react with organic peroxy radicals [Platt et al 90].

$$NO_3 + RO_2 \longrightarrow RO + NO_2 + O_2 \tag{2.38}$$

The degradation of NO_3 radicals due to reaction with itself or NO_2 is too slow under typical atmospheric conditions to be of importance. Another relevant degradation process is a heterogeneous loss either of NO_3 radicals itself or of dinitrogen pentoxide, which is the thermodynamically balanced product of NO_2 and NO_3 radicals

$$NO_3 + NO_2 \overset{M}{\rightleftharpoons} N_2O_5 \tag{2.39}$$

with a $k_{\rightharpoonup}$(2.39) of 1.2×10^{-12} cm^{3}s^{-1} and a uni-molecular $k_{\leftharpoondown}$(2.39) of 6.6×10^{-2} s^{-1} at 298 K and atmospheric pressure, respectively. Due to the strong temperature dependence of the back reaction (2.39) the N_2O_5 can serve as reservoir species for its precursors NO_2 and NO_3. Formed in a cool environment N_2O_5 molecules decompose and release their precursors NO_2 and NO_3 in warmer regions. Moreover, due to the equilibrium any N_2O_5 loss process affects the NO_3 budget as well. N_2O_5 is taken up by aerosols, thereby being hydrolysed to nitric acid,

$$N_2O_5(g) + H_2O(surface) \rightleftharpoons 2HNO_3(surface) \tag{2.40}$$

or is removed by dry deposition.

Chapter 3

The Atmosphere Simulation Chamber SAPHIR

The atmosphere simulation chamber SAPHIR * (Figure 3.1) is designed for the investigation of tropospheric photochemistry. It allows the set-up and investigation of chemical systems under controlled conditions, ie without disturbing transport processes or unaccounted sources or sinks of trace gases, which often occur in the field. The state of the art instrumentation at the chamber, operated by the staff of the Institute for Chemistry and Dynamics of the Geosphere II: Troposphere, allows monitoring of chamber characteristics as well as concentrations of chemical species.

3.1 Technical Description

The chamber consists of a double-walled FEP † foil of 125 μm for the sides and the top and 250 μm thickness for the ground, which was chosen for its chemical inertness and favourable light transmission characteristics. The gap between the two foils is flushed continuously with high purity nitrogen in order to prevent any intrusion of contaminants from outside. It has a roughly cylindrical shape with a diameter of 5 m, a length of about 18 m and an effective volume of 270 m^3. Synthetic air is generated by evaporation of high purity liquid N_2 and O_2 (purities $>$ 99.9999 %). Two flow controller systems serve to replenish air. The purge gas flow has a capacity of up to 500 m^3s^{-1} and serves to clean the chamber. Before starting an experiment the chamber is purged until all trace gas concentrations are below the limit of detection. The experiment gas flow has a capacity of up to 15 m^3s^{-1} (normally operated at 6 to 8 m^3s^{-1}) and serves to replenish chamber air that was lost due to sampling extraction and leaks at the

*Simulation of Atmospheric PHotochemistry In a large Reaction chamber

†per-Fluoro-Ethylene-Propylene, DuPont

Figure 3.1: *South-east view of the atmosphere simulation chamber SAPHIR with shutters open.*

chamber wall. The chamber is operated at 40 Pa above ambient pressure to ensure that air flows exclusively from inside to outside. Humidity can be introduced into the chamber by evaporating high purity water (Milli-Q Gradient A10, Millipore Corporation) and adding it to a flow ($\approx$ 300 $m^3 s^{-1}$) of synthetic air. Humidification can take more than 60 minutes depending on the requested humidity, whereby the lowest reachable level is about 0.1 mbar. Furthermore, the chamber is equipped with a shutter system that protects the teflon foil from bad weather conditions and keeps the volume in darkness if required. It can also be opened for daylight exposure within 60 seconds. When illuminated the actinic flux in the wavelength range from 290 to 420 nm in the chamber is typically 20 to 30 % lower than outside due to shadowing of the metal framing and light transmission characteristics of the FEP foil [Bohn and Zilken 05]. A second shutter system comprises a filter foil, which cuts off all light below 370 nm. A list of technical parameters is shown in Table 3.1. The following characteristics of the chamber were described in detail by *Rodríguez-Bares* [03] and are summarised here.

Table 3.1: *Technical specifications of the SAPHIR chamber.*

Effective volume [m^3]	270
Surface/Volume [m^{-1}]	≈ 1
Diameter [m]	≈ 5
Length [m]	≈ 18
Wall material	FEP teflon
Wall thickness [μm]	150 – 250
Synthetic air (%)	N_2:O_2 (80:20)
Purity of synthetic air	$>$ 99.9999 %
Shutter system	Open/Close within 60 s
Experiment gas flow [m^3h^{-1}]	3 – 15
Max. purge gas flow [m^3h^{-1}]	500
Mixing time [min]	10 (illuminated)
	30 (darkened)
	≈ 1 (fan)
Pressure	Ambient + 40 Pa
Temperature	Ambient conditions

3.1.1 Dilution

During operation of the chamber gas losses occur due to leaks in the FEP foil and sampling extraction. The replenishment experiment gas flow keeps the chamber at constant pressure, thereby slowly diluting all trace gases present. The dilution is described by an exponential decay.

$$-\frac{dC(t)}{dt} = \frac{F_{\mathrm{E}}}{V} \times C(t) = k_{\mathrm{Dil}} \times C(t) \tag{3.1}$$

$$C(t) = C(0) \times \exp\left(-\frac{1}{V}\int_0^t F_{\mathrm{E}} \times dt'\right) \tag{3.2}$$

Here, $C(t)$ is the concentration of a compound at time t, F_{E} is the experiment gas flow in m^3s^{-1} and V the effective volume of the chamber in m^3. The quotient of the last two is called dilution coefficient. Typically, concentrations are reduced by 2 to 3 % h^{-1}. The effective chamber volume was determined by monitoring the dilution of a couple of inert gases and simultaneously recording the applied flow.

3.1.2 Mixing and Transport

The instrumentation at the chamber is designed for monitoring a homogeneous air volume. This requires that the gas in the chamber is well mixed.

As gases are injected through inlets at the chamber wall, it takes some time for the injection to distribute. This time is a characteristic of the chamber and was determined in the illuminated and dark chamber with compounds, which are chemically inert (eg CO_2). First, a specific amount was injected and then the time span, until a constant concentration level had been reached, was measured. Mixing was achieved within 10 and 30 minutes in the illuminated and dark chamber, respectively. Mixing is caused by three processes.

- Molecular diffusion; this process is negligible (diffusion coefficient in air $D_{\mathrm{molec}} \approx 2{\times}10^{-5}$ m^{2}s^{-1} at 12° C).
- Convection driven by temperature gradients; this process is important, particularly when the chamber is illuminated (empirical diffusion coefficient $D_{\mathrm{illum}} \approx 0.6$ m^{2}s^{-1}).
- Turbulent diffusion presumedly driven by the experiment gas flow; as the experiment gas flow is operated continuously, this process is the other important mixing force (empirical diffusion coefficient $D_{\mathrm{turb}} \approx 0.15$ m^{2}s^{-1}).

In late summer 2004, a fan was installed into the chamber in order to enforce rapid mixing. In operation, mixing times were reduced to the order of one minute.

3.1.3 Sources in the Chamber

Nitrous Acid

Photolytic formation of nitrous acid ($HONO$) was proposed as an important OH source in simulation chambers leading to elevated reactivity in simulation chamber experiments. Indeed, $HONO$ production has been observed at SAPHIR under solar irradiation [Rohrer et al 05]. NO_2 as a precursor of $HONO$ and photolysis of nitrate on different surfaces are excluded for the specific SAPHIR set-up. A photolytic $HONO$ source at the chamber wall is suggested, which depends on humidity, light intensity and temperature. An empirical function reproduces the observed $HONO$ formation rates within 10 %.

$$S(\mathrm{HONO}) = a_{1,2} \times J(\mathrm{NO_2}) \times \left(1 + \left(\frac{RH}{RH_0}\right)^2\right) \times \exp\left(-\frac{T_0}{T}\right) \qquad (3.3)$$

Here, $S(\mathrm{HONO})$ is the source term in cm^{-3}s^{-1}, $J(\mathrm{NO_2})$ the photolysis frequency of NO_2 in s^{-1}, RH the relative humidity in %, T the temperature in

Kelvin. $a_{1,2}$, RH_0 (11.6 %) and T_0 (3950 K) are fitting parameters. The values best fitting SAPHIR data are given in parentheses. The parameter $a_{1,2}$ was found to change with time (4.7×10^{13} cm^{-3} from Jul 2001 to Jul 2002 and 8.5×10^{13} cm^{-3} from Aug 2002 to Dec 2003). Being an empirical function the exact mechanism behind the HONO source remains unknown.

Formaldehyde

Karl [04] describes a photolytic formaldehyde source in the dry chamber at relative humidities less than 1 %. A photolytic fragmentation of organic compounds deposed on the chamber wall in previous experiments is suggested as source. An empirical relation was found that depends on light intensity and temperature.

$$S(\mathrm{HCHO}) = B \times J(\mathrm{NO_2}) \times \exp\left(-\frac{\vartheta_0}{T}\right) \tag{3.4}$$

Here B (3.29×10^{17} cm^{-3}) and ϑ_0 (6142 K) are further fitting parameters. As is the case with the HONO source, the exact mechanism behind the HCHO source is not understood to date.

3.2 Instrumentation at SAPHIR

At the chamber several instruments are operated covering a range of physical parameters as well as gas-phase compounds. A list of the instrumentation is shown in Table 3.2. Short descriptions of instruments, which data were used in Chapter 5, are given below. Performance figures of these instruments are given in Table 3.3 at the end of this section.

The Hantzsch Monitor (Hantzsch), HCHO

The Hantzsch monitor at SAPHIR works in three steps [Krinke 99]. First, the gas-phase $HCHO$ in an air sample is transferred into the aqueous phase by a stripping process. Then, adding the Hantzsch reagent containing acetylacetone, acetic acid and ammonium acetate initiates a reaction with $HCHO$ to produce the fluorescent dye 3,5-diacetyl-1,4-dihydrolutidine. This dye is excited with radiation at 410 nm and the resulting fluorescent light is detected at 510 nm in the yellow spectral range. The instrument has to be calibrated on a liquid formaldehyde standard frequently, which in practice is done prior to and after the measurements. In operation, a null reference is determined periodically by introducing a hopcalite [‡] scrubber into the sample flow, which removes all traces of $HCHO$.

The Gas Chromatograph (GC), hydrocarbons up to C_{10}

Many non methane hydrocarbons (NMHC), eg lower alkenes like ethene, are detected by a commercially available gas chromatograph (Chrompack, the Netherlands) [Rodríguez-Bares 03]. The system is equipped with a flame ionisation detector (FID) and a cryo focus modul (Auto-TCT, Chrompack, the Netherlands). Sampling for NMHC analysis proceeds through a heated (T ≈328 K) inlet line of about 10 m length at the chamber. Before pre-concentration of NMHCs from chamber air, water vapour is removed by a cold trap at 233 K. After water removal the NMHCs are sampled at 253 K in an adsorption tube also partly trapping CO_2. In order to remove it, the tube is heated to 293 K and purged with ultra-pure Helium. The NMHCs are then thermally desorbed at 523 K and transferred to a capillary column where they are cryo-focussed at 113 K. To transfer the NMHCs to the gas chromatograph the capillary column is heated to 413 K. Eventually, peak separation is performed on a fused silica column (Al_2O_3, KCl deactivated). The system is calibrated on a commercially available certified standard mixture of 30 VOC compounds in synthetic air (NPL, UK). VOC mixing ratios in this standard range from 2 to 7 ppbv. The variation of the individual mass response factors is less than 8 %.

[‡]A mixture of copper and manganese oxides

Table 3.2: *Standard SAPHIR instruments for the measurement of gas-phase species and meteorological parameters.*

METHOD	PARAMETER, SPECIES
Chemiluminescence	NO_2, NO
Dew/frostpoint hygrometer	Relative humidity
Gas chromatography [a]	Several VOCs [b] (up to C_{10})
	CO
Hantzsch [c]	HCHO
Laser induced fluorescence	OH, HO_2
Laser-DOAS [d]	OH
(LDOAS)	HCHO
LOPAP [e]	HONO
MIESR [f]	RO_2
	NO_3
Pressure transmitter	Pressure
Spectroradiometer	Actinic flux
Ultrasonic anemometer	Temperature
UV absorption	O_3
Xenon short arc lamp DOAS [d]	O_3
(XDOAS)	NO_2, NO_3, HONO
	HCHO, Benzaldehyde
	Toluene, Phenol ...
	SO_2
	Halogen oxides

[a] Flame Ionisation Detector, Mass Spectrometry
[b] Volatile Organic Compound
[c] Fluorescence technique
[d] Differential Optical Absorption Spectroscopy
[e] LOng Path Absorption Photometer
[f] Matrix Isolation Electron Spin Resonance

The Long Path Absorption Photometer (LOPAP), HONO

Nitrous acid is measured by a commercially available, recently presented, long path absorption photometer (LOPAP) [Heland et al 01]. The instrument consists of three units. First, gas-phase $HONO$ is stripped from an air sample into the liquid phase using sulfanilamide and HCl, whereby a diazonium salt is formed. Then, a solution containing n-(1-naphthyl)ethylenediamine-dihydrochloride is added to the stripping solution, which initiates formation of an azo dye. The resultant solution is finally transferred into a liquid core waveguide, in which it is analysed by absorption spectroscopy. Calibration of the set-up is done with a liquid nitrite standard regularly. The LOPAP works with two instrumentally identical serial channels. The first is the actual detection channel. When the air sample reaches the second, almost all of the $HONO$ is removed. Thus, the second serves to account for interferences.

The Chemiluminescence Detector (CL), NO_x

The sum of NO and NO_2 is detected photometrically, as energy rich nitrogen dioxide emits photons in a relaxation process. The chemiluminescence instrument at SAPHIR [Rohrer and Brüning 92] is based on the chemical reaction of the ambient NO on a background of excess O_3. The resultant radiation from the energy rich NO_2^* product, which is proportional to the concentration of the NO in the air sample, is detected. As NO chemiluminescence detection is well characterised, NO_2 is detected the same way, the only difference being its prior conversion to NO. This is achieved photolytically using a broadband arc lamp. The conversion efficiency is approximately 50 %. Calibrations are performed regularly on a gas mixture standard. Furthermore, consistency checks are conducted using the photostationary concentrations of NO_x and O_3 in the illuminated chamber.

The Ultraviolet Absorption Detector (UV-A), O_3

At SAPHIR O_3 measurements are performed with a commercial instrument (Ansyco, Germany). The method is based on the ultraviolet absorption of O_3 at 254 nm. A mercury emission lamp serves as light source. The UV light is detected by evacuated photo-tubes. The photometer comprises two detectors. One determines the transmission coefficient through the sample cell. The other detects the lamp's UV intensity as reference. In operation, the gas sample can flow into a cuvette directly or over a selective ozone scrubber. The two ways alternate every ten seconds. Thereby, transmissions from the ozone scrubbed and ozone containing samples are measured, respectively. O_3 concentrations are finally calculated taking the

Table 3.3: *Performance figures of the instruments at SAPHIR, which data were used in this thesis.*

INSTRUMENT	PARAMETER	ACQUIS. TIME [min]	LOD [a] [pptv]	ACCURACY [%]
Hantzsch [b]	HCHO	2	25	3
GC [c,d]	hydrocarbons	30	10	8
LOPAP [e]	HONO	1	5	10
CL [f]	NO_2	1.5	10	10
UV-A [f]	O_3	1	2000	5
DPH [f]	H_2O	1	5×10^7	4
LDOAS [g,h]	HCHO	3	≈ 400	> 3

[a] Limit of detection
[b] Personal communication from Ralf Tillmann
[c] LoD and accuracy may slightly vary for different species
[d] Personal communication from Robert Wegener
[e] Personal communication from Rolf Häseler
[f] Personal communication from Franz Rohrer
[g] LoD and accuracy estimated from comparison to Hantzsch
[h] Personal communication from Eric Schlosser

ratio of the two transmissions according to the Beer-Lambert law (cf section 2.1.1).

The Dewpoint Hygrometer (DPH), H_2O

The dewpoint marks the temperature at which an air sample is saturated with water vapour at given pressure. When saturation occurs below 0° C the term frostpoint is used. For detection an air sample is passed over a small mirror, which is cooled thermo-electrically. Changes in the reflectance properties of the mirror surface, caused by starting condensation, are detected by an optical system. A control circuit keeps the mirror exactly at the transition temperature where condensation on the mirror surface starts. This dewpoint/frostpoint temperature is directly related to the absolute water vapour content of the air sample.

The Laser-DOAS Instrument (LDOAS), OH

The LDOAS [§] instrument is designed to directly detect OH radicals [Hausmann et al 97, Schlosser et al 06]. However, it also measures $HCHO$, naphthalene and SO_2 [Neuroth et al 91]. A modified multiple reflection cell is used to obtain total light paths in the chamber of 2240 m allowing the detection of OH concentrations down to 10^6 cm^{-3}. Regarding the set-up this system is quite similar to the XDOAS [¶] instrument that was established in the course of this thesis. A laser as light source facilitates sufficient light transmittance within the narrow spectral range around 308.1 nm where OH can be measured. The light exiting the multiple reflection cell is guided to a high resolution spectrograph (SOPRA F1500, $\Delta\lambda$ = 2.7 pm). There, the spectrum is detected by a photo diode array.

[§]To distinguish the DOAS instruments at SAPHIR, the abbreviation LDOAS is used for the Laser-DOAS

[¶]XDOAS: Xenon short arc lamp DOAS, Chapter 4

Chapter 4

The XDOAS Instrument

A DOAS instrument was constructed during this thesis. Some parts of the design were adapted from the already established Laser-DOAS (cf section 3.2). However, planned as an instrument not optimised for a single trace gas, specific differences remain. One of the main challenges of the XDOAS construction was, that its components had to be adapted to the set-up of the SAPHIR chamber.

4.1 The White Cell

Multiple reflection cells allow the realisation of long folded absorption paths on a small spatial scale. As part of the XDOAS instrument a multiple reflection system of the White cell design was constructed and installed into the SAPHIR chamber during this thesis. The principle of the White cell was first proposed in 1942 by *White* [42]. Since then it was modified by *White* [76] and *Ritz et al* [92]. The White cell consists of an arrangement of three spherical mirrors and three prisms. Long folded light paths are achieved by guiding light through a particular pattern on mirrors and prisms being reflected hence and forth in a given incremental number of the cell's base length.
The White cell mirrors and prisms are located at the front ends of the chamber at a distance of 20 m (Figure 4.1). To allow accurate optical alignment they were attached to adjustable mounts. Planning the SAPHIR chamber great care was taken that reactions on chamber walls would not affect the chamber volume. Additional features like optical mounts located inside the chamber would provide non-inert surfaces, at which chemical reactions could be altered in an unpredictable and irreproducible way. Hence, the objective of the multiple reflection cell at SAPHIR was to install as much optical mounts outside the chamber. This was accomplished by the set-up shown in Figure 4.2. The FEP foil is guided and fixed between the back of

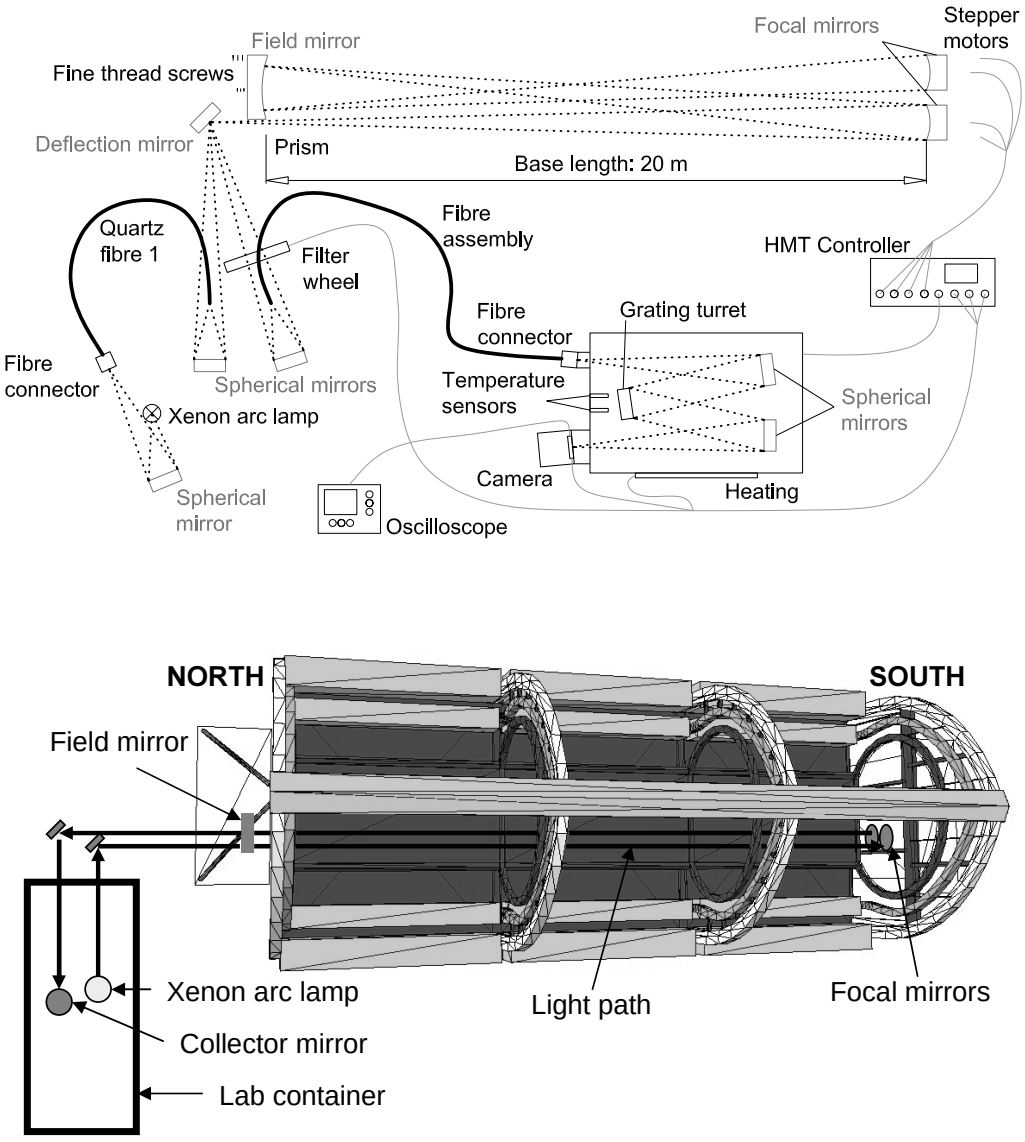

Figure 4.1: *Upper panel: simplified scheme of the optical multiple reflection cell showing how the light is guided into the White cell via transfer optics consisting of mirrors and optical fibres and then collected and guided to the spectrograph. Lower panel: bird's eye view how the cell was integrated into the chamber set-up. Chamber wall not shown.*

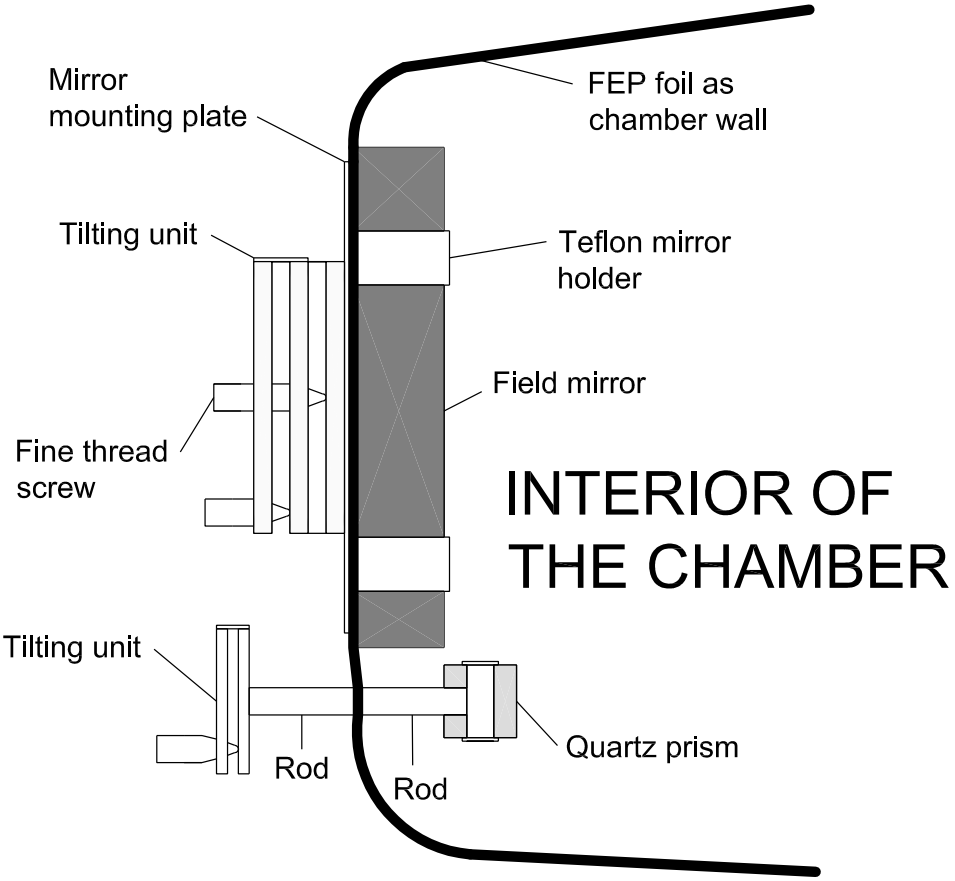

Figure 4.2: *Simplified arrangement how the optical mounts of field mirror and prisms were integrated into the chamber at the northern side. Not shown is a transparent quartz plate on its mount, which separates inside and outside for light entering or leaving the cell.*

field mirror and mirror mounting plate and between two metal rods, which serve as holders of the prism mount. Using a non-degassing sealing compound, directly where the foil was penetrated, air tightening was ensured reliably. The same design was used for the two focal mirrors.
At the north end the field mirror (diameter: 300 mm; thickness: 50 mm; f/33; cutting edge length: 160 mm; coating: UV enhanced Al) is situated above the prisms. The field mirror can be tilted manually in the vertical and the horizontal direction by two fine thread screws. The outer left and right prism can be tilted vertically and the centre prism horizontally according to the required degree of freedom.
The function of the prisms is to displace the light beam by two total reflections at the centre of the cathetus sides. Thus, for each light spot on the field mirror a neighbour spot is created. The distance to the original spot is defined by the spatial shift. This way, the light path is doubled with each prism pass. As the cathetus angle is slightly smaller than 90° the incoming and outgoing light beams converge at the distance of the focal mirrors.

Between field mirror and the smallest prism light enters and exits the cell (Figure 4.3) through a Quartz plate, which separates the chamber from ambient air.
The two focal mirrors (diameter: 150 mm; thickness: 40 mm; f/67; coating: UV enhanced Aluminum) at the south end are arranged in line vertically. They can be tilted by a set of two stepper motors (types ZSS 25.200.0.6 and ZSS 32.200.0.6, Phytron, Gröbenzell) in the vertical as well as the horizontal direction. The numerical aperture of this set-up results in 1 / 133.

4.2 The Transfer Optics

The light source and the receiving optics are located on top of a lab container at the north end of SAPHIR. Transfer optics guide the light from there to the chamber. Light emitted by the light source is collected by a spherical concave mirror with a diameter of 76.2 mm (f/2), which has an ultraviolet enhanced Aluminum coating. From there, it is cast off-axially onto the entrance of an optical fibre with a core diameter of 400 μm, a numerical aperture (NA) of 0.12 and a length of two metres.
The fibre exit is located in front of another spherical mirror of the same type as above that collects the light and throws the image along its optical axis via three deflection mirrors into the entrance of the multiple reflection system. The numerical aperture is chosen such as to match that of the White cell.
Having passed the White cell the light is deflected towards the lab container. A filter wheel (type OWIS 65, Staufen) is placed between chamber and receiving optics, which has five slots for square-sized filters ($2'' \times 2''$) and can activate a VIS blocker (U-330, Schott) for measurements in the ultraviolet, a UV blocker (OG530, Schott) for measurements in the visible, or a blind for determining the background signal. On the lab container, having passed the filter wheel, the light is collected by a spherical mirror of the type described above. The image of the spherical mirror is cast onto the entrance of an optical fibre being part of a larger fibre assembly. The assembly guides the light from the outdoor set-up into the lab container where the data acquisition electronics are situated.
The fibre assembly (cf *Veitel* [02]) consists of a single fibre with a diameter of 600 μm, an NA of 0.12 and a length of four metres, with which light exiting the multiple pass cell is collected. The fibre exit is connected to a bundle of 19 circularly packed fibres with an individual diameter of 100 μm, an NA of 0.12 and a length of 0.5 m each. They are arranged in line vertically at the other end to form the linear entrance slit into the spectrograph with dimensions of 100 μm $\times$ 2 mm. There, the light is dispersed and cast onto the light detector.

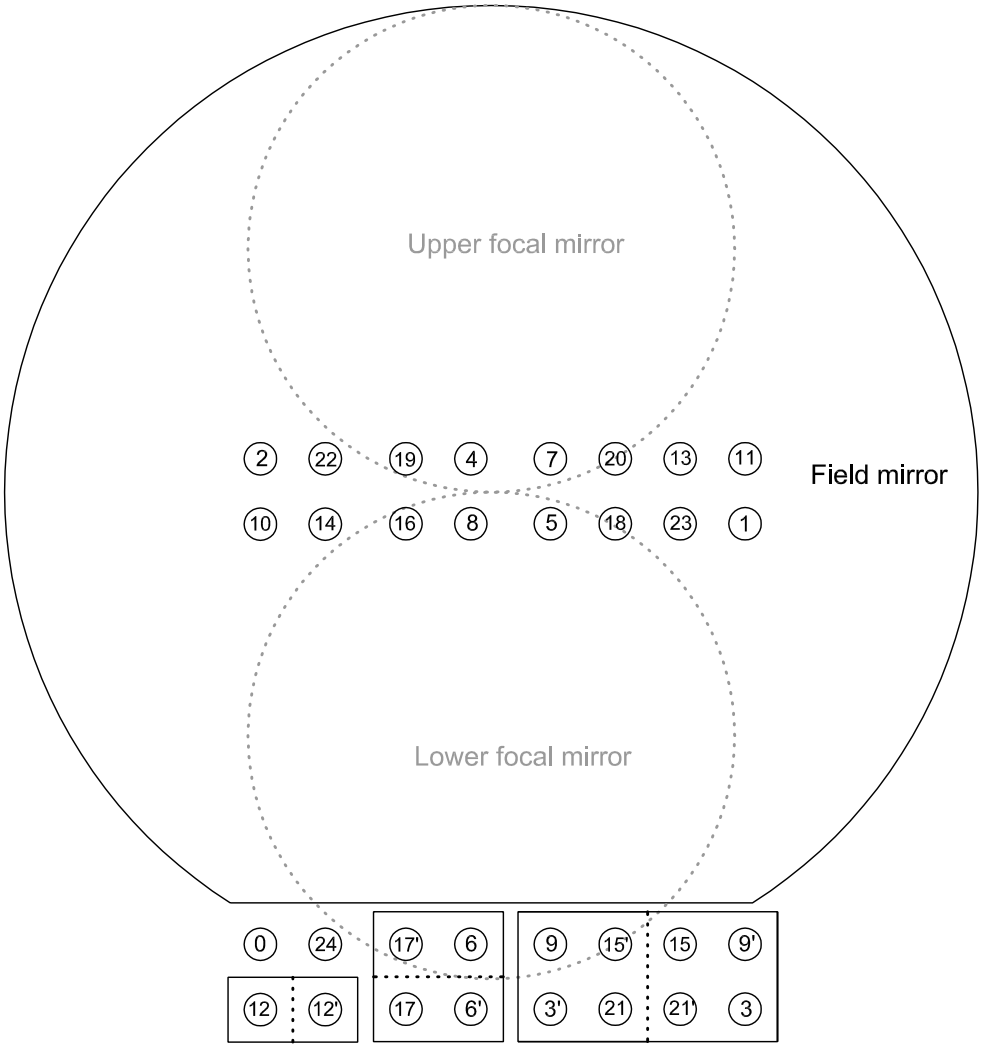

Figure 4.3: *Light spot chart of the White cell with a front view of the field mirror (on top) and the three prisms (in line below). The set-up shown yields a total path length of 960 m being the longest path that can be realised providing reasonable light transmittance. Grey dotted lines mark the focal mirrors being situated at the other end of the chamber. Numbers denote the order of passing with 0 being the entrance and 24 being the exit spot.*

4.3 Light Source, Spectrograph, Light Detector and Controller

The Light Source

Light source is a Xenon short arc lamp operated in a lamp housing (Müller Elektronik Optik, Moosinning). Xenon short arc lamps are favourable for spectroscopic applications, as they have a high light yield in ultraviolet and visible wavelength intervals, emit a very smooth spectrum and have a light arc that is rather small and can be regarded as a point source in most cases. The types used in this thesis are XBO 75 W/2 and XBO 75 W/2 OFR (OSRAM, Munich), which have a color temperature of about 6000 K generating a sun-like spectrum, and an average lifetime of 400 h. The stated dimension of the light arc is 0.3×0.5 mm^2.

The Spectrograph

The spectrograph of the XDOAS set-up (type HR 460, JobinYvon) is based on the design by *Czerny and Turner* [30]. It has a focal length of 460 mm, an NA of 0.09 and is operated in first order. The grating turret is equipped with two holographic gratings. One has 1200 grooves per mm and a blaze wavelength of 330 nm, which is particularly suited for studies in the ultraviolet. The other has 600 grooves per mm and a blaze wavelength of 500 nm, which is preferred for studies in the visible and near-infrared (Table 4.1). The grating turret can be turned incrementally by a sine drive motor, which is limited by two end switches, covering a range of 209304 steps. Each position corresponds to a given wavelength interval on the light detector array. This relationship was determined using Hg emission line spectra (section 4.5.4). As the performance of the spectrograph is temperature sensitive, it is thermostated in an insulation box at a constant temperature ($\pm 0.25°$ C) of 10 to 20° C above ambient with a maximum heating power of 100 W.

The Light Detector

The light detector and the ensuing data acquisition electronics are parts of a commercially available detection assembly (Hoffmann Messtechnik, Rauenberg). The detector consists of an array of 1024 photo diodes (type S3904, Hamamatsu) allowing the spectral retrieval of light in the wavelength range between 200 and 1100 nm. The PDA is placed in a camera that was evacuated and then refilled at an excess pressure of Argon of 0.2 mbar in order to avoid deposition of dust particles and condensation

Table 4.1: *Characteristics of two holographic blazed gratings installed in the spectrograph Jobin Yvon HR 460.*

GRATING	1	2
Grooves [mm^{-1}]	1200	600
λ_{Blaze} [nm]	330	500
Spectral interval [nm]	44	89
Dispersion [nm $\times$ $pixel^{-1}$]	0.043	0.087
Line width, FWHM [nm]	0.17	0.34

of water vapour. The camera is attached to the spectrograph. The operational voltage of the diodes is 2.5 V. The diodes have a capacity of 4 pF. Thermal electron transitions lead to a slow self-discharge. As this dark current depends on temperature exponentially, the PDA was cooled to a temperature of -15° C using a Peltier cooler controlled by a Pt100 temperature sensor at the cold side.

The Controller

Acquired light signals are sent to an HMT controller (Hoffmann Messtechnik, Rauenberg) via an integrator, in which the signals are converted from an analog into a digital format. From there, they are forwarded to a standard desktop computer and saved. In order to simplify the optical adjustment of the cell the acquired spectra can be monitored by an oscilloscope, which was added to the set-up. Moreover, the controller operates the stepper motors at the south end of SAPHIR and thus the tilting of the focal mirrors and the positioning of the filter wheel. Furthermore, it monitors and controls heating and cooling of spectrograph and PDA, respectively.

4.4 Discussion of the Experimental Set-up

Optical fibres are flexible waveguides, which do not require frequent optical adjustment. Furthermore, a fibre coupled to a spectrograph provides a well defined entrance slit. Therefore, optical fibres were used in the entrance as well as the exit transfer optics.
In the first designs of the entrance transfer optics the light was cast directly from the first spherical mirror into the White cell entrance. As the surroundings of the actual light arc also emit light, though of less spectral quality, the fibre was introduced to generate a more definite spot-like image. This could be delivered by the exit of the optical fibre, and hence

simplified the optical alignment of the White cell.
The first design of the exit transfer optics comprised a single fibre with core diameter of 200 μm, an NA of 0.11 and a length of four metres. The fibre guided the light into the spectrograph. However, as the fibre entrance slit was 200 μm in height, whereas the diodes of the light detector have a height of 2.5 mm, the larger fraction of the diode surface was not illuminated. This added undesired noise to the spectral retrieval. To amend this and to improve the resolution of the set-up, the single fibre was swapped for a fibre assembly (described in section 4.2). Using the fibre assembly, the resolution was halved lowering the spectroscopic limit of detection of most chemical species. Aside from this obvious upgrade, an improvement of the signal-to-noise ratio due to the better use of the detector surface was expected. In fact, using this design the optimum signal-to-noise ratio was doubled. As trade-off, a loss in light transmittance resulted, which is most likely caused by a mismatch of the numerical apertures of the fibres and the spectrograph [*]. Apart from this, a so far uncharacterised light loss in the connector between single fibre and fibre bundle must be considered.
In conclusion, optical fibres contribute to the stability of the optical system. However, better performance could be achieved, if optical fibres even more customised to the other instrumental components were employed.
The light transmittance from Xenon short arc lamp through the White cell to PDA depends strongly on the reflectance of the coating of the White cell mirrors. The higher the mirror reflectance (and the corresponding light transmittance in the cell) is, the more passes through the White cell can be realised, which in turn would improve the sensitivity of the instrument. Certain coatings would allow to increase reflectances close to unity. However, these high reflectances could just be maintained over a small spectral range, which would reduce the list of detectable compounds. Therefore, the White cell mirrors were equipped with an enhanced Aluminum coating, which has a reflectance of about 0.94 over two wavelength ranges from 250 to 350 and 600 to 700 nm. The coating allows light path lengths of 320 m ($\lambda < 300$ nm) and 960 m (300 nm $< \lambda <$ 400 nm and 600 nm $< \lambda <$ 700 nm) providing sufficient light transmittance.
The White cell prisms serve to extend the number of passes through the volume. In the set-up at SAPHIR monolithic prisms with one surface for the cathetus and hypothenuse sides are used. The single surface design allowed the optimisation of the cathetus angle (slightly smaller than 90°) for one displacement only. This design causes a geometric light loss at the greatest prism, as it is passed four times at two different spatial displacements. Recently, *Grassi and Guzzi* [01] proposed a new monolithic multiple surface design for a prism, which would allow the operation of a White cell without geometric light loss. To the present day, application of such a prism has not been reported in the literature, so that its performance still

[*] 0.09 for the Jobin Yvon compared to 0.12 for the fibres in the set-up

remains to be investigated.

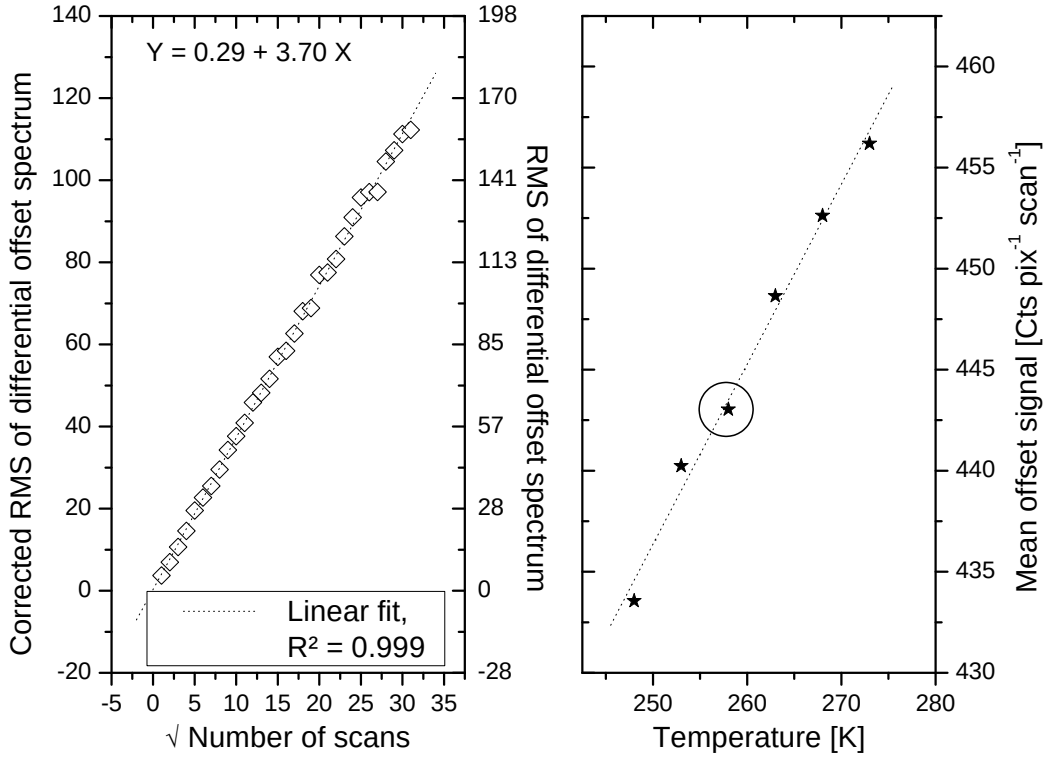

Figure 4.4: *Left panel: dependence of the offset noise on the square-root of the number of scans at −15° C. Right panel: temperature dependence of the electronic offset of the Hamamatsu S3904. The straight line is meant to guide the eye. The circle denotes the data point at the standard measurement temperature (258 K = −15° C).*

4.5 Instrumental Characterisation

All characteristics presented in this section were monitored repeatedly between the experiments.

4.5.1 Electronic Offset and Dark Current

The offset signal is a bias voltage added to the photo diode read out signal in order to avoid any problems converting analog into digital signals. To determine the electronic offset the PDA was covered and a spectrum was recorded at the minimum integration time of 60 ms and 1000 scans. The overall offset level stayed constant over a long period of operation time. A slight temperature dependence was observed. As an artificial signal the electronic offset is a source of noise and contributes significantly to the total noise of a spectrum when scans are co-added. The offset noise was determined plotting the quotient of two offset spectra corrected by $\sqrt{2}$ against the square-root of the number of scans. Figure 4.4 shows the dependence of

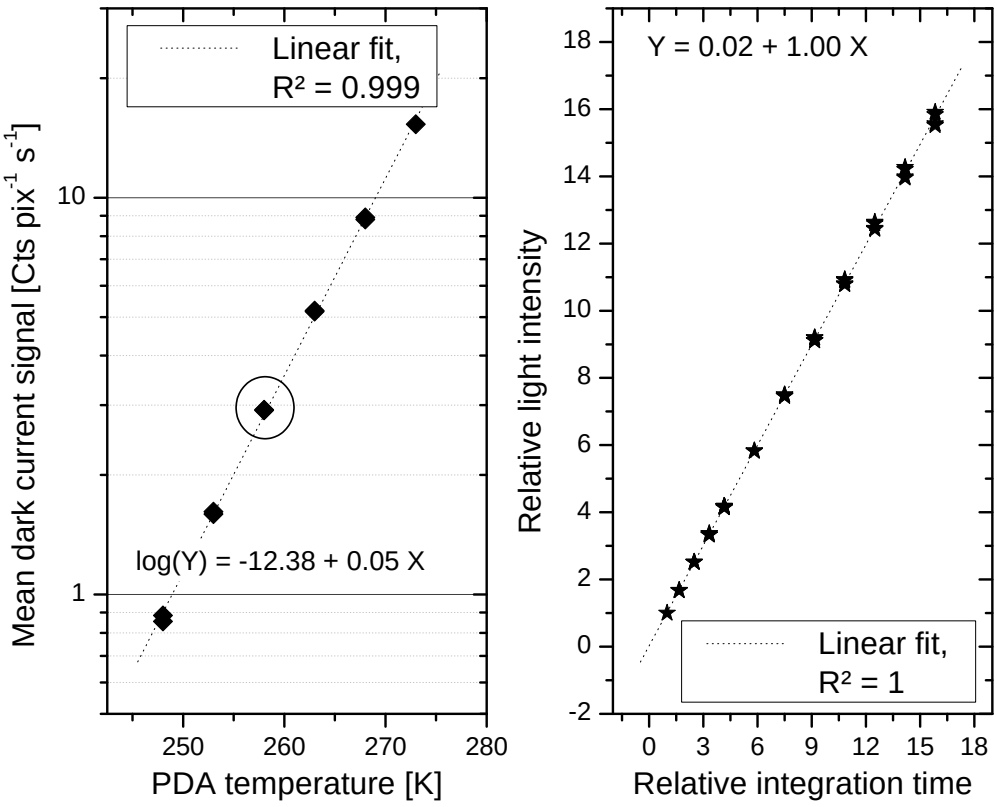

Figure 4.5: *Left panel: temperature dependence of the average dark current signal of the Hamamatsu S3904. The circle denotes the standard measurement temperature (258 K = −15° C). Right panel: PDA response signal vs total integration time, both in relative units.*

the electronic offset on temperature and the fitting of the offset noise. The noise of a spectrum grows by 3.7 counts$\times\sqrt{\text{Number of scans}}$.
The dark current signal occurs due to a thermal self-discharging of the detector pixels and is strongly temperature dependent. It was determined recording a single scan spectrum of ten minutes integration time with the dark PDA. It was observed that few pixels show a disproportionately stronger dark current signal than others. The temperature dependence is shown in the left panel of Figure 4.5.

4.5.2 Detector Linearity

Light detector measurements have to be performed in an intensity range where the detected signal depends linearly on the incoming light intensity. To verify linearity spectra had to be recorded with the same specifications regarding scan number and integration time leaving light intensity as the only variable. A simpler approach to test linearity is taking spectra at varying integration time and then calculating the relationship between integrated signal and total integration time assuming that light conditions

stayed constant during the measurements. For that purpose, measurements were done with mercury emission lines in wavelength ranges from 300 to 700 nm using also second order line peaks. These were normalised to the intensity obtained at the shortest integration time, and likewise the integration times were normalised to the smallest value (right panel of Figure 4.5). The slope of the regression results in unity within five permil.

4.5.3 Stray Light

Stray light is a potential part of a recorded intensity spectrum whose origin cannot be discriminated against the actual, desired, light signal. Therefore, it can distort the analysis considerably. Generally, there are three kinds of stray light in spectroscopic studies using multiple reflection cells.

- Stray light being generated in the spectrograph, eg by surface deficiencies of gratings or mirrors, a mismatch between the numerical apertures of transfer optics and spectrograph, or the presence of bright and reflective surfaces inside the spectrograph housing.
- Atmospheric stray light.
- Stray light being generated in the multiple reflection cell by overillumination of the mirrors on highly reflective adjacent metal surfaces.

Smooth stray light in a measurement spectrum reduces the optical density by the relative part it has compared to the actual measured signal. For example, if a spectrum contains the signature of 10 ppbv NO_2 without stray light, the spectral content is reduced to 9.9 ppbv if 1 % of smooth stray light is introduced. If the stray light spectrum bears a spectral signature itself or a signature that could be falsely perceived as an absorption structure, it would produce erroneous measurements, as origin and type of the structure were hard to identify. Atmospheric stray light contains spectral features due to the solar Fraunhofer structures. However, these are known quite accurately [Kurucz et al 84].
The set-up used in this thesis was tested for spectrograph stray light by taking white light spectra in the wavelength region below 400 nm with an edge filter (type Schott GG400). Spectrograph stray light should depend basically on the total light intensity guided into the spectrograph. As the emission strength of the Xenon short arc lamp is highest in the region between 400 and 500 nm, results obtained with the GG400 are transferable to other wavelength intervals as an upper limit. The result of a test on 23 Nov 2004 is shown in Figure 4.6. In the block region the scaled stray light resulted in less than 1 % (0.8 % from 338 to 382 nm and 0.2 % from

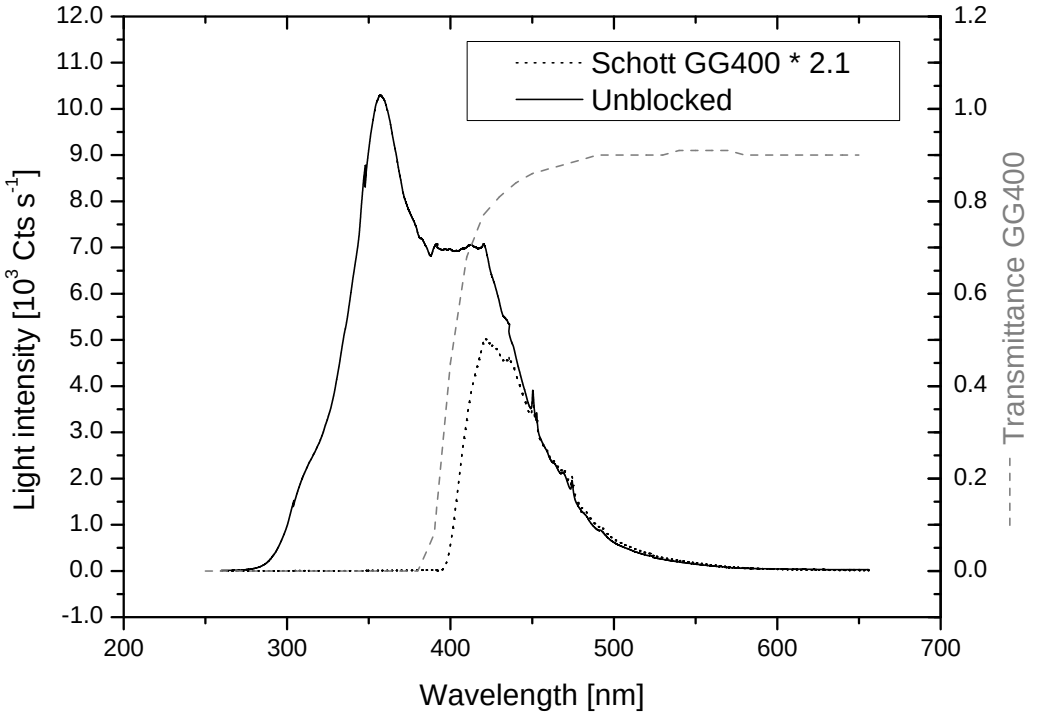

Figure 4.6: *Left axis: light intensity of the Xenon arc lamp at a path length setting in the White cell of 960 m unfiltered (solid) and using a filter (Schott, type GG400) blocking wavelengths below 400 nm (dotted). The maximum light intensity at 360 nm is caused by the reflection characteristics of the employed mirrors. The spectrum taken with activated filter was scaled to match that without filter. Right axis: transmittance of the GG400 filter as specified by the producer.*

306 to 350 nm) compared to the signal without filter.
Atmospheric stray light was determined by taking spectra without the artificial light source. With chamber shutters closed the relative stray light signal turned out to be less than a permil. With shutters open relative stray light depended strongly on the chosen wavelength region being generally highest in the visible and falling off towards the ultraviolet and the infrared. In the ranges of interest from 400 to 450 nm (NO_2, Glyoxal) and 600 to 700 nm (H_2O, NO_3), with shutters open and clear sky conditions in summer, the stray light part did not exceed 3 %.
Stray light generated in the chamber is the most difficult to determine. In this thesis the approach was to block one of the light spots on the field mirror at the 960 m setting immediately before the light was exiting the White cell. For that purpose, a blind was introduced in place of spot number 23 (Figure 4.3), where just a double pass equalling 40 m was missing before the light would have left the cell. If surface reflections, eg on the mirror mounts, were responsible for stray light it would grow with the number of passes, so that this set-up should yield a good estimation. Indeed stray

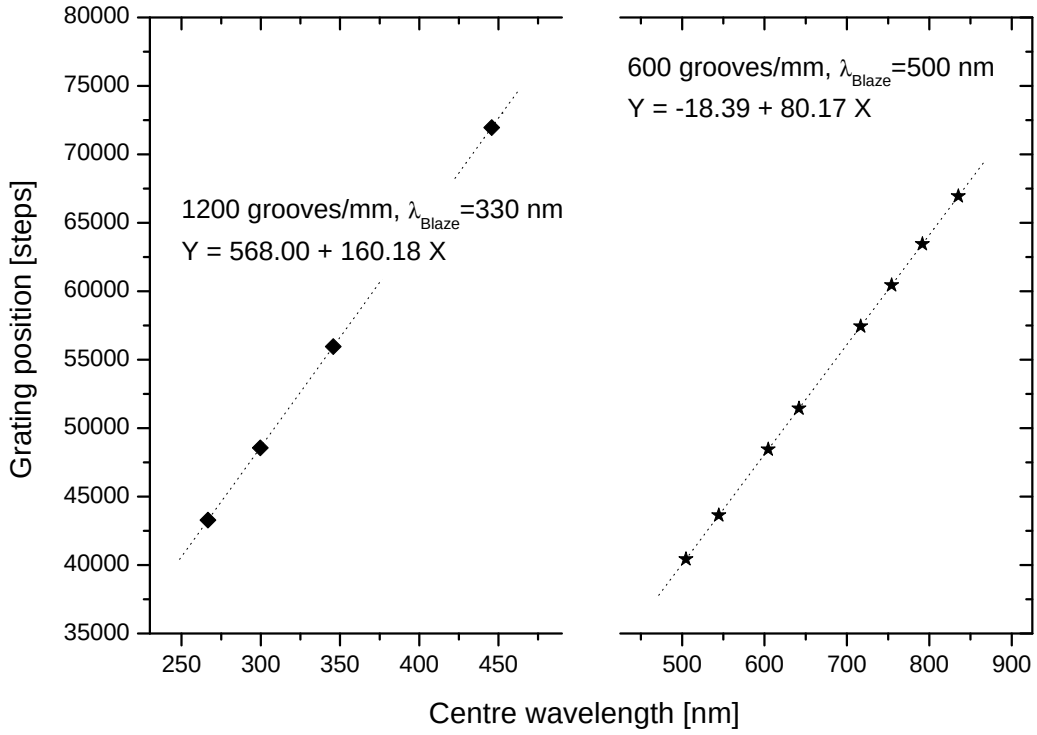

Figure 4.7: *Relation of stepper motor position and centre wavelength for grating 1 (1200 grooves per mm, λ_{Blaze} = 330 nm, left panel) and grating 2 (600 grooves per mm, λ_{Blaze} = 500 nm, right panel).*

light was detected, though it stayed in the sub percent regime compared to the actual light signal (relative part 0.3 % from 306 to 350 nm on average). In conclusion, three sources of stray light have been investigated. Generally, spectrograph and chamber stray light levels are so low, that they can be neglected. On the other hand, atmospheric stray light does not matter, when chamber shutters are closed, but can be important with shutters open. For quality assurance, control sample spectra of atmospheric stray light were recorded during each experiment. A summary how stray light is considered in the error estimation of the spectroscopic evaluation is given in section 4.5.5.

4.5.4 Wavelength Calibration

A proper spectral evaluation requires an accurate wavelength calibration. The original, mostly natural, line width of the spectral features should be much smaller than the instrumental line width, which defines the resolution of the set-up. The instrumental line width is governed by the horizontal dimension of the entrance aperture into the spectrograph. In case of a single cylindrical fibre it depends on its core diameter and is strictly symmetrical in shape. For spectroscopic systems a wavelength calibration is

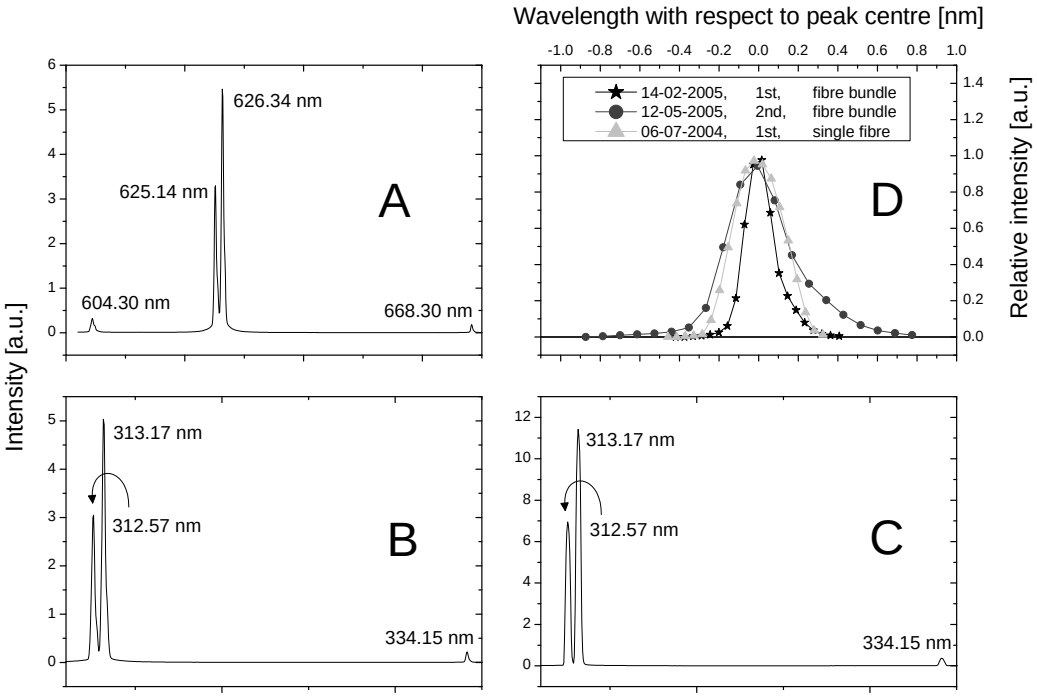

Figure 4.8: *Panel A: grating 2, the entrance slit is a linear fibre bundle (2^{nd} order peaks). Panel B: grating 1, the entrance slit is a linear fibre bundle, (1^{st}). Panel C: grating 1, the entrance slit is a single fibre, (1^{st}). Panel D: line shapes of the peaks at 334.15 nm (1^{st}) and 668.30 nm (2^{nd}), respectively. Peaks taken with the linearly arranged fibre bundle are not entirely symmetric.*

achievable either by taking cuvette spectra of trace gases that have prominent spectral features in the region of interest, eg NO_2 from 400 to 450 nm or O_3 from 250 to 300 nm, or by recording emission line spectra, eg of mercury. In this thesis the second method was used. Pixel positions of the peaks were assigned to the respective wavelengths taken from the literature. Then, the relation between the two was calculated. Relations for this particular set-up turned out to be linear (Figure 4.7). Sample emission line spectra and line shapes are presented in Figure 4.8.

4.5.5 Error Contributions from the Instrumental Set-up

The precision of the DOAS measurement and the accuracy of the absorption cross sections have been discussed in section 2.1.4. Aside from these, other uncertainties arise due to the set-up of the apparatus. In that respect, the background signals like electronic offset and dark current have to be considered. Monitoring them over period of several days revealed that their variability was 10^{-4}, which renders this error source negligible.

Table 4.2: *Accuracies (95 % confidence limit) of a DOAS evaluation of a typical spectrum recorded by the XDOAS multiple reflection cell set-up at SAPHIR.*

SOURCE OF UNCERTAINTY	ACCURACY IN %
Electronic background	negligible
Stray light	1
Ambient abundance	1 – 3
Total	**1.4 – 3.2**
+ Accuracy of cross section	2 – 8

The possible stray light sources were discussed in detail in section 4.5.3. Here, the stray light generated in the multiple reflection cell and in the spectrograph is taken into account with a contribution of 1 % to the overall uncertainty. Atmospheric stray light is corrected for the individual measurements. Finally, an additional error can be introduced by ambient air. In the chamber the light path is folded many times defining the region of spectral retrieval. Nonetheless, in the set-up at SAPHIR the light first has to traverse the distance to and from the chamber in ambient air before it is guided to the spectrograph. This external distance amounts in total to about ten metres. Considering the light path in the chamber of ca 1000 m (or 320 m depending on the White cell setting) this yields a relative uncertainty of 1 % (3 %) on the optical density assuming that the concentration of the monitored trace gas in ambient air compares to the artificial gas mixture in the chamber. If so, additional absorption in ambient air could be described with an effective path length, which would equal the path limited by the White cell design if the ambient air was clean and would show the same time profile as the external concentration. As all these contributions are independent of each other, they are summed up quadratically (Table 4.2).

Chapter 5

Results and Discussion

The XDOAS instrument was planned, constructed, installed and technically characterised at the atmosphere simulation chamber SAPHIR within eighteen months. The experiments performed with the newly established XDOAS can be classified in three groups.

- XDOAS measurements were compared to other detection methods for the molecules NO_2 (chemiluminescence, CL), O_3 (ultra-violet absorption, UV-A), H_2O (dewpoint hygrometer, DPH), $HONO$ (long path absorption photometer, LOPAP), benzene, m-xylene (both gas chromatograph, GC), and $HCHO$ (Hantzsch monitor, Hantzsch).
- The XDOAS was furthermore compared to concentration-time profiles, calculated based on chamber properties, of a series of injected trace gases. This was done for $HCHO$, benzaldehyde, toluene, and NO_3 radicals.
- XDOAS measurements and data from other instruments were used to validate current kinetic data in atmospheric chemistry models. This was done for the $HCHO$ yield from ethene oxidation, the OH reaction with benzene and m-xylene, as well as for the aldehyde degradation by NO_3.

5.1 Instrument Intercomparisons

In this section instrument intercomparisons are presented treating the compounds NO_2, O_3, H_2O and $HONO$. Beyond that, instrument intercomparisons were also performed for $HCHO$, benzaldehyde, toluene, benzene and m-xylene. However, since these data were also compared to model studies and calculations, they are presented in separate sections.
The procedure for comparing data was the same for all compounds. The

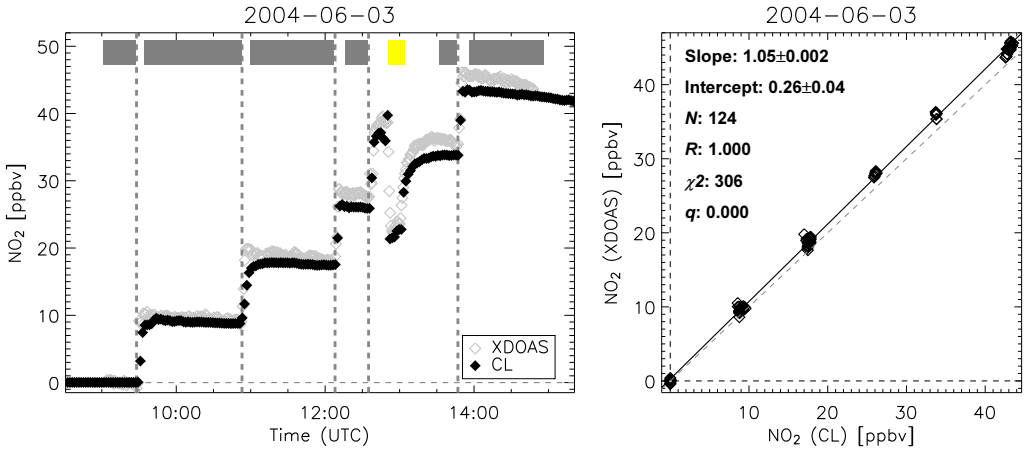

Figure 5.1: *Left panel: NO_2 profiles recorded by XDOAS and CL. Grey horizontal line: zero line. Grey dashed vertical lines: NO_2 injections. Grey bars: data included in the correlation. Yellow bar: period of daylight exposure. Right panel: correlation plot. Dashed grey line: unity projection.*

data of the reference instrument were sampled on the XDOAS time grid, when the precision of the reference was much better than that of the XDOAS (NO_2, H_2O, $HONO$). When the precisions of the two detection methods had about the same magnitude (O_3) or the time resolution of the reference was much lower (benzene, m-xylene) the XDOAS data were sampled on the grid of the reference. Errors of the sampled time profiles were calculated taking into account the scatter of data lying in an acquisition interval as well as the errors of the individual data points. Regression and correlation parameters were computed assuming a linear relation accounting for errors in both axes, when available (y-axis: XDOAS, x-axis: reference instrument). Injection periods of a trace gas as well as periods of purging were excluded from the analysis as indicated by the grey bars in the concentration-time profiles. Correlation and regression parameters (Pearson linear correlation coefficient R, χ^2, quality of fit parameter q [Press et al 92]) are given in the correlation plots.

5.1.1 Nitrogen Dioxide

An NO_2 intercomparison (XDOAS vs CL) was carried out on 3 Jun 2004 in the purged chamber. Pure gas-phase NO_2, taken from a compressed gas cylinder, was injected in five steps of similar magnitude (left panel of Figure 5.1). After the fourth injection the chamber was exposed to daylight for about ten minutes in order to test the NO_x budget derived from the CL data (confer section 3.2). The budget was found to agree well with calculations based on a photostationary state assumption. When shutters were closed again, the NO_2 recovered the previous concentration level.
The first injection began at 09:28 UTC. The DOAS fit was performed with

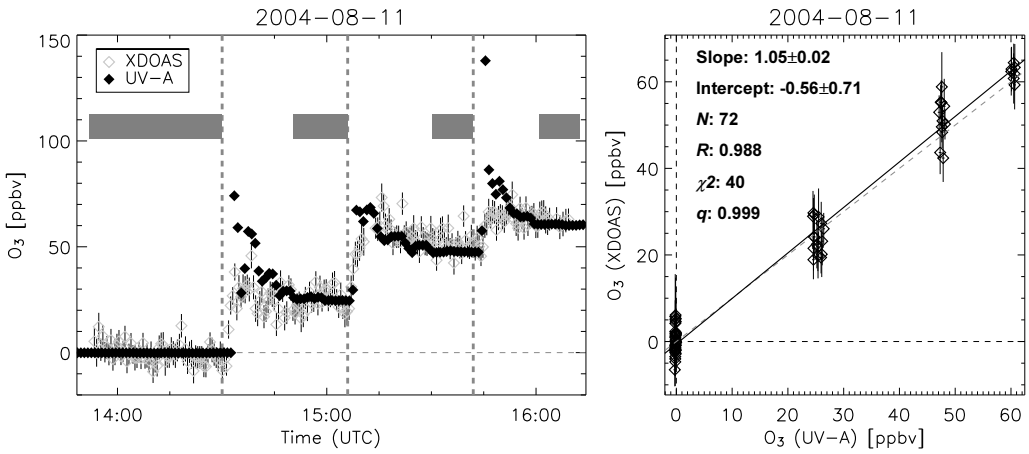

Figure 5.2: *Left panel: profiles of O_3 recorded by XDOAS and UV absorption. Grey vertical lines: O_3 injections. Grey bars: data included in the correlation. Right panel: correlation plot.*

the NO_2 cross section by *Voigt et al* [02] (T = 293 K and P = 1 bar). The right panel of Figure 5.1 shows the correlation and regression of the two concentration-time profiles. The slope of the regression is 1.05. The accuracies of the XDOAS and the CL are given as 6 % and 10 %, respectively. Since the slope cannot be distinguished from unity by the uncertainty level, good agreement between the two instruments can be stated for the investigated range of mixing ratios. The χ^2 of the fit normalised to the measurement errors is a factor of 2.5 higher than the number of data points. Therefore, the quality factor q is virtually zero. A non-linearity between the two instruments is unlikely considering the measurements in a well-defined air mass. The errors of the CL are so small that the errors of the XDOAS govern the statistical analysis. A q close to zero could indicate that the variability of the data around the straight line of the best fit is not explained by the stated errors. The measurement errors of the CL had to be multiplied by a factor of 10 to explain the encountered variance. However, this would mean that the errors of the CL were very badly estimated. The NO_2 measurement errors of the XDOAS had to be multiplied by a factor of only 1.6 to account for the variance, which is a more plausible explanation.

5.1.2 Ozone

An O_3 intercomparison (XDOAS vs UV-A) was performed on 11 Aug 2004 in the purged chamber. O_3 was generated by an external silent discharge ozoniser and then added in three steps (left panel of Figure 5.2). The mixing time of about 20 minutes on that day is easily observable within the UV-A data, whereas concentrations of the XDOAS reach a constant level significantly faster. This feature can be ascribed to the different sampling methods. The XDOAS observes the integrated concentration along the light path

being less sensitive to inhomogeneously composed air masses, whereas the UV-A samples air at the chamber wall.
Injections started at 14:31 UTC. In the spectral analysis the absorption cross sections of O_3 by *Voigt et al* [01] (T = 293 K and P = 1 bar) and $HCHO$ by *Meller and Moortgat* [00], the latter to account for possible remnants of the $HCHO$ experiment the day before (cf section 5.4.1), were included. However, no significant traces of $HCHO$ were found. The slope of the regression line is 1.05.
In addition, an intercomparison of the two instruments was also performed for O_3 concentrations recorded during the ethene-ozone experiments (section 5.4.2) in Feb 2005. On 15 and 17 Feb about 120 ppbv O_3 was added to 150 ppbv ethene in dry synthetic air. On 16 Feb O_3 was added into the chamber in two steps of 60 ppbv each within 30 min (left panel of Figure 5.3). On all days $HCHO$ was present in the chamber in the range from 0 to 15 ppbv, so that the spectral retrieval included the $HCHO$ cross section. The O_3 cross section used here was measured at a slightly different temperature ([Voigt et al 01] at 280 K and 1 bar) being closer to the winter conditions. Here, the slope results in 0.89.
Relative accuracies of the XDOAS and the UV-A are 8 % and 5 %, respectively. In the 11 Aug 2004 experiment both instruments agree well within the uncertainty margin, whereas a significant discrepancy appears in the Feb 2005 measurements. The experimental conditions were not the same in both experiments. On 11 Aug 2004 the ambient temperature was about 25° C higher than during the Feb 2005 experiments. Furthermore, on 11 Aug 2004 O_3 was injected into the otherwise purged chamber with no other trace gases present. Due to the temperature difference, the XDOAS evaluation of the Aug 2004 data was performed with a cross section measured at 280 K, whereas the cross section used for the Feb 2005 data was measured at 293 K. However, the difference in the differential absorption cross sections was determined to be 2 %, which cannot explain the observed discrepancy. On 16 Feb O_3 was added in two steps on a background of 6 ppbv $HCHO$ in the chamber. No $HCHO$ interference with the XDOAS retrieval of O_3 was observed. The inconsistent results of the two experiments remain unresolved to date.

5.1.3 Water Vapour

As part of a larger activity employing several different instruments, a H_2O intercomparison with two DPHs and the XDOAS was conducted from 7 to 8 Apr 2005 at absolute water vapour mixing ratios ranging from 0 to 7.5 ‰. Before the H_2O injections started on 7 Apr 2005, the chamber was illuminated for 35 minutes in order to check, whether one of the instruments responded to a photochemical interference. The XDOAS data reveal rising humidity during daylight exposure (upper left panel of Fig-

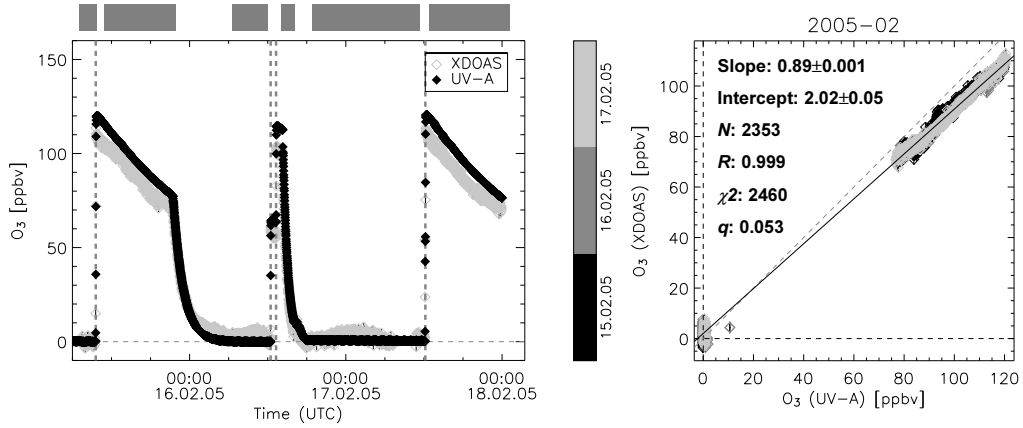

Figure 5.3: *Left panel: O_3 profiles recorded by XDOAS and UV absorption in Feb 2005. Grey vertical lines: O_3 injections. Grey bars: data included in the correlation. Right panel: correlation plot. The days are colour coded.*

ure 5.4). However, due to the thermal forcing the sunlight exerted on the chamber the optical adjustment of the set-up drifted away. Therefore, the XDOAS measurement had to be interrupted for the realignment of the light path marking the previously recorded data with a considerable uncertainty. These data were not included in the comparison. After the daylight exposure period, H_2O vapour from ultra-pure water was added in three steps. Having finished the measurements the chamber was purged for the next day's experiment. On 8 Apr 2005 a considerable amount of H_2O was added once followed by a flushing down to a second very low concentration level. Concentration-time profiles are shown in the left panels of Figure 5.4. In contrast to intercomparisons in 2004, operation of a previously installed fan ensured that H_2O additions were distributed rapidly. The two independent DPHs measured virtually the same concentrations.

Measurements in the red spectral range were performed using grating 2 (Table 4.1). The H_2O high resolution cross section from the HITRAN database [Rothman et al 05] for typical tropospheric conditions was used in the evaluation.

The XDOAS data exceed those of the DPHs by 2 and 3 %, respectively. No accuracy is reported for the HITRAN data. With an accuracy of about 4 % for the DPHs and assuming that the cross section has an accuracy in the range of a few percent, a very good agreement for both regressions is observed. The χ^2 of the two fits is about three times N. Here, the variability of the DPH data is negligible against the scatter of the XDOAS. If the XDOAS error estimation was responsible for this (as discussed before in section 5.1.1), the XDOAS errors of H_2O had to be multiplied by a factor of 1.7.

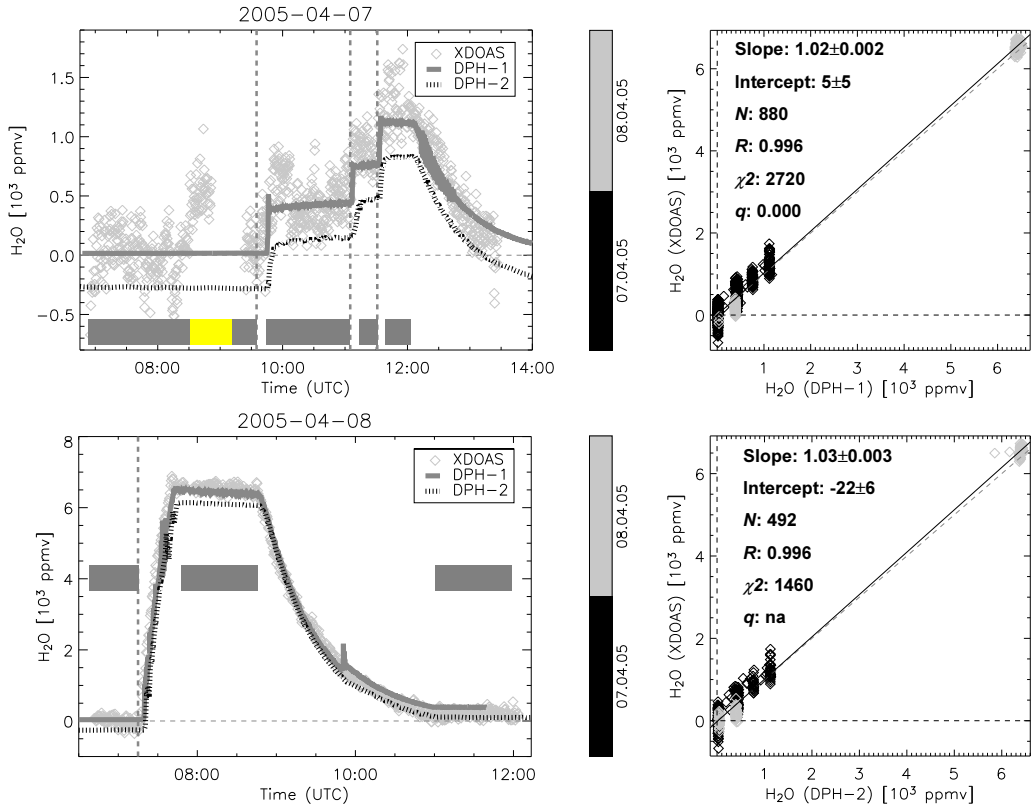

Figure 5.4: *Left panels: profiles of H_2O recorded by XDOAS and two DPHs on 7 Apr (upper) and 8 Apr (lower) 2005. Grey vertical lines: water vapour injections. Yellow bar: period of daylight exposure. Grey bars: data included in the correlation. The data of DPH-2 were displaced by −300 ppmv for clarity. Right panels: correlation plot of XDOAS against DPH-1 (upper) and DPH-2 (lower). The days are colour coded.*

5.1.4 Nitrous Acid

A HONO intercomparison (XDOAS vs LOPAP) was carried out on 16 Jun 2004 (Figure 5.5). Nitrous acid was generated by the photochemical source found in the SAPHIR chamber under daylight exposure. As the HONO formation potential is greater with growing humidity, H_2O was added to the chamber before the illumination until approximately 85 % relative humidity had been reached. When the chamber volume was exposed to daylight at 10:00 UTC, HONO levels grew strongly. Thereby, LOPAP concentrations rose immediately after daylight exposure, followed by XDOAS concentrations with a delay of ca 5 min. The gap in the XDOAS data between 11:53 UTC and 13:32 UTC was caused by a realignment of the optical mounts, which was required due to a thermal drift. The gaps in the LOPAP data denote the time, when a zero reference was taken. Later, when it seemed that HONO levels would not rise any further, more H_2O was added to the chamber. Later in the afternoon about 25 ppbv NO_2 were added to

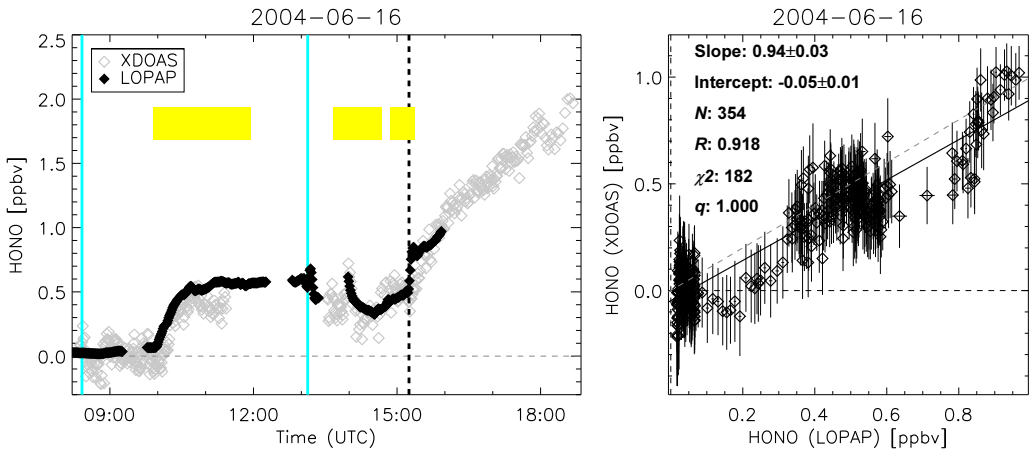

Figure 5.5: *Left panel: profiles of HONO measured by XDOAS and LOPAP. Blue vertical lines: water vapour injections. Yellow bars: periods of daylight exposure. Dashed vertical line: NO_2 injection. Right panel: correlation plot.*

enhance the HONO formation rate. HONO levels kept on growing after the final closure of the shutters, a feature that had been observed many times before *.
In the evaluation, the cross sections of NO_2 [Voigt et al 02] (T = 293 K and p = 1 bar) and HONO [Stutz et al 00] were included.
LOPAP HONO levels rose earlier than those of the XDOAS. The assumption of a homogeneous air mass in the chamber does not hold completely, when shutters are open. The influx of radiation causes thermal gradients leading to air convection. Moreover, the illumination of the chamber is not equal in every place, since some parts are shadowed by the metal frame. The XDOAS is a path-integrative measurement technique. The light path itself is directed along the axis through the centre of the chamber, about 2 m away from the walls. In contrast, the LOPAP technique is an extractive point measurement. Air is sampled at the chamber wall through an inlet manifold. As

- the walls are very likely involved in HONO formation [Rohrer et al 05],
- the probed air is not necessarily representative of the air mass in the chamber and
- the two sampling methods differ,

deviations from a unity correlation are not surprising. Notwithstanding, the two instruments agree very well within the uncertainty margins (slope: 0.94; accuracies XDOAS: 6 %, LOPAP: 10 %), so that the aspects considered above had no great effect on the correlation and regression. However,

*Personal communication from Rolf Häseler

Table 5.1: *Measurement settings of the internal instrument intercomparisons at SAPHIR.*

DATE	ABSORBER	GENERATION	RANGE [ppbv]	ACQUIS. [a] TIME [s]
2004-06-03	NO_2	injected	0–50	≈ 40
2004-08-11	O_3	injected	0–70	≈ 30
2005-02-15/17			0–120	≈ 60
2005-04-07	H_2O	injected	0–2×10^6	≈ 20
2005-04-08			0–7×10^6	
2004-06-16	HONO	photochem.	0–1.5	≈ 50

[a] Of the XDOAS

the χ^2 is smaller than N. In turn, q is close to unity. The LOPAP errors are small against the XDOAS errors. Resuming the discussion of measurement errors in sections 5.1.1 and 5.1.3, this would indicate that the XDOAS errors of HONO had been overestimated by a factor of 1.4.

5.1.5 Summary of Intercomparisons

The intercomparisons presented here covered NO_2, HONO, O_3 and H_2O (Table 5.1). Aside from HONO, all of these species were injected into the chamber. HONO was generated by a photochemical mechanism. Mixing ratios were chosen to allow a unambiguous detection. For example, H_2O is a comparatively weak absorber featuring a peak differential cross section around 651.6 nm of 7.5 10^{-25} cm^2 at a resolution of 0.34 nm contrasting its high abundance in the atmosphere, with peak mixing ratios reaching several percent. In contrast to that, concentration levels of HONO were rather low ($<$ 2 ppbv), which is due to the limited production rate of the photochemical chamber source. In general, the intercomparisons were performed in regimes encountered in the troposphere. The settings of the XDOAS instrument allowed data acquisition at a time resolution of less than a minute.
To obtain highest sensitivity the wavelength ranges featuring the highest differential cross sections, accessible with the apparatus, were chosen for the spectral retrieval. For example, the differential absorption cross section of NO_2 is highest in the region beyond 450 nm. However, it was retrieved between 400 and 450 nm since above that the light source features strong Xenon emission peaks, which would have adversely affected the analysis. O_3 was studied from 306 to 350 nm, not being the range with highest sensitivity, to ensure the accuracy of the literature cross sections in a range where other species of interest (eg HCHO and HONO) are detected.
The literature absorption cross section is the main contributor of uncer-

tainty to the DOAS evaluation and as such usually covers the range of several percent for an individual work. However, regarding comparisons of different reported cross sections, a greater variance is encountered. The ratio of the largest to smallest differential absorption cross section results in, determined using a non-linear least squares fitting method, 1.08 for NO_2 at 295 K [Orphal 03], 1.10 for O_3 at 295 K [Orphal 03], and 1.78 for $HONO$ [Stutz et al 00]. No accuracies are given for the H_2O cross section. In the SAPHIR intercomparisons the deviations of a unity regression stayed in the range implied by the literature cross sections for NO_2 and O_3. The 6 % discrepancy encountered in the $HONO$ comparison indicates that the scaling of the differential absorption cross section of $HONO$ by *Stutz et al* [00] used for the DOAS evaluations is correct within the uncertainty limit.
The different instruments exhibit high correlation coefficients towards the XDOAS with values greater than 0.92. The instruments are assumed to have probed the same air mass. The good linearity between the independently measured data gives evidence for the stable and homogeneous conditions the simulation chamber provided. The slopes of the regressions cannot be distinguished from unity within the accuracy limits. Significant discrepancies were encountered only in the O_3 comparison of Feb 2005. The intercepts of the regressions are not always as close to zero as anticipated from the error calculated from the data scatter. Nonetheless, they are much smaller than the precision of an individual data point indicating a non-statistical origin. In that respect, the sampling methods and settings of the different instruments should be scrutinised in more detail. The regression parameters (q, χ^2) indicated that for some compounds (NO_2, $HONO$, H_2O) the estimation of the XDOAS error did not match the observed data variability. Errors had been calculated by multiplying the DOAS fitting error by a factor of 2, derived empirically from earlier measurements of O_3 and $HCHO$. Another more promising approach would be to base the error on a statistical analysis of the fit residual for each evaluated spectrum individually [Hausmann et al 99]. The implementation of this algorithm remains a task for future improvements of the analysis procedure.

5.2 SAPHIR as a Calibration Platform

In order to validate the detection methods for oxygenated volatile organic compounds, the OVOC intercomparison within the ACCENT [†] framework was conducted from 24 to 28 January 2005 at the Forschungszentrum Jülich with twelve participating research groups from six countries. 16 compounds were chosen for the intercomparison (formaldehyde, acetaldehyde, butanal, hexanal, methanol, ethanol, 1-propanol, 1-butanol, methacrolein, methyl vinyl ketone, acetic acid methyl ester, acetone, benzaldehyde, 2-methyl-3-buten-2-ol, n-butane and toluene, whereby the last two served as tracers for dilution processes at SAPHIR and as reference compounds for the gas chromatographs). From these 16 substances formaldehyde, benzaldehyde and toluene were retrieved by the XDOAS.

Experimental

Each night the chamber was flushed to remove possible remnants of previous experiments below the limits of detection. On 24 Jan blind measurements in synthetic air with the subsequent addition of H_2O and O_3 were conducted. The additions served to determine interferences with the involved instruments. On the days 25 to 27 Jan specified initial amounts of each compound were injected in the morning within half an hour. The schedule provided three hours of measurements, then about one hour of flushing the chamber to a lower concentration level, again three hours of measurements, one hour of flushing again to the final level and the last three hours of measurements. Exact quantities and flushing rates were selected by and only known to the referee. Prior to the campaign it was agreed that initial mixing ratios would be in the range between 4 and 8 ppbv for each compound. The experiment on 25 Jan was performed in pure synthetic air. On 26 and 27 Jan H_2O and H_2O with O_3 were added, respectively, in order to detect possible interferences. On 28 Jan, the chamber was not flushed with clean synthetic but with ambient air to simulate ordinary winter term boundary layer conditions. On that day only one concentration level was studied.
The three substances detected by the XDOAS absorb in different wavelength intervals. Therefore, they were retrieved in different wavelength ranges. Measurements were done using grating 1 (cf Table 4.1). The measurement algorithm alternated between the two required ranges. Below a wavelength of 300 nm the White cell was operated at a total path of 320 m to obtain sufficient light transmittance.
For many absorbers (eg NO_2 or O_3) high resolution literature cross sections are available. However, the best available absorption cross sections

[†] Atmospheric Composition Change - the European NeTwork of excellence

of benzaldehyde and toluene [Etzkorn et al 99] were determined at a resolution similar to that of the XDOAS at SAPHIR [‡]. To adapt resolutions a de-convolution method was applied (cf Appendix B).
Apart from the direct instrument intercomparison measured data were compared to calculated data. For that purpose, initial concentrations in the chamber were computed from the sample weights of the injected compounds. The fate of the injections was calculated taking into account the dilution coefficient. Concentrations could not be calculated on the last day due to the flushing with ambient air of unknown composition.
As the OVOC campaign was a blind intercomparison, the data of the other participating instruments, all extractive techniques sampling from the same line, were not available for presenting them in this thesis. A preliminary regression result of benzaldehyde, toluene and formaldehyde is shown in Figure 5.6 [§]. As can be seen the maximum deviation amounts to a factor of about 2.5 for each compound. A more detailed discussion based on the highly resolved time profiles of the instruments will be published soon [¶]. In the following the XDOAS analysis and results are discussed with respect to the calculated values.

Analysis

For toluene (265–273 nm), an analysis setting different from that of benzaldehyde (273–286 nm) was chosen, because slight misalignments of the wavelength calibration occurred when a retrieval with linked benzaldehyde and toluene was executed. This indicates that the reported wavelength-to-pixel mapping of one of the absorbers was not correct. As the benzaldehyde cross section aligned well to the one of O_3 [Voigt et al 01], which had been confirmed previously [Orphal 03], it is suggested to shift the toluene cross section by $+0.2$ nm. Other absorbers like benzaldehyde, $HCHO$, O_3 or NO_2 were introduced when necessary. It turned out that $HCHO$ and NO_2 were too weak to be detected from 265 to 286 nm. No benzaldehyde and toluene data were recorded on 24 Jan in the blank experiment.
The $HCHO$ retrieval was performed under different analysis settings (310–350 nm). Due to a technical problem of the spectrograph's thermostat the $HCHO$ data from 25 and 26 Jan were of low quality, which rendered them useless for the comparison.

Benzaldehyde

Due to the high differential absorption cross section with a prominent band at about 284.1 nm (3.6×10^{-18} cm^2 at the resolution of the XDOAS) the

[‡]FWHM of 0.15 nm in the literature compared to 0.17 nm in this thesis
[§]Personal communication from Theo Brauers
[¶]Personal communication from Eric Apel, Rainer Steinbrecher and Armin Wisthaler

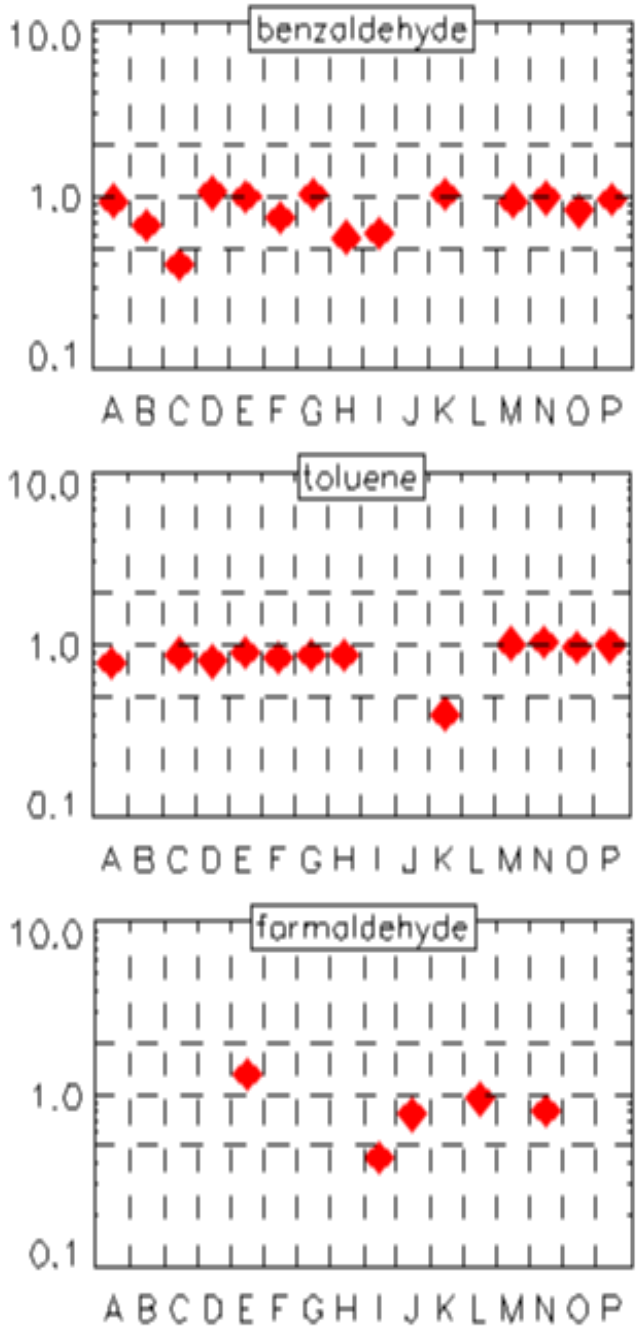

Figure 5.6: *Preliminary regression results (instrument vs calculation) of benzaldehyde (upper panel), toluene (centre panel) and formaldehyde (lower panel) during the OVOC campaign. Each letter denotes an instrument (E: XDOAS). Y-axis: slope of a regression forced through the origin.*

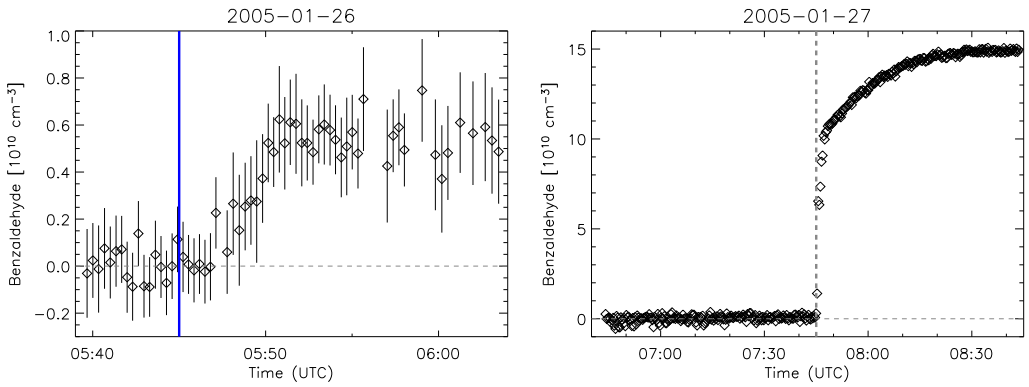

Figure 5.7: *Left panel: benzaldehyde concentration on 26 Jan measured by the XDOAS indicating a significant increase before first injections into the previously purged chamber started. Blue line: beginning of water vapour injection. Right panel: benzaldehyde time profile before and after the injection on 27 Jan. Grey vertical line: benzaldehyde injection. It took an hour for benzaldehyde concentrations to reach the final level.*

signal-to-noise ratio allowed a high precision measurement in the mixing ratio regime of a few ppbv. The time resolution of the order of 20 s allowed the observation of, so far unreported, chamber characteristics during the injection procedures, which are described in the following.
On Wednesday, 26 Jan, during injection of H_2O benzaldehyde levels rose by about 0.5×10^{10} cm^{-3} or 200 pptv (left panel in Figure 5.7). This feature might indicate that a reservoir, most likely in the condensed phase, had been formed somewhere in the chamber or in the chamber supply lines in previous experiments. The benzaldehyde rise was not taken into account for the calculated data of that day. Therefore, these data are endowed with an additional uncertainty of 5 % comparing the observed artifact to the amount of injected benzaldehyde.
The reservoir hypothesis is corroborated by the behaviour the benzaldehyde exhibited during injection on 27 Jan (right panel of Figure 5.7). On that day, it took almost one hour for the aromatic to be flushed into the chamber completely. Liquid benzaldehyde was injected into a stream of clean and dry synthetic air, so that evaporation should have happened fast. However, assuming that some of the liquid injection settled on the walls of the inlet tubing, eg in a fissure of the material where exposure to the air stream was lowered, could account for the delay. In the morning of 28 Jan the chamber was flushed with ambient air for the last experiment. No benzaldehyde was detected on that morning.
Correlations and regressions of measurement vs calculation are shown in the upper right panel of Figure 5.8. Data of the ambient air experiment were not included. The first mixing ratio level on 27 Jan was omitted due to the delayed distribution of the injection as discussed. Despite the additional uncertainty of 5 % for the 26 Jan calculated data, XDOAS and calcu-

lation are in good accord (slope: 1.03±0.001, intercept: (−0.03±0.003) ppbv, N=1783, χ^2=1490, R=0.999).

Toluene

The toluene injections were of the same order of magnitude as the ones of benzaldehyde. Since the differential absorption cross section is smaller by a factor of 10 than that of benzaldehyde the precision of the XDOAS is accordingly lower being visible in the larger scatter of the toluene data. This larger scatter rendered the XDOAS not sensitive enough to observe a significant rise in toluene levels in the morning of 26 Jan during H_2O injection, if there had been one. In contrast to benzaldehyde the injected toluene was mixed in the chamber almost instantly in the morning of 27 Jan. A feature that could be attributable to the considerably higher vapour pressure of toluene in comparison to benzaldehyde. The last day's experiment revealed that about 2.4 ppbv of toluene were present in ambient air at that time.
The graphs (centre row) in Figure 5.8 demonstrate that measured data of 26 and 27 Jan agree quite well with the calculation, whereas the data of 25 Jan appear to be displaced upward (slope: 1.19±0.008, intercept: (-0.67±0.03) ppbv, N=1942, χ^2=2500, R=0.938). The reason for this inconsistency between three days within one campaign is not apparent. However, one has to account for the uncertainty of the injected toluene sample, which is of the order of 10 %. To put this finding in a more general picture, the data recorded by the other instruments during OVOC have to be considered.

Formaldehyde

Due to a technical problem of a thermostat the XDOAS $HCHO$ data of days 25 and 26 Jan were of low quality and therefore not suitable for the intercomparison. The injection of $HCHO$ differed from the other OVOCs insofar, as it was not evaporated from a liquid but rather thermolysed from paraformaldehyde powder to the gas-phase by heating (cf section 5.4.1). The concentration-time profile of the 28 Jan reveals that the $HCHO$ level in ambient air was significantly lower than one ppbv.
The correlation turned out to be very good (N=336, χ^2=184, R=0.991). The intercept of (−0.05±0.02) ppbv is small. However, the regression in the lower right panel of Figure 5.8 exhibits a much higher slope (1.35±0.01) than expected from the calculations. Assuming that the XDOAS measurement is correct, this behaviour would occur when the weight of the injected para-formaldehyde sample had been underestimated by the corresponding

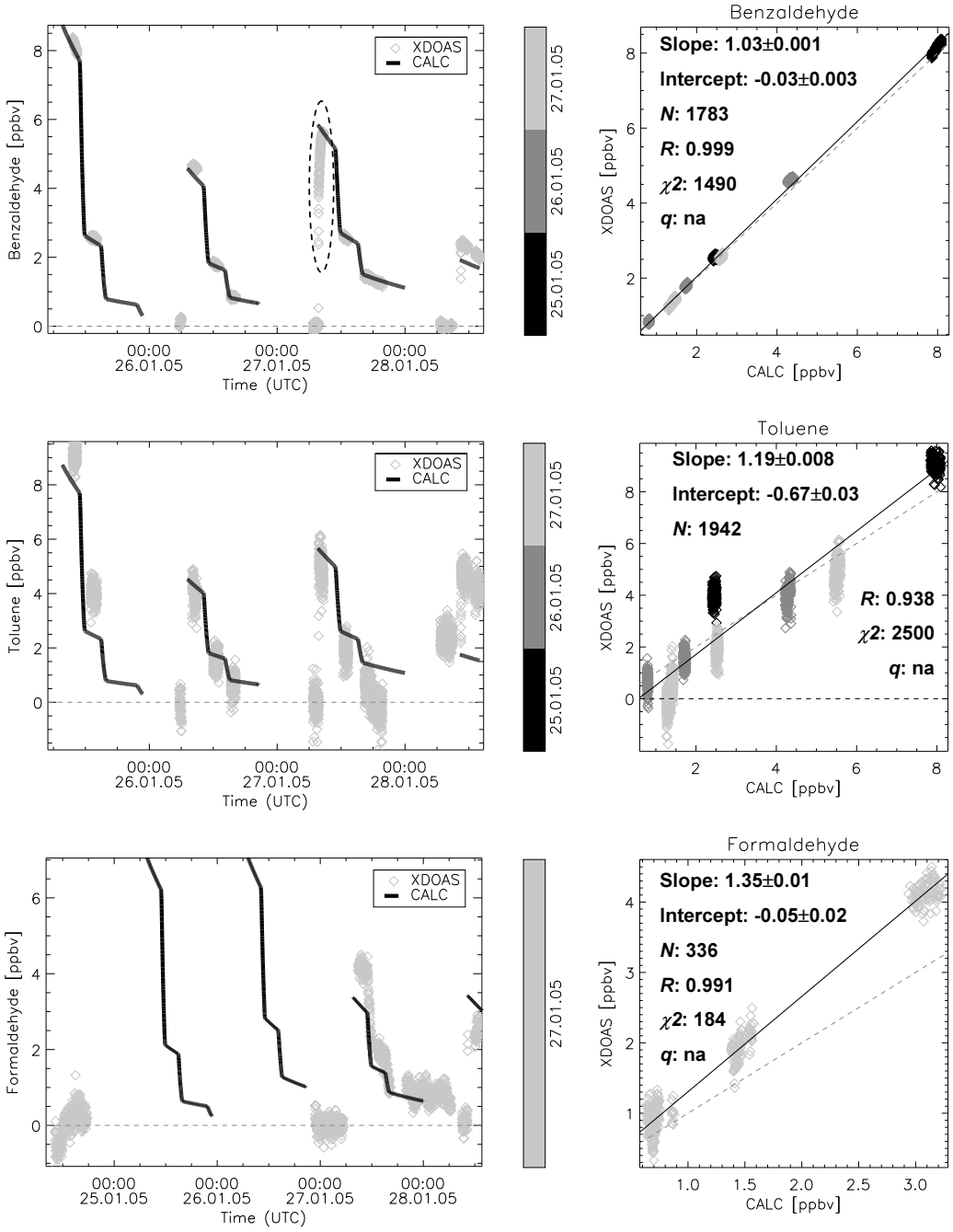

Figure 5.8: *Left panels: concentration-time profiles of benzaldehyde (upper), toluene (centre) and formaldehyde (lower) measured by XDOAS and calculated (CALC) from injection and replenishment flow data. Benzaldehyde data in the dashed ellipse were not included in the correlation. Right panels: correlation plots of XDOAS vs calculation.*

factor. However, as with the discrepancy found in the toluene data, conclusions can be drawn only when the data of the other participating instruments are considered.

5.3 The HO_XCOMP Campaign

The HO_xCOMP campaign within the ACCENT framework served to validate measurements of hydroxyl and hydroperoxy radicals (HO_x) conducted by international research groups using several independent instruments. For that reason, experiments under various conditions were carried out from 4 to 23 Jul 2005 in ambient air and in the SAPHIR chamber on the campus of the Forschungszentrum Jülich.

Experimental

The experiment performed on 23 Jul 2005 was designed to derive the concentration of photochemically produced hydroxy radicals from the loss of chemical reactants, which were quantified by independent measurement techniques. For that purpose, a mixture of several hydrocarbons (benzene, 1-hexene, m-xylene, n-octane, n-pentane and isoprene at about 5 ppbv each), which fate was determined by dilution and OH reaction only, was injected into the humid chamber. Small amounts of NO (1.5 ppbv) and O_3 (20 ppbv) were also added. From the injected compounds benzene and m-xylene were retrieved by the XDOAS, and compared to the results of a gas chromatograph (left panels of Figure 5.9), which is part of SAPHIR's standard instrumentation. The gap in the XDOAS time profile was caused by a realignment of the optical set-up.
The cross sections of $HCHO$ [Meller and Moortgat 00], O_3 [Voigt et al 01] at 293 K and 1000 mbar, benzene and m-xylene [Etzkorn et al 99] were included in the analysis. Since the resolutions of the literature cross sections of the aromatics are similar to the one of the XDOAS, an FFT algorithm was applied for the adaptation (cf Appendix B).

XDOAS vs GC

The right panels of Figure 5.9 show correlations and regressions of the two measured concentration-time profiles. Due to the 30 min long enrichment time of the GC, the XDOAS data were sampled onto the GC time grid. Correlation coefficients are close to unity for both aromatic compounds. The slopes deviate by 4 % downward from unity for benzene and 13 % upward for m-xylene. Accuracies of the XDOAS measurement of benzene and m-xylene are 8 % and 5 %, respectively. The accuracy of the GC is stated as 8 %. In contrast to other instrument intercomparisons at SAPHIR (section 5.1), the precision of the slopes is rather high yielding 19 % (benzene) and 5 % (m-xylene), which is due to the low number of GC samples. A significant difference between the two instruments, based on the small sample of seven data points, is not observed.

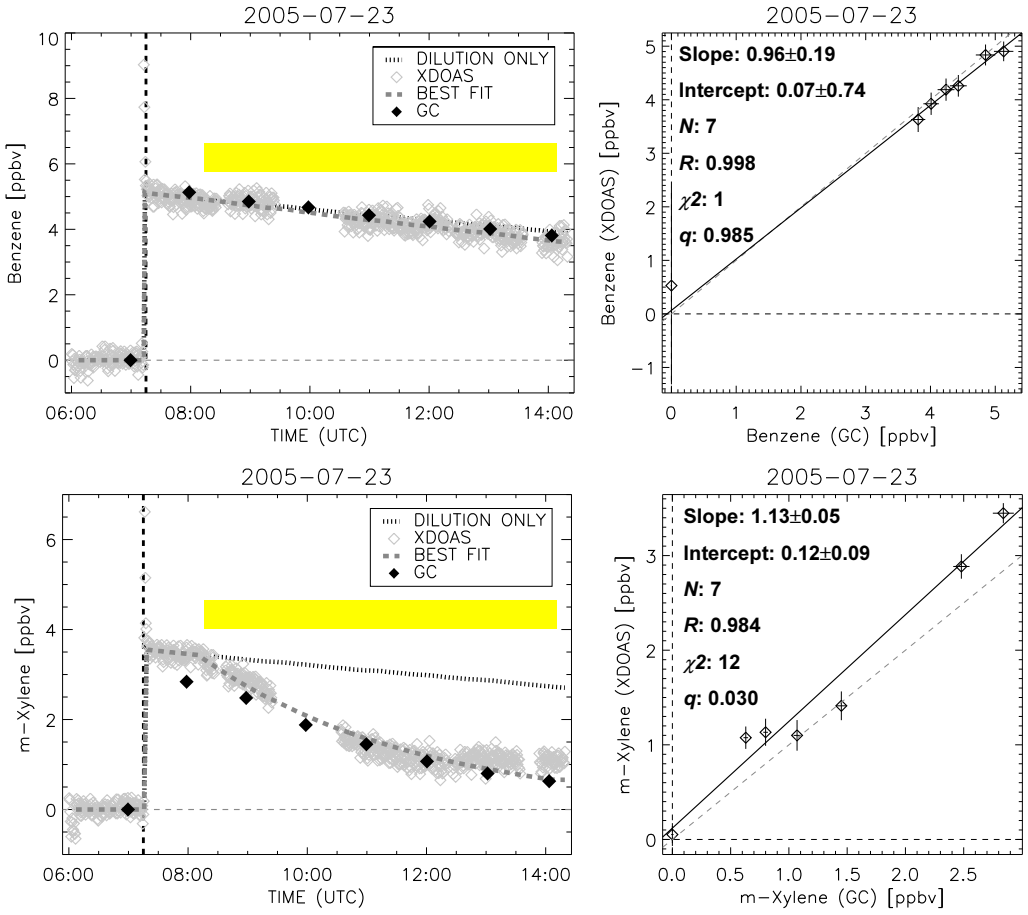

Figure 5.9: *Left panels: profiles of benzene (upper) and m-xylene (lower) recorded by XDOAS and GC and two model results, one assuming a dilution-only scenario, the other applying a fit to the XDOAS data assuming a constant OH concentration under daylight exposure. Black dashed vertical line: time of injection. Yellow bar: period of daylight exposure. Right panels: correlation plots of XDOAS vs GC for benzene (upper) and m-xylene (lower).*

5.3.1 Calculating the Average Hydroxyl Radical Concentration

Measured concentration-time profiles of the two aromatics allowed to calculate an average OH radical concentration in a pseudo-first-order decay approach from the rate coefficients of the OH-hydrocarbon reaction using a simple scenario considering only the dilution and the OH reaction.

$$-\frac{d[\text{Aromatic}]}{dt} = -\left(k_{\text{Dil}} + k_{\text{OH}} \times \delta \times \overline{[\text{OH}]}\right) \times [\text{Aromatic}] \tag{5.1}$$

k_{Dil} represents the dilution coefficient, which was monitored accurately by a mass flow controller. It was imposed on the calculation from the measurement. Exposure of the chamber to daylight initiated the production of OH radicals. Therefore, the parameter δ was set to unity under illumination. Beyond that, is was set to zero. Concentrations were calculated on a grid of 30 s. Rate coefficients of the reactions

$$\text{OH} + \text{Benzene} \longrightarrow \text{Products} \tag{5.2}$$

$$\text{OH} + \text{m} - \text{Xylene} \longrightarrow \text{Products} \tag{5.3}$$

were adopted from *Witte et al* [86] for reaction (5.2) ($2.3\times10^{-12}\times\exp(\text{-}190/T)$ cm^3 s^{-1}) and *Atkinson and Aschmann* [89] for reaction (5.3) (2.3×10^{-11} cm^3 s^{-1}). Initial amounts of the hydrocarbons were estimated by extrapolation of the XDOAS data to the time of injection, which resulted in 5.1 ppbv for benzene and 3.6 ppbv for m-xylene. A weighted least squares fit of calculated to measured data, with $\overline{[\text{OH}]}$ as variable, was applied to benzene and m-xylene separately. Results for the daylight exposure period were $(2.8\pm0.4)\times10^6$ cm^{-3} (m-xylene) and $(3.0\pm1.0)\times10^6$ cm^{-3} (benzene). The uncertainty must be regarded as an estimation, since the assumption of a constant hydroxyl radical concentration did not match the exact concentration-time profile on a day with ragged cloud cover. Between 13:00 and 14:00 UTC of that day the cloud cover was particularly solid, so that OH levels and the corresponding aromatic turnovers were low. The uncertainty of the benzene fit is larger than that of the m-xylene calculation since the turnover of benzene by OH is slow compared to the dilution. The accuracies of m-xylene (5 %) and benzene (8 %) measurements were included in the estimation as well as the uncertainties of the rate coefficients (OH-m-xylene, 7 %, and OH-benzene, 20 %) and the chamber properties (3 %).
The mean OH concentration measured by the LDOAS in the daylight exposure period was calculated as $(2.9\pm1.3)\times10^6$ cm^{-3} being in perfect agreement with the result deduced from the XDOAS data. The uncertainty of the LDOAS reflects the 1σ RMS of the data against the mean and demonstrates the high variability of the OH concentration on that day. A more extensive discussion of the OH measurements during the HO_xCOMP campaign will be published soon [‖]. The good accord between measured and

[‖] Personal communication from Eric Schlosser

calculated average OH concentration demonstrates that trace gas levels in the chamber can be computed from independently measured data, when the kinetic parameters are known accurately.

5.4 Formaldehyde Experiments

5.4.1 Generation of Gaseous Formaldehyde by Thermolysis

In this section measurements of $HCHO$ conducted in 2004 (6 Jul and 10 Aug) and 2005 (16 Feb) in the dark and previously purged chamber are presented. $HCHO$ was retrieved by the XDOAS, the Hantzsch monitor and the Laser-DOAS.

Experimental

In all three experiments $HCHO$ was generated by heating a weighted amount of solid para-formaldehyde until it was thermolysed completely. The resulting gas was flushed into the chamber by high purity N_2 ($>$ 99.9999 %). The thermolysis temperature was reached after 10 to 20 minutes (120 to 170° C at standard pressure). At that point, the transition into the gas-phase occurred within seconds. In the experiments in 2004 a homogeneous concentration level in the chamber was reached after the characteristic mixing time (cf Table 3.1). In 2005 a fan was operated, which distributed the injection in the chamber almost instantly. After the injection the chamber was purged twice for several minutes during the experiment in order to dilute the $HCHO$ and thus to cover a broader dynamic range. O_3 was added in two steps on the lowest $HCHO$ level in the 16 Feb 2005 experiment to test the instruments for a possible O_3 interference (with the Hantzsch described by *Krinke* [99]). However, $HCHO$ data of neither XDOAS nor Hantzsch responded to the O_3 addition. Figure 5.10 shows concentration-time profiles of the Hantzsch and the XDOAS instrument. The Hantzsch data appear as a solid line in the figure due to the excellent precision of this detection method. The XDOAS data from 10 Aug 2004 exhibit a larger scatter compared to the other days. Nonetheless, the evaluation procedure revealed no evidence for these data to be corrupt, so that they were included in the comparison. The lower precision on that day might have been caused by artificial structures introduced into the spectra by the already aged Xenon short arc lamp. LDOAS data are not shown, as the differential optical absorption cross section around 308.1 nm at the high resolution of the LDOAS is not known. In the following the LDOAS data are discussed on a relative scale. The $HCHO$ absorption structure in the XDOAS spectra was identified using the well established cross section by *Meller and Moortgat* [00] at 298 K.

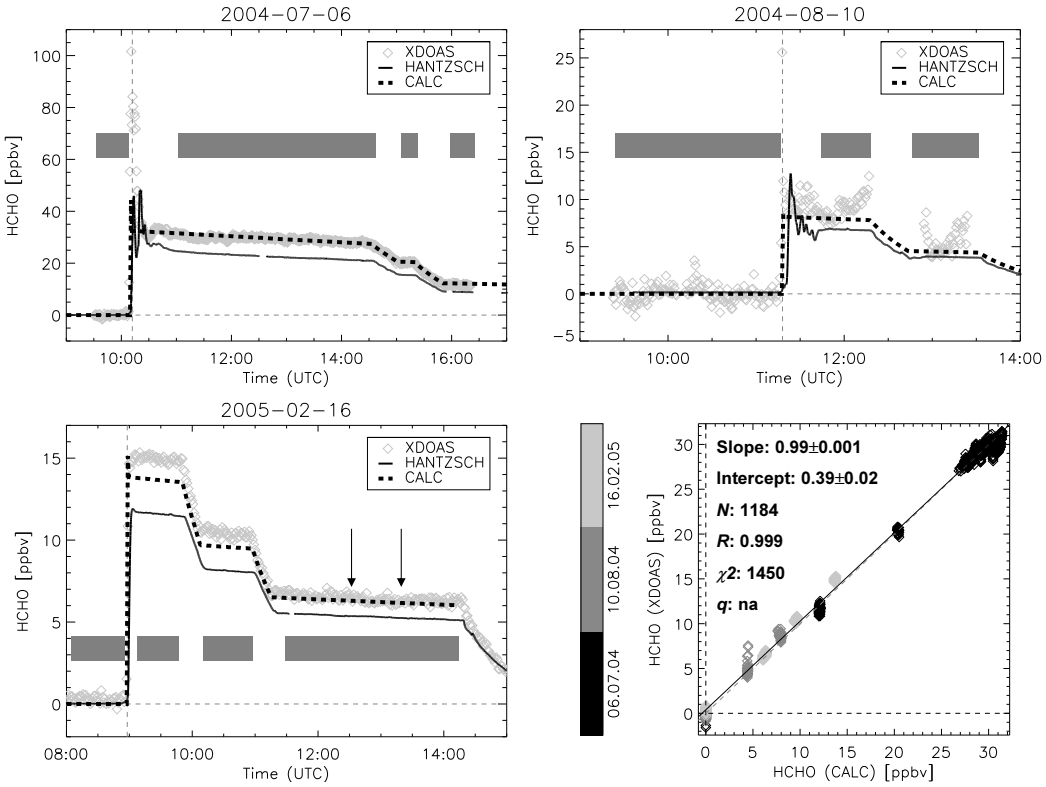

Figure 5.10: *Upper left panel: HCHO profiles on 6 Jul 2004 as measured by XDOAS and Hantzsch, and as calculated. Grey vertical line: HCHO injection. Upper right panel: data from 10 Aug 2004. Lower left panel: data from 16 Feb 2005. Arrows: ozone additions. Grey bars: data included in the correlation. Lower right panel: correlation plot. The days are colour coded.*

Calculated HCHO Concentrations

HCHO concentrations were calculated in steps of 60 seconds. For the calculation, the centre of the injection period was used as injection time to generate comparable data sets. Initial concentrations were deduced from the weighted para-formaldehyde (Sigma-Aldrich, stated purity $>$ 95 %; 10.91 mg on 6 Jul 2004, 2.66 mg on 10 Aug 2004 and 5.00 mg on 16 Feb 2005 corresponding to 32.5 ppbv, 8.2 ppbv and 13.9 ppbv, respectively) assuming that it did not contain impurities and that the gas-phase HCHO yield in the chamber disregarding potential line losses was 100 %. From the purity and the accuracy of the chamber volume an accuracy of the initial mixing ratio of the injection of 6 % is estimated (cf Appendix C.1). The fate of HCHO in the chamber was governed by dilution.

$$-\frac{[\mathrm{HCHO}]}{dt} = k_{\mathrm{Dil}} \times [\mathrm{HCHO}] \tag{5.4}$$

Small data gaps in the gas flows were filled applying a linear interpolation.

XDOAS vs Calculation

The calculated $HCHO$ values were interpolated linearly on the XDOAS time grid. Joint correlation and regression of the three experiments are shown in the lower right panel of Figure 5.10. 1184 data points were available. The calculation and the XDOAS data exhibit good agreement (slope: 0.99$\pm$0.001, intercept: (0.39$\pm$0.02) ppbv, N=1184, R=0.999, χ^2=1450). The intercept is above zero significantly. Data from 16 Feb 2005 exhibit a slightly higher slope than data from summer 2004. The temperature, at which the experiments were performed, differed about 25° C between summer 2004 (25-30° C) and winter 2005 (0-5° C). The absorption cross section of $HCHO$ is temperature dependent. This dependence for the spectral range of interest here was studied by *Meller and Moortgat* [00] and *Cantrell et al* [90]. Although the response of the $HCHO$ cross section on a temperature change agreed in the two studies, a discrepancy in the magnitude occurred. Whereas the *Meller and Moortgat* [00] cross section decreases by 1 % over a temperature drop of 25° C, the *Cantrell et al* [90] cross section goes down by 7 % (cf Appendix C.3). *Cantrell et al* [90] used $HCHO$ prepared and stored at 77 K prior to the measurement. *Meller and Moortgat* [00] demonstrated in their report that this kind of storage adversely affected the reproducibility of the measurements by polymerisation effects. In conclusion, the *Meller and Moortgat* [00] cross section is assumed to be more reliable and therefore their temperature dependence is adapted here. However, due to its small magnitude, the effect of their temperature dependence can be neglected. The precision of the weighted sample for each day was not considered in the evaluation. Regarding the accuracies of the XDOAS measurement (11 %) and of the injection (6 %), in three different thermolysis experiments conducted over a period of seven months the paraformaldehyde yielded a constant gas-phase $HCHO$ level in the chamber. As measured data match the calculation, which was obtained from basic assumptions, very well, it is concluded that the scaling of the *Meller and Moortgat* [00] $HCHO$ cross section (discussed in Appendix C.2) is consistent with the findings at SAPHIR.

LDOAS vs Calculation

Laser-DOAS data are available for two of the three thermolysis experiments. Calculated values were interpolated on the LDOAS acquisition time grid of 2 minutes. The correlation and regression are shown in the upper left panel of Figure 5.11. The LDOAS data are described by a straight line accurately with a correlation coefficient of unity on the sample of 113 data points. The fit confirms that the gas-phase $HCHO$ yield at SAPHIR has been constant over several months, as observed by the XDOAS. In that respect, the two spectroscopic techniques and the calculation are in very good

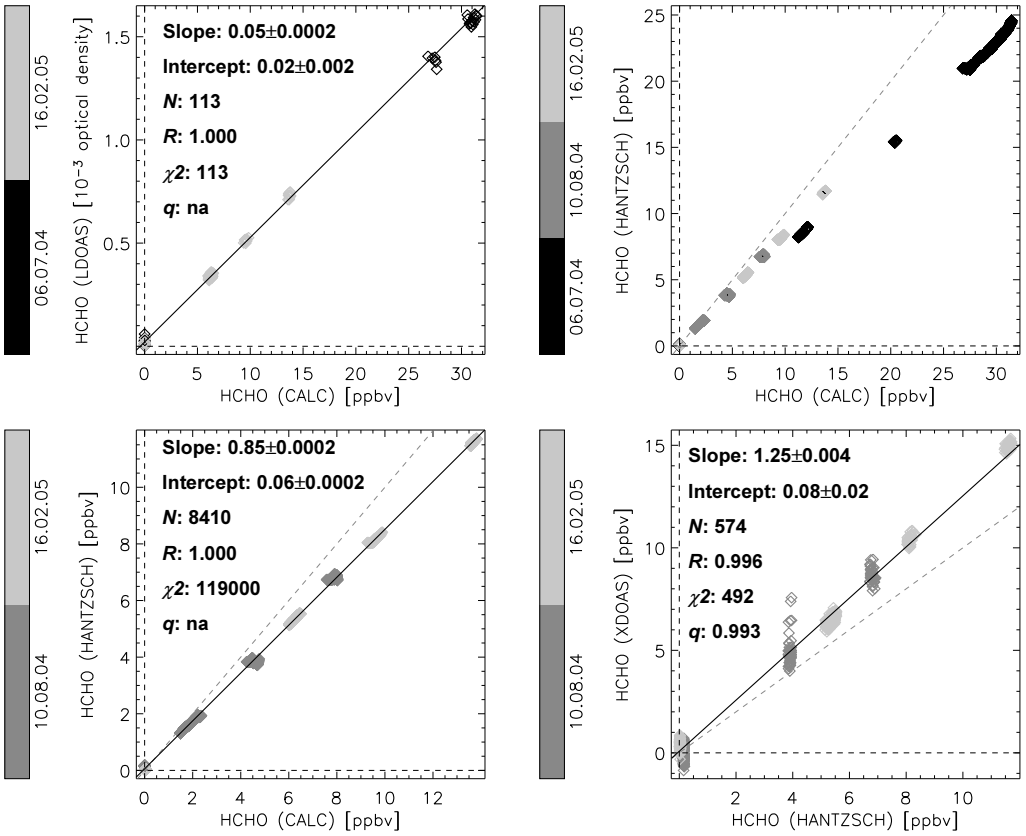

Figure 5.11: *Upper left panel: correlation plot of LDOAS vs calculation. LDOAS data in optical densities. Upper right panel: Hantzsch vs calculation, all days. Lower left panel: Hantzsch vs calculation, two days only. Lower right panel: XDOAS vs Hantzsch for two days. The days are colour coded.*

accord. From the slope of the regression the differential absorption cross section at the high resolution of the LDOAS around the 308.1 nm range was calculated as 8.9×10^{-21} cm^2. The corresponding accuracy is approximately 6 %.

Hantzsch vs Calculation

The Hantzsch data from 6 Jul 2004 (upper right panel of Figure 5.11, black diamonds) show a distinctly different slope compared to days 10 Aug 2004 and 16 Feb 2005. On that day the instrument was run at higher sensitivity of the photomultiplier tube to avoid a non-linear response signal at the comparatively high initial mixing ratio of 33 ppbv. As the origin of this discrepancy is still under investigation, the data from 6 July are not considered in further correlation and regression analyses. For that reason, in the lower left panel of Figure 5.11 the correlation and regression of the Hantzsch against the calculation for the two remaining days

are presented (slope: 0.85±0.0002, intercept: (0.06±0.0002) ppbv, N=8410, R=1.000, χ^2=119000). Regarding the stated accuracy of the Hantzsch instrument (3 %), calculation and measurement do not agree.

XDOAS vs Hantzsch

As the precision of the Hantzsch is better than that of the XDOAS, the Hantzsch data were sampled onto the XDOAS time grid (lower right panel of Figure 5.11). The Hantzsch data from 6 Jul 2005 were excluded from the regression due to the unaccountable behaviour the Hantzsch exhibited on that day (slope: 1.25±0.004, intercept: (0.08±0.02) ppbv, N=574, R=0.996, χ^2=492, q=0.993). The correlation coefficient is 0.996, which is higher than found in previous field intercomparisons of the two detection methods [Lawson et al 90, Cárdenas et al 00, Grossmann et al 03, Hak et al 05] (Table 5.2). The Hantzsch data underestimate the XDOAS data by a factor of 0.8. Accordingly, the observed discrepancy cannot be explained by the accuracies of the two instruments (XDOAS: 11 %, Hantzsch: 3 %) alone indicating another systematic error.

Discussion of the Thermolysis Experiments

Previous HCHO intercomparisons of a Hantzsch monitor and a DOAS instrument during field campaigns, reported in the literature, revealed deviations in the absolute values within a range of 2 to 70 % (Table 5.2). The discrepancies turned out not to be biased towards one of the techniques. For example, in the study by *Cardenas et al* [00] Hantzsch exceeded DOAS data by a factor of 1.67 at the Weybourne site, whereas *Grossmann et al* [03] present DOAS data exceeding a Hantzsch by a factor of 1.2. In part, these deviations can be ascribed to performing the measurements in ambient air. Due to meteorological effects like turbulence probing the same air mass by the different instruments was not guaranteed. The same argument holds for the measurement techniques. The Hantzsch monitor extracts air samples, whereas the DOAS integrates gas-phase concentrations along the light path.
Under laboratory conditions at SAPHIR, HCHO measurements of the XDOAS exceeded those of the Hantzsch by a factor of 1.25 revealing a scaling problem. In order to track down the reason(s) for this discrepancy from the XDOAS side the basic DOAS equation (2.8) is scrutinised. It contains three parameters, the differential optical density τ', the path length L and the differential optical absorption cross section σ'. The path length in the White cell is known very accurately to within one permil. The light path outside the chamber is ten metres in total. To account for the 25 % enhancement, ambient HCHO levels should have been larger

than the levels in the chamber by a factor of 24 (ie up to 700 ppbv on the 6 Jul 2004 experiment), which is quite unlikely considering a typical tropospheric mixing ratio range of 0.1 to 10 ppbv in rural-suburban areas [Finlayson-Pitts and Pitts 00]. Moreover, if an ambient concentration was significant, it would remain arguable why it should align to the time profile the HCHO followed in the chamber. Looking at τ' an overestimation of the absorption strength is not conceivable, unless it would be an artifact of the spectral evaluation. However, no evidence for that was found. Regarding the potential error of a non-zero HCHO concentration in the reference, the XDOAS result could just differ downward from a correctly working comparison instrument, but would hardly exceed it (cf section 2.1.2). For this reason, on the XDOAS side only a possible inaccurate scaling of the absorption cross section remains. Although the accuracies stated in the literature hardly exceed 5 % for an individual work, the scatter of different publications turns out to be greater than that (cf Appendix C.2). However, the comparison of XDOAS and the calculated concentrations, whereby the latter were derived from simple assumptions, showed good agreement, so that the scaling of the *Meller and Moortgat* [00] cross section is assumed accurate to within the uncertainty boundaries. *Co et al* [05] come to a similar conclusion in their latest paper on the HCHO cross section in the range from 351 to 356 nm. In summary, the discrepancy between Hantzsch and XDOAS cannot be explained by an inaccurate scaling of $\sigma'(\mathrm{HCHO})$.

Aside from the scaling of the absorption cross section another explanation could be found in the instrumental settings. Like the LOPAP the Hantzsch method is an extractive point measurement, in contrast to the path-integrating DOAS method. By surface effects the gas-phase HCHO could have been converted into another compound before being sampled in the inlet line of the Hantzsch. So far, in experiments at SAPHIR no evidence was found that such an inhomogeneity of chamber air masses exists in the dark. Furthermore, possible heterogeneous processes would have adversely affected the linearity between the two instruments.

Derivatisation methods focusing on particular species are often subject to interferences from other substances. Interferences with the Hantzsch method were reported for, among others, glyoxal and acetaldehyde, although they are known to have just a small effect [Dong and Dasgupta 87]. However, during para-formaldehyde thermolysis compounds could have been formed, eg by polymerisation, that negatively interfered with the Hantzsch detection process. In order to investigate this potential cross sensitivity, an additional set of experiments was designed where HCHO was generated chemically in the chamber. These experiments are described in section 5.4.2.

Table 5.2: *Analysis results of HCHO intercomparisons reported in the literature employing DOAS and Hantzsch instruments (Y: DOAS, X: Hantzsch). All references cited were field measurements. In the SAPHIR measurements the error of the fit is too small to be significant.*

REFERENCE	REMARK	SITE	SLOPE [a]	INTERCEPT [ppbv] [a]	N	R^2
This work	Thermolysis	SAPHIR	1.25	0.08(2)	574	0.99
	$C_2H_4 - O_3$	SAPHIR	1.18	0.06(1)	1616	0.99
[Hak et al 05] [b]	Hantzsch 1	Bresso	0.96(8)	0.39(27)	132	0.81
	Hantzsch 2	Bresso	0.92(15)	−0.15(56)	57	0.66
	Hantzsch 3	Bresso	0.90(18)	−0.93(84)	79	0.50
	Hantzsch 4	Bresso	0.93(11)	−0.07(49)	69	0.86
	Hantzsch 5	Bresso	0.98(15)	−0.02(48)	100	0.49
[Grossmann et al 03] [c,d]	–	Pabstthum	1.23(3)	0.56(4)	327	0.66
[Cárdenas et al 00] [c,e]	DOAS 1	Mace Head	0.27	0.21	65	0.09
	DOAS 1	Weybourne	0.84	0.28	52	0.68
	DOAS 2	Weybourne	0.60	−0.01	110	0.77
[Lawson et al 90] [b]	–	Glendora	1.12 [f]	–	–	–

[a] Errors with respect to last digits in parentheses when available
[b] DOAS measurement with multiple reflection cell
[c] DOAS measurement with double pass long path set-up
[d] All data considered
[e] Narrow dynamic concentration range; results for all data
[f] No direct correlation; slope was calculated by dividing the slopes of DOAS and Hantzsch data towards the spectroscopic mean

5.4.2 Chemical Generation of Gaseous Formaldehyde

As described in section 5.4.1 $HCHO$ intercomparisons in summer 2004 revealed a significant discrepancy between the Hantzsch and the XDOAS instruments. In these experiments $HCHO$ had been generated by thermolysing para-formaldehyde powder. In order to test whether the way of $HCHO$ generation had any influence on the instrumental performance, another intercomparison was carried out from 15 to 18 Feb 2005. There, $HCHO$ was generated by the gas-phase chemistry in the reaction of ethene and ozone in the dark. The same three instruments as before (section 5.4.1) were operated during these experiments (XDOAS, LDOAS, Hantzsch).

Experimental

The schedule of the measurements was as follows. On Monday, 14 Feb 2005, a blank measurement with respect to $HCHO$ was carried out. Only ozone, propane and ethane were injected at initial levels of 120 ppbv, 10 ppbv and 10 ppbv, respectively. The dilution of these compounds was monitored for about seven hours to ensure that the instrumentation worked well. The following experiments were conducted in the purged chamber at low absolute humidities of less than 400 mbar. Fan operation in the chamber during injections guaranteed that the volume was well mixed within short time. On Tuesday, 15 Feb 2005, the first ethene-ozone experiment was done. First, ethene and propane were injected at initial mixing ratios of 150 ppbv and 11 ppbv, respectively (purities > 99.95 % each). At 273 K propane has a lifetime of about ten days in the presence of an OH concentration of 10^6 cm^{-3}. Therefore, it would stay chemically inert in this kind of experiment and hence could serve as control parameter of the dilution coefficient. Ethene degradation was initiated by the addition of 120 ppbv O_3 and hence $HCHO$ formation started. In the evening flushing of the chamber was started, which lasted to the next day. On Wednesday, 16 Feb 2005, a $HCHO$ addition by thermolysis of para-formaldehyde similar to the experiments conducted in summer 2004 was repeated. During that experiment the chamber was purged twice shortly to cover a broader dynamic range (cf section 5.4.1). Finally, the chamber was flushed again overnight for the next day. On Thursday, 17 Feb 2005, the experiment of Tuesday was repeated, the only difference being the addition of excess CO (500 ppmv) in order to suppress OH reactions. Ethene was added once during the experiment to enhance $HCHO$ production. The last experiment ran overnight and ended in the morning of Friday, 18 Feb 2005 (Figure 5.12).

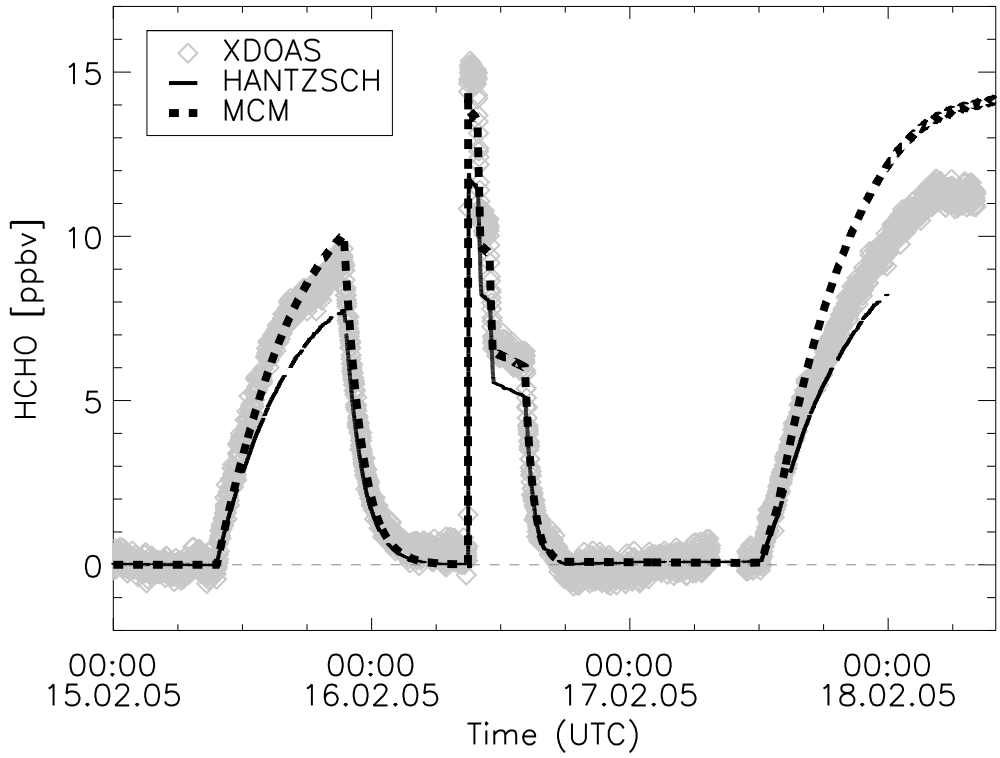

Figure 5.12: *HCHO time profiles in the ethene-ozone experiments performed in Feb 2005. Between the experiments at low (15 Feb) and at high (17 Feb) level CO, on 16 Feb, another thermolysis experiment was performed.*

Model Calculations

Model calculations were performed, which employed the ethene module of the MCMv3. The model initialisation was based on the measured data of O_3 and ethene determined by independent instruments (UV-A, GC). The code of the chemical mechanism is shown in detail in Appendix A.1. Initial values of ethene, ozone and propane were determined by the best fit of the model result to the measured concentration-time profiles (Figure 5.13). Generally, measured profiles show good agreement with the model. Propane data indicate that the dilution coefficient was recorded accurately. Ethene and ozone data confirm that no unaccounted loss process of the two compounds existed. CO injected on 17 Feb 2005 as OH scavenger was not monitored continuously, as the mixing ratio of 500 ppmv exceeded the detection range of the gas chromatograph by several orders of magnitude. Instead, two sample measurements of chamber air were performed using a portable CO monitor (Dräger, Germany), which confirmed an initial mixing ratio of about 500 ppmv. The model was initialised with this value.

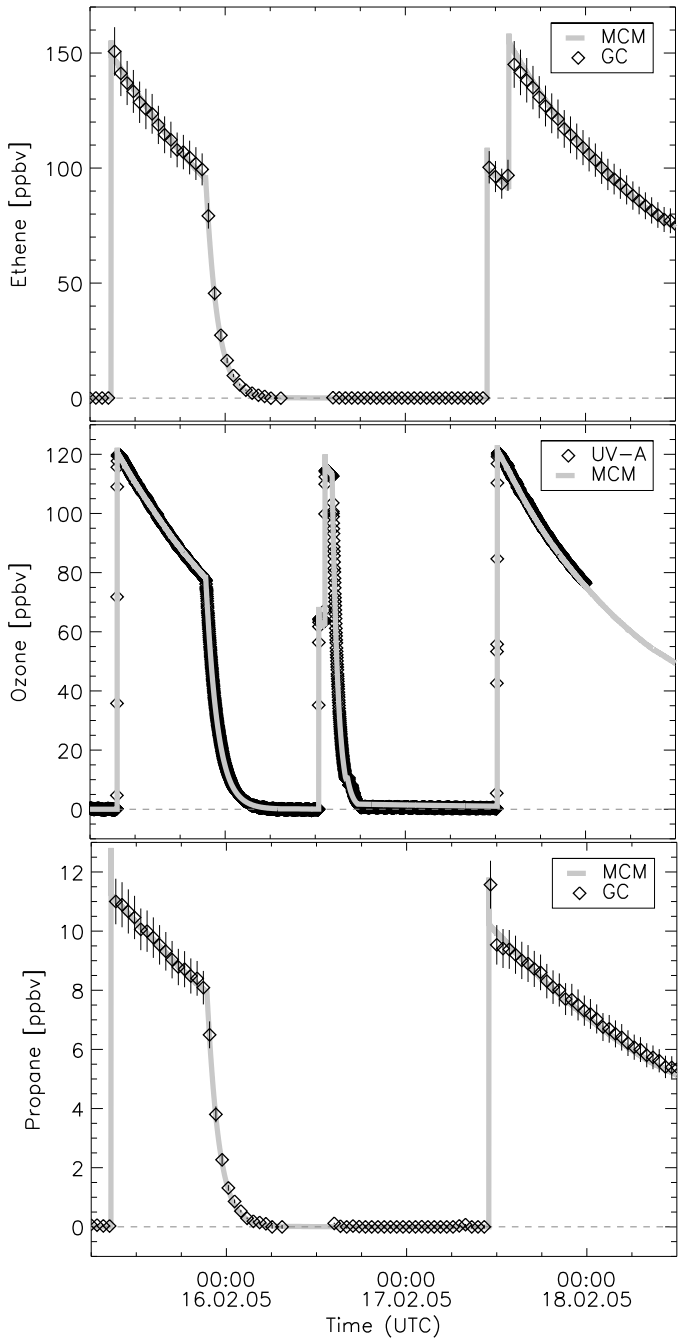

Figure 5.13: *Model data (MCMv3) of the ethene-ozone experiments (lines). Initial values derived from actual measurements (diamonds). Upper panel: ethene. Centre panel: ozone. Ozone was injected on 16 Feb 2005 in a thermolysis experiment in two steps in order to check the Hantzsch monitor for a possible interference. Lower panel: propane.*

XDOAS vs Model

The model data, in steps of 60 seconds, were interpolated linearly to the XDOAS time grid. For correlations and regressions only the data, when no flushing of the chamber was active, were considered. Results of the two experiments are shown in the upper and the centre panel of Figure 5.14. In both figures the correlation curve is slightly bent and deviates significantly from a linear relation indicating the influence of uncertainties in the model, eg in the reaction rate coefficients. However, the regressions yield a correlation parameter of greater than 0.996. The slope in the 15 Feb 2005 experiment at low CO is 0.91. The data show a dip at mixing ratios about 8 ppbv. The reason for this dip remains unclear. It could have been caused by artificial spectral structures from the lamp. In the 17 Feb 2005 experiment at high level CO the slope results in 0.77, which is significantly smaller than in the previous experiment.

XDOAS vs Hantzsch

In the lowest panel of Figure 5.14 the XDOAS is plotted against the Hantzsch data (slope: 1.18$\pm$0.003, intercept: (0.06$\pm$0.01) ppbv, N=1616, R=0.996, χ^2=1250, q=1.000). Again, the correlation coefficient is higher than found in previous intercomparisons of the two techniques. As before results of the Hantzsch instrument underestimate the XDOAS, although the discrepancy between the two is smaller than previously found (1.25 in the thermolysis experiments, section 5.4.1, compared to 1.18 in the ethene-ozone experiments). XDOAS measurements of $HCHO$, introduced into the chamber by thermolysis, were described quantitatively by simple model assumptions. As the $HCHO$ cross section by *Meller and Moortgat* [00] yielded a consistent picture and one of the thermolysis experiments (16 Feb 2005) was conducted between the two ethene-ozone experiments, it appears reasonable to extend the validity of the absorption cross section to the ethene-ozone experiments. A possible explanation of the discrepancies in the thermolysis and ethene-ozone experiments could be that the reproducibility of the Hantzsch calibration is overestimated. Interferences with the Hantzsch instrument due to the presence of reaction intermediates should also be considered. However, the origin or the mechanism of this probable interference remains unclear to date.

Formaldehyde Product Yield

In order to derive absolute $HCHO$ concentrations from data of independent measurements using a chemical mechanism the total product yield of $HCHO$ with respect to chemical ethene consumption was determined. In

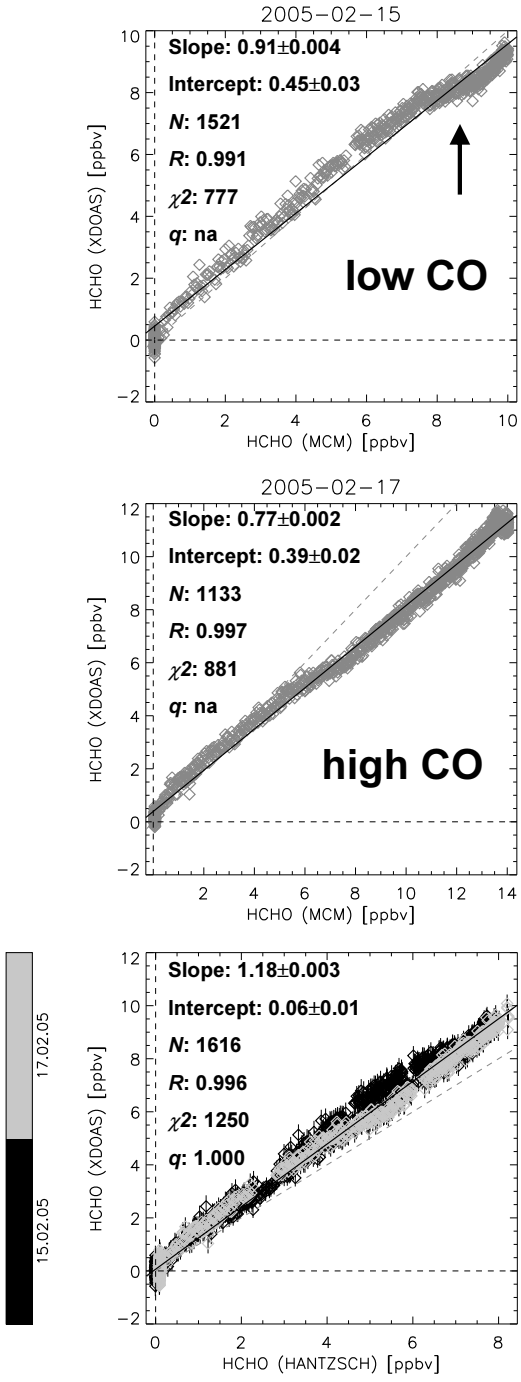

Figure 5.14: *Correlation of XDOAS vs model calculation (MCMv3) for the ethene-ozone experiment without additional CO (upper panel) and at excess CO (centre panel). Arrow: occurrence of an unexpected mixing ratio dip. Lower panel: joint correlation of XDOAS vs Hantzsch for the two days, which are colour coded.*

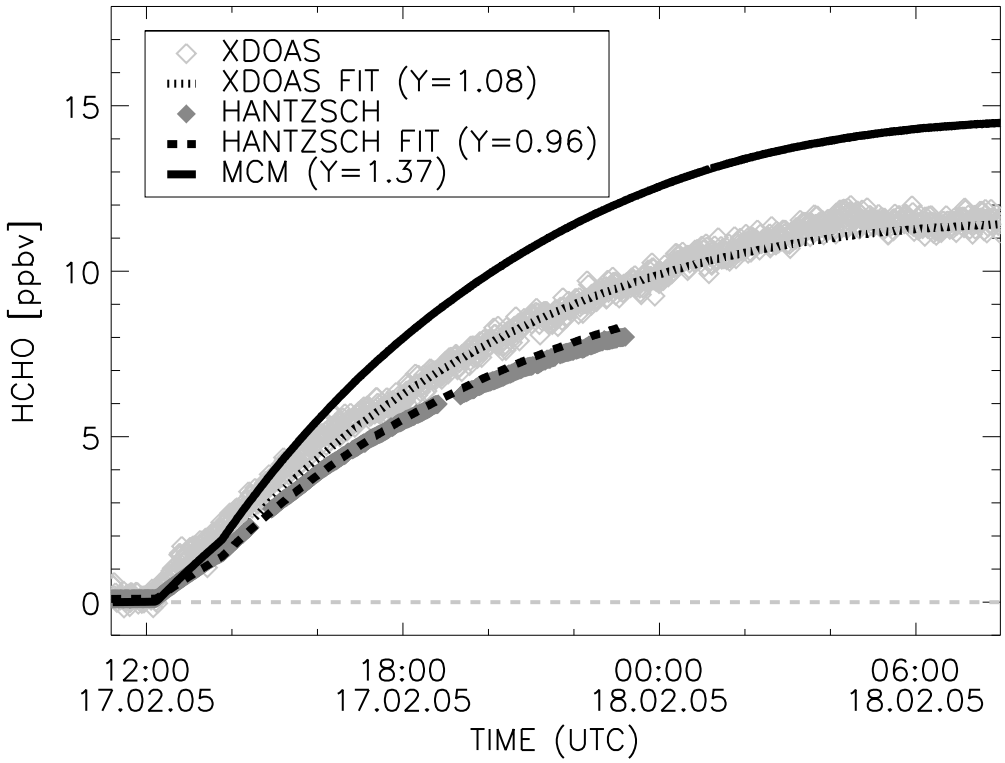

Figure 5.15: *Best fit of modelled to measured HCHO data applying the yield based on ethene consumption as fit parameter, resulting in 1.08±0.19 (XDOAS) and 0.96±0.16 (HANTZSCH) in the experiment at excess CO on 17 Feb 2005. Solid line: yield resulting from the unmodified MCM module.*

the ethene-ozone reaction HCHO is formed as primary product. Experiments suggest a yield of unity [Atkinson 97]. However, other minor secondary production pathways, some of which are speculative to the present day, have been proposed. Total destruction rates of ethene and formaldehyde were corrected for the loss due to dilution. In the experiment at high level CO reaction with O_3 is the single significant ethene sink, whereas in the experiment without added CO, OH radicals, formed by the decay of reaction intermediates, would also degrade ethene and formaldehyde. In the latter case, as OH radicals were not measured, ethene conversion by OH depended completely on the OH production predicted by the model. Rate coefficients of the reaction of ethene and ozone described in the literature and derived from the data in the excess CO experiment agreed within the stated uncertainties. Therefore, ethene consumption was based on the rate coefficient recommended by *IUPAC* [05]. The XDOAS found a product yield of 0.91±0.29 on 15 Feb (at low CO) and 1.08±0.19 on 17 Feb (at high CO). The best fit to the Hantzsch data resulted in 0.77±0.22 on 15 Feb (at low CO) and 0.96±0.16 on 17 Feb (at high CO). Measurement and best fit of HCHO in the high level CO experiment on 17 Feb 2005 are shown in Figure 5.15 for the two instruments. The uncertainty in the experiment at low

CO levels is significantly higher due to the influence of the OH reactions. Generally, uncertainties are so high, that the observed discrepancies between XDOAS and Hantzsch are not significant in both experiments. However, comparing the results to the model reveals agreement within the uncertainty of the HCHO yield measured by the XDOAS in the experiment without added CO (15 Feb). In the experiment at high CO levels (17 Feb) the yield of 1.37, anticipated by the MCMv3, was not found by either of the instruments. The deviation of the experiment at low CO from the experiment at high CO (17 Feb) results from the proposed reaction of CO and stabilised Criegee intermediates, which enhances the HCHO yield in the model of the ethene-ozone reaction considerably (section 2.2.2). The model predicts a yield 37 % above unity under the given conditions. In conclusion, the mechanism of secondary reactions with the respective rate coefficients responsible for secondary HCHO production is not reflected accurately in the model. Particularly, the suggested reactions of stabilised Criegee intermediates with H_2O and CO are still lacking reliable confirmation, and hence introduce uncertainties, which cannot be estimated.
Finally, the idea of deriving the concentration of the product formaldehyde accurately from the reactants ethene and ozone must be discarded. When the accuracy of the rate coefficient of the primary ethene-ozone reaction (factor of 1.26 at 298 K according to *IUPAC* [05] at 95 % confidence limit) is considered, an uncertainty band is created, which encloses the XDOAS as well as the Hantzsch measurements. Therefore, the origin of the discrepancy between XDOAS and Hantzsch cannot be clarified by these experiments. However, the picture created by the XDOAS data appears more consistent with what is known about HCHO chemistry. Finally, the possible negative interference of reaction product intermediates (eg Criegee intermediates) with the Hantzsch detection remains an open question, which should be addressed in future studies.

5.5 Nitrate Radical Experiments

For the generation of NO_3 radicals at the SAPHIR chamber the $NO_2 - O_3$ reaction was used. The ratio of injected NO_x:O_3 allowed to control the produced amount of NO_3.
XDOAS retrieval of NO_3 was performed in the wavelength range from 600 to 690 nm (grating 2, Table 4.1) using the absorption cross section by *Sander* [86]. When necessary H_2O [Rothman et al 05] and a Fraunhofer line reference [Kurucz et al 84] to account for possible atmospheric stray light were included in the evaluation. In the wavelength interval mentioned above NO_3 radicals feature absorption structures that have a natural line width at least comparable to, if not greater than, the instrumental line width [**]. Hence, the cross section was adapted to the instrumental dispersion by an interpolation. From evaluations a limit of detection of NO_3 at 960 m path length of about 20 pptv was derived.

5.5.1 Lifetime in the Purged Chamber

The experiment described in this section was designed to characterise a possible loss process of NO_3 in the purged chamber. At T=298 K and P=1013 hPa NO_3 and its precursor NO_2 are accompanied by N_2O_5 (reaction (2.39)). To date N_2O_5 is not monitored at the SAPHIR chamber making loss processes of N_2O_5 (reaction (2.40)) and a presumed loss process of NO_3 indistinguishable. In order to reduce the effect of the N_2O_5 a chemical system is needed, which features essentially only NO_3. This is achieved by injecting a comparatively small amount of NO_x into an environment of high level O_3, for example at a ratio of 1:5000 (in ppbv). In this case, the NO_2 is converted into NO_3 radicals at a lifetime of about 4 min (at 298 K and 1013 hPa). Initially, an increase in N_2O_5 to a level of 100 pptv is expected. However, due to the short lifetime of 15 s (at 298 K and 1013 hPa) N_2O_5 decomposes rapidly and then stays on a level close to zero for the remainder of the experiment.
In an experiment on 31 Aug 2005 two NO_2 injections of 1 ppbv were performed on a background of 5 ppmv O_3. Consequently, strong production of NO_3 radicals after the NO_2 injections followed (Figure 5.16). Extrapolation of the measured time profile to the time of injection confirmed that the two NO_2 injections amounted to 1 ppbv. After reaching the maximum NO_3 concentrations fell off rapidly.
Reactions (i) to (vii) in Table 5.3 present the inorganic $NO_x - O_x$ mechanism as incorporated in the MCM. Using this system a model was calculated (dashed-dotted line in Figure 5.16, concentrations were multiplied by

[**] 0.4 nm [Sander 86] compared to 0.34 nm FWHM for the XDOAS

Table 5.3: *Inorganic reactions of the MCM in a plain NO_x-O_x system. The modifications reflect proposed but unconfirmed gas-phase reactions in a N_2O_5-NO_3 system. Rate coefficients in cm^3s^{-1} for bimolecular and in cm^6s^{-1} for termolecular reactions.*

NO.	REACTION	RATE COEFFICIENT
	MCM inorganic [a]	
(i)	$N_2O_5 \xrightarrow{M} NO_2 + NO_3$	Troe expression [b,c]
(ii)	$NO + NO + O_2 \longrightarrow NO_2 + NO_2$	$3.3\times10^{-39} \times \exp(530/T) \times [O_2]$
(iii)	$NO + NO_3 \longrightarrow NO_2 + NO_2$	$1.8\times10^{-11} \times \exp(110/T)$
(iv)	$NO + O_3 \longrightarrow NO_2 + O_2$	$1.4\times10^{-12} \times \exp(-1310/T)$
(v)	$NO_2 + NO_3 \xrightarrow{M} N_2O_5$	Troe expression [b,d]
(vi)	$NO_2 + NO_3 \longrightarrow NO + NO_2 + O_2$	$4.5\times10^{-14} \times \exp(-1260/T)$
(vii)	$NO_2 + O_3 \longrightarrow NO_3 + O_2$	$1.4\times10^{-13} \times \exp(-2470/T)$
	Modifications	
(viii)	$NO_3 \xrightarrow{M} NO + O_2$	$2.5\times10^{6} \times \exp(-6100/T)$ [e]
(ix)	$NO_3 + O_3 \longrightarrow NO_2 + 2O_2$	1×10^{-17} [f]
(x)	$N_2O_5 + H_2O \longrightarrow 2HNO_3$	2.5×10^{-22} [g]
(xi)	$N_2O_5 + H_2O \xrightarrow{H_2O} 2HNO_3$	$1.8\times10^{-39} \times [H_2O]$ [g]

[a] [Saunders et al 03]

[b] k=$k_0 \times k_\infty \times (k_0 + k_\infty)^{-1} \times (F_c)^X$, X=$\left[1 + \left(\frac{\log(k_0/k_\infty)}{0.75-1.27\times\log(F_c)}\right)^{-2}\right]^{-1}$

[c] k_0=$1\times10^{-3} \times [N_2] \times (T/300)^{-3.5} \times \exp(-11000/T)$
k_∞=$9.7\times10^{14} \times (T/300)^{0.1} \times \exp(-11080/T)$, F_c=0.35

[d] k_0=$3.6\times10^{-30} \times [N_2] \times (T/300)^{-4.1}$, k_∞=$1.9\times10^{-12} \times (T/300)^{0.2}$, F_c=0.35

[e] [Johnston et al 86]

[f] [Wayne et al 91]

[g] [IUPAC 05]

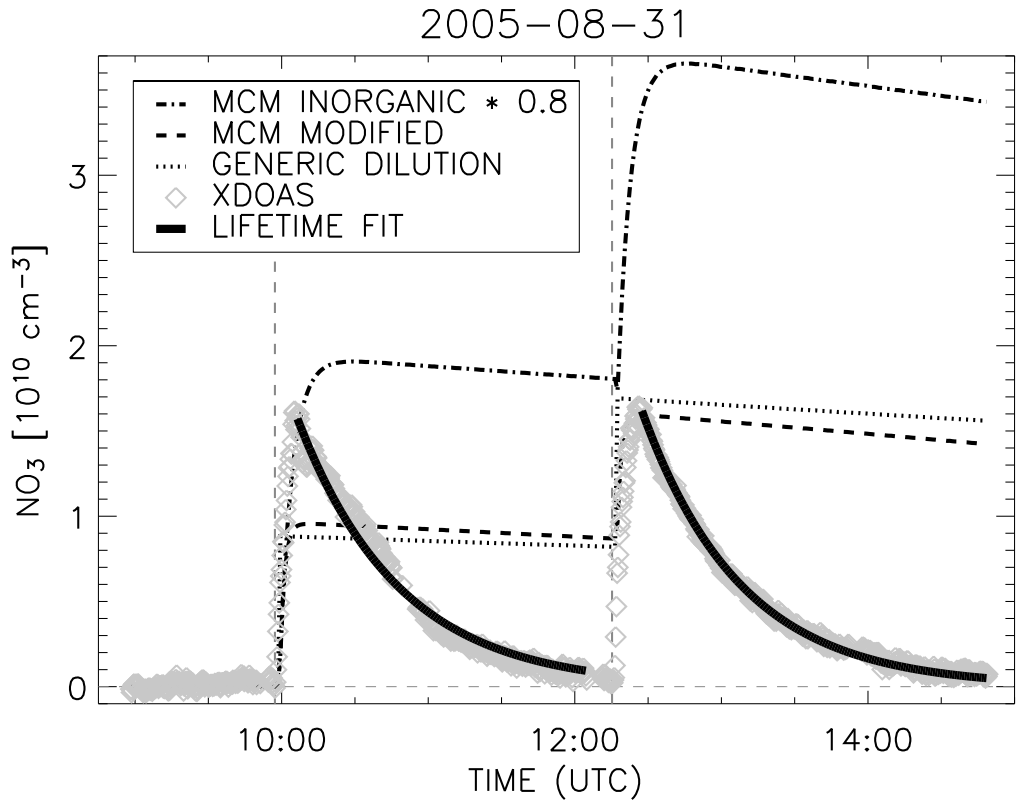

Figure 5.16: *NO_3 time profiles calculated from the plain inorganic MCM mechanism (dashed-dotted line, scaled down by 20 %), calculated from a modified MCM mechanism including reactions (viii) to (xi) from Table 5.3 (dashed line), and measured by the XDOAS (diamonds). Dotted line: effect of the dilution at generic concentrations. Solid line: exponential decay fit to the measured NO_3 data. Vertical lines: NO_2 injections.*

a factor of 0.8) based on measured temperatures, pressures and dilution coefficients, an initial O_3 mixing ratio of 5 ppmv, two NO_2 additions of about 1 ppbv, and a low initial H_2O content of 100 ppmv. Due to the excess O_3 NO levels stay low, and hence NO reactions are not of importance in this system. Once having reached an equilibrium the NO_3 stays quite constant. The slightly negative slope of the time profile is caused by the dilution. However, the resulting NO_3 profile does not reproduce the measured one, so that further assumptions have to be made.
In the last twenty years additional reactions in the gas-phase $NO_3 - N_2O_5$ system were suggested. One of these is the self reaction of NO_3

$$NO_3 + NO_3 \longrightarrow 2NO_2 + O_2 \tag{5.5}$$

with a rate coefficient of 2.3×10^{-16} cm^{3}s^{-1} at 298 K [JPL (02-25) 03]. However, at a maximum possible NO_3 mixing ratio of 1 ppbv it can be neglected. Other reactions to be considered are the thermal decay of NO_3, the reaction of NO_3 and O_3, and two hydrolysis reactions of N_2O_5 ((viii) to (xi) in

Table 5.3). The model calculation described above was repeated adding these four reactions to the plain inorganic MCM system (dashed line in Figure 5.16). Having reached the equilibrium the slope of the NO_3 profile is slightly more negative than would be expected from the dilution (dotted line). This is caused by the hydrolysis reactions (x) and (xi) of N_2O_5 converting the oxidised nitrogen into the reservoir HNO_3. However, these losses are very small. Using reactions (viii) and (ix) in the model the maximum NO_3 level results in about half the level detected by the XDOAS indicating that the significance of these reactions was hitherto overestimated. The thermal decay (decay rate of 3.4×10^{-3} s^{-1} at 298 K [Johnston et al 86]) as well as the ozone reaction (upper rate limit estimated as 1×10^{-17} cm^3s^{-1} [Wayne et al 91]) have been proposed on circumstantial evidence only and are lacking reliable confirmation. Moreover, reactions (viii) and (ix) turn NO_3 back to NO_x and thus dampen the NO_3 radical concentration. But, due to high O_3 levels the produced NO_x is in turn recycled to NO_3 radicals almost immediately.

The fall-off after the maximum concentration can be explained only by a loss process. To characterise the time constant of the fall-off, a first order exponential decay was assumed. NO_3 consumption was calculated considering the dilution and the exponential decay.

$$-\frac{d[NO_3]}{dt} = \left(k_{Dil} + \tau(NO_3)^{-1}\right) \times [NO_3] \tag{5.6}$$

The inverse time constant of the decay term, $\tau(NO_3)^{-1}$, was fit to the measured NO_3 radical data with error weights (solid line in Figure 5.16). As lifetimes 43 and 41 min resulted from the fit of the two fall off curves, respectively, giving in total (42$\pm$4) min. The error was estimated from the accuracies of the dilution (3 %) and the NO_3 measurement (8 %).

Figure 5.17 presents the XDOAS measurement as well as a model result based on reactions (i) to (vii) in Table 5.3 and an additional decay term applying a lifetime of 42 min. The rise in NO_3 as well as its fall-off are well described by the calculation. Including reactions (viii) or (ix) would spoil the agreement. From this, it is estimated that the decay rate of reaction (viii) and the rate coefficient of reaction (ix), given in Table 5.3, are at least lower by a factor of 1 / 21 and 1 / 6, respectively, which renders these reactions irrelevant in this system. Furthermore, the thermal decay lifetime of 6110 s at 298 K derived in this work is longer by a factor of 24 than the average lifetime of 250 s measured by *Heintz et al* [96] on a rural site in the Baltic Sea, which implies that thermal decay of NO_3 plays no significant role in the atmosphere.

The mechanism of the loss process at SAPHIR remains unclear. It could be a heterogeneous loss on surfaces (aerosols, chamber wall). A homogeneous loss would be possible only if a gas-phase reactant of NO_3 was present in the chamber volume, which would convert the oxidised nitrogen into a gas-phase reservoir. Aldehydes, for example, react with NO_3 at rates of about

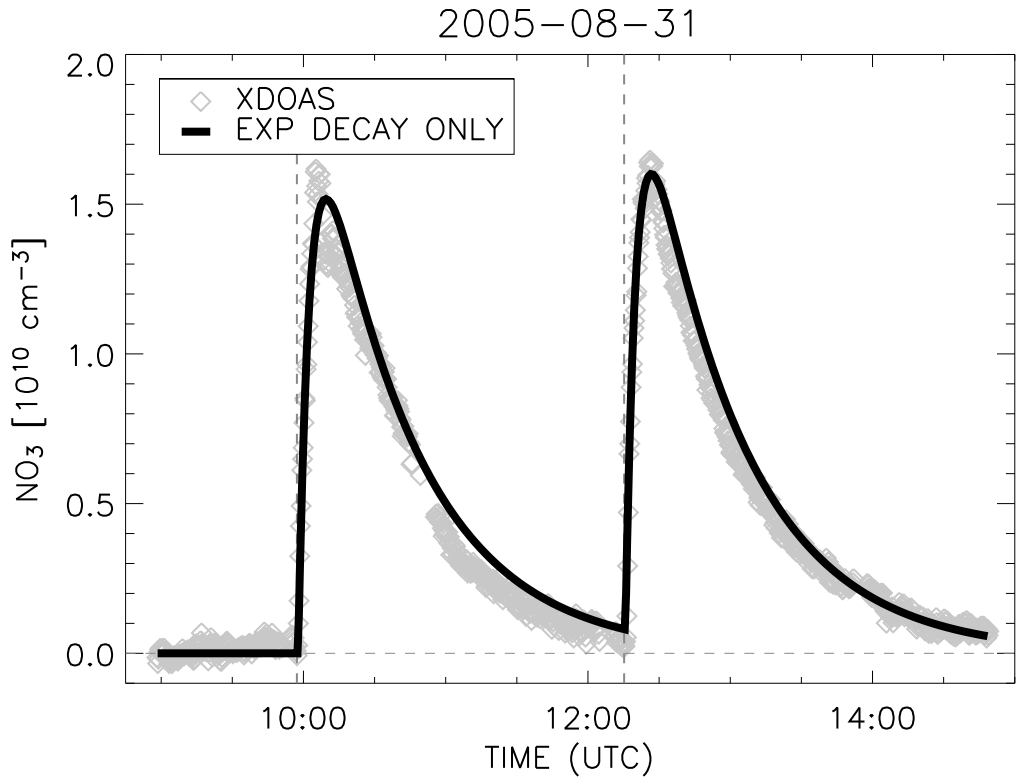

Figure 5.17: *NO_3 time profiles calculated from the plain inorganic MCM mechanism modified only by the derived decay rate of 42 min (solid line), and measured by the XDOAS (diamonds). Vertical lines: NO_2 injections.*

10^{-15} cm^3s^{-1}. To account for the lifetime of 42 min, an aldehyde should be present at levels of at least 16 ppbv. To the present day, no such background reactant for NO_3 could be identified in the purged chamber.

5.5.2 Atmospheric Light Leakage

Nitrate radicals are very sensitive to light at wavelengths below 620 nm (reactions (2.36a) and (2.36b)). The chamber can be darkened with a shutter system during daylight hours. However, it was observed that a fraction of daylight is reaching the interior of the chamber. In the volume the light can interact photochemically with present compounds. This feature was observed when the fan was switched on in a dark NO_3 formation experiment on 12 May 2005 during daylight hours. In this experiment 10 ppbv NO and 160 ppbv O_3 were injected in the otherwise purged chamber. With shutters closed NO_3 concentrations rose steadily until the fan in the chamber was switched on (rectangle in the left panel of Figure 5.18). Then, NO_3 concentrations clearly fell off before being reduced to zero by exposing the chamber to daylight (yellow bar). In general, such an effect could be caused by heterogeneous loss of NO_3 at surfaces (cf section 5.5.1). The loss

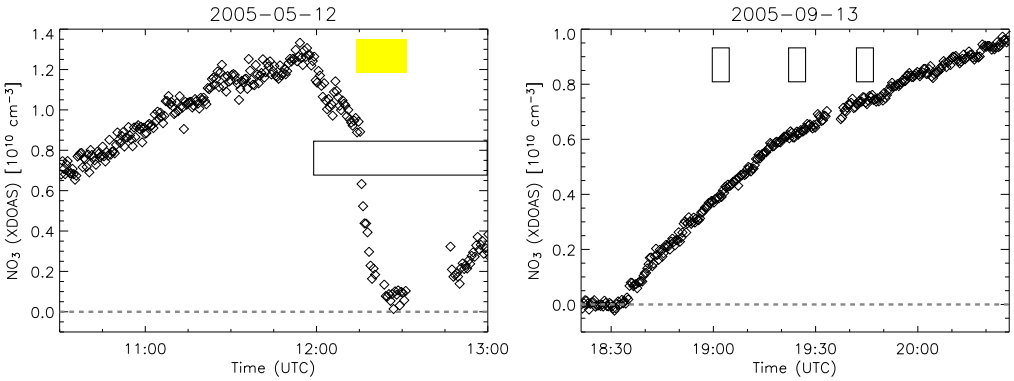

Figure 5.18: *Left panel: NO_3 profile measured by the XDOAS during daytime on 12 May 2005. Yellow bar: period of daylight exposure. Rectangles: periods when fan was operated. At the end of the daylight exposure period NO_3 levels rose again. Right panel: data from 13 Sep 2005 during nighttime. During the night no effect of fan operation on the radical time profile is discernible.*

would affect the boundary layer at the chamber wall extending to some millimetres. In this case, operation of the fan would accelerate the air mass exchange in the boundary layer and hence increase conversion rates. Another hypothesis is that NO_3 radicals are photolysed by the XDOAS light beam. However, if a sink of NO_3 existed in the XDOAS light beam (eg photolysis), operation of a fan would raise the measured NO_3 levels due to the residence time of an air parcel in the light beam. Since this contradicts the observation of a fall-off, NO_3 photolysis by the XDOAS light beam cannot be responsible for the fan effect.

To determine the true nature of the fan effect, an experiment was performed during nighttime, when the influence of daylight could be excluded (right panel of Figure 5.18). Here, 15 ppbv NO_2 and 150 ppbv O_3 were injected in the otherwise purged chamber. Having reached sufficient concentration levels the fan was turned on for intervals of 5 minutes and then off again. The procedure was repeated three times. The operation of the fan had no visible effect on the NO_3 radical concentration. The wall loss can be assumed independent of light conditions, so that the reduced lifetime hypotheses has to be discarded.

To explain the NO_3 loss during fan operation in daylight hours, a dim illumination of small peripheral parts of the current set-up of the chamber by solar stray light is proposed. Nitrate radicals in these peripheral parts are subject to photolysis (reactions (2.36a) and (2.36b)) and hence the effective NO_3 concentration in the chamber is slightly reduced.

Photolysis of NO_3 radicals is not a sink of oxidised nitrogen. Instead NO_3 is converted into NO_x, which is in turn recycled to NO_3 on a time scale depending on the amount of present O_3 (cf section 2.2.3). Since the XDOAS light beam is aligned close to the centre axis of the chamber and the mix-

ing in the dark is relatively slow, a stray light photolysis effect would not be observable unless mixing was forced by operation of the fan.
From the NO_3 fall-off in the time profile from 12 May 2005 during fan operation a fan-initiated lifetime of about 1800 s is estimated. Due to the rapid mixing this value applies to the whole chamber volume of 270 m^3. 1800 s are greater by a factor of 360 than the typical lifetime in the sunlit atmosphere of 5 s (cf section 2.2.3). The fan usually is operated during injection periods of a couple of minutes only. When the fan is turned off, the volume affected by the light leakage must be smaller compared to the total volume by the above factor. To estimate the effect on measurements without fan operation, the lifetime of 1800 s during fan operation applying to the whole chamber volume of 270 m^3 is converted into a shorter lifetime of 5 s applying to the corresponding fraction of the volume 270 m^3 / 360 = 0.75 m^3 when the fan is turned off. The stray light intensity is likely to be lower than full sunlight, so that this estimation must be regarded as a lower limit. However, even if that estimation was wrong by a factor of 4, only 1 % of the chamber volume would be affected by the light leakage, which renders this effect negligible for the experiments performed for this thesis.

5.6 Degradation of Atmospheric Aldehydes by Nitrate Radicals

In the following sections kinetic studies of the reactions of four aldehydes and NO_3, and two product studies of the propanal-NO_3 and butanal-NO_3 reaction are described. As all available measured data were used in the evaluation (NO_2, NO_3, O_3), the considerations about NO_3 behaviour presented in section 5.5 did not have to be accounted for.

5.6.1 Rate Coefficients of NO_3-Aldehyde Reactions

Current recommendations of rate coefficients by *IUPAC* [05] for ethanal (acetaldehyde) and butanal (butyraldehyde) comprise a complete Arrhenius expression and are based on absolute rate studies by *Dlugokencky and Howard* [89] and *Ullerstam et al* [00], respectively. The first was performed at low pressures and the latter employed high, non-atmospheric, reactant concentrations. The recommendation for propanal (propionaldehyde) was derived from several relative rate studies. However, from these data no temperature dependence could be calculated. To the present day, two relative rate studies addressed rate coefficients of the NO_3-benzaldehyde reaction [Atkinson et al 84, Clifford et al 05]. The results by *Atkinson et al* [84] had to be corrected several times until the final specification in *Atkinson* [91], since the coefficient depended on the N_2O_5 production and destruction equilibrium coefficient of reaction (2.39), which underwent numerous changes since that time.
The SAPHIR chamber and the XDOAS instrument allowed absolute rate studies of NO_3 reactions under atmospheric conditions. Aldehydes react with NO_3 and OH radicals, and are photolysed. They do not react with O_3. In a dark environment, in the presence of O_3 and NO_x, secondary reactions in the NO_3 radical initiated conversion of aldehydes constitute the exclusive sources of OH [Platt et al 90]. In the chamber, conditions were generated, under which the NO_3 reaction posed the only chemical loss process. The influence of OH radicals was reduced by a background of excess CO at 250 to 500 ppmv without interfering with other reactions.

Benzaldehyde (Benzenecarbonal)

Benzaldehyde as well as NO_3 were detected concurrently by the XDOAS. On 29 Aug 2005 about 6 ppbv of benzaldehyde (purity $>$ 99.5 %), 10 ppbv of NO_2 and 100 ppbv of O_3 were injected at short intervals into the purged chamber. OH reactions were not expected, since the OH yield from benzaldehyde degradation is too low. Benzaldehyde and NO_3 radicals absorb

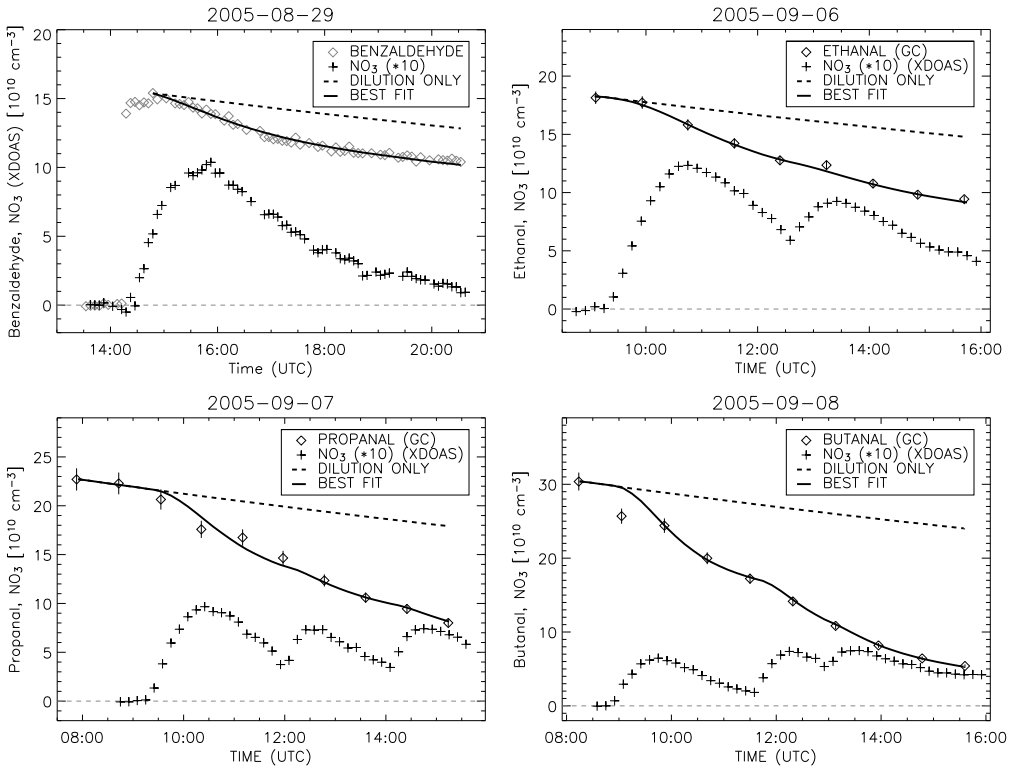

Figure 5.19: *Reactant time profiles of the NO_3-aldehyde experiments. Upper left: benzaldehyde. Upper right: ethanal. Lower left: propanal. Lower right: butanal. Dashed line: evolution of the aldehyde concentration if dilution had been the only sink. Black line: best fit of calculated to measured aldehyde data applying the rate coefficient as variable. The NO_3 data (black crosses) were scaled by a factor of 10.*

in different wavelength regimes. Therefore, the XDOAS measurement algorithm alternated the two required ranges at regular intervals in the measurement period, which lasted about 6 hours.

Aliphatic C_2 to C_4 Aldehydes

On each day from 6 to 8 Sep 2005 an NO_3-aliphatic aldehyde reaction was studied. The experiments were performed after the following pattern. First, the aldehyde ($\approx$ 10 ppbv, Sigma-Aldrich, purities: ethanal $>$ 99.9 %, propanal $>$ 98 %, butanal $>$ 99.5 %) and CO ($\approx$ 250 to 500 ppmv) were injected. A little later O_3 (initially $\approx$ 150 ppbv) was added. The injection of NO_2 ($\approx$ 10 ppbv) initiated production of NO_3. In order to enhance NO_3 radical generation and to obtain higher conversion rates additional NO_2 was injected once or twice during the measurements. The aliphatic aldehydes were monitored by a gas chromatograph at a repetition rate of 1 data point per 50 min.

Modelling the NO_3-Aldehyde Reaction

Concentration-time profiles of the aldehydes after injection were modelled considering only losses due to dilution and to reaction with NO_3 (compare the procedure for the HO_xCOMP campaign, section 5.3.1).

$$-\frac{d[\mathrm{RCHO}]}{dt} = (k_{\mathrm{Dil}} + A \times k_{\mathrm{NO_3}} \times [\mathrm{NO_3}]) \times [\mathrm{RCHO}] \qquad (5.7)$$

(R = CH_3, C_2H_5, C_3H_7, C_6H_5). A is the fitting parameter. $k_{\mathrm{NO_3}}$ reflects the rate coefficient recommended by *IUPAC* [05] including the temperature dependence when available (ethanal, butanal). In the benzaldehyde experiment the model was calculated in 5 min steps. Due to the higher acquisition time of the GC instrument, the time step was extended to 10 minutes for the aliphatic aldehydes. Small gaps in the time profiles of support data (temperature, pressure, etc) were filled by a linear interpolation. The dilution coefficient as well as the measured NO_3 radical concentrations were imposed on the model from the measurements. The model was initialised with a data point, when all of the injected aldehyde had been flushed into the chamber. Uncertainties reported with the fit results were deduced from the accuracies of the measured data sets being 5 % for benzaldehyde (XDOAS), 8 % for the aliphatic aldehydes (GC), 8 % for NO_3 radicals and 3 % for the dilution.

Discussion of the Kinetic Studies

Measured data and model results are shown in Figure 5.19. The rate coefficients (in units of 10^{-15} cm^3s^{-1}) result in: benzaldehyde 2.2$\pm$0.6, ethanal 2.6$\pm$0.5, propanal 5.8$\pm$1.0, and butanal 11.9$\pm$1.4 (Table 5.4). The derived benzaldehyde rate coefficient is based solely on spectroscopic measurements. After model initialisation the benzaldehyde was lost faster than could be expected from a pure dilution effect (dashed line in Figure 5.19). This difference is attributable to the reaction with NO_3. The gradient of benzaldehyde loss is steepest when the NO_3 radical concentration is highest. With the decline of nitrate radicals the benzaldehyde concentration-time profile aligns with the course given by a pure dilution. During the 6 hour experiment the temperature fell from initially 303 to 297 K. Assuming that the temperature dependence of the benzaldehyde rate coefficient, at present not known, resembled that of ethanal described in the works of *Dlugokencky and Howard* [89] the coefficient would have varied by 13 % from minimum to maximum temperature. The relatively high error of the benzaldehyde rate coefficient in this thesis can be ascribed to the comparatively low integrated conversion of benzaldehyde over the experimental period, being comparable to the integrated dilution in this case. The rate coefficient derived here agrees well within the uncertainty limits with the

Table 5.4: *Reaction rate coefficients of NO_3 radicals and four aldehydes (RCHO) determined in absolute rate (AR) and relative rate (RR) studies. Confidence limits of the accuracies: [IUPAC 05] 95 %, all others 68 %.*

R	T [K]	$k(T)$ [a]	REFERENCE	M [b]
C_6H_5	**301±3**	**2.2 ± 0.6**	**This work**	**AR**
	295±2	4.3 ± 0.3	[Clifford et al 05]	RR
	294	2.6 ± 0.1	[Atkinson 91] [c]	RR
CH_3	**300±3**	**2.6 ± 0.5**	**This work**	**AR**
	298±2	3.2 ± 0.8	[Cabañas et al 01]	AR
	298	2.7 ± 0.3	[Dlugokencky and Howard 89]	AR
	298	$2.7\ ^{+\ 1.6}_{-\ 1.0}$	[IUPAC 05]	Review
	298±2	2.6 ± 0.3	[D'Anna et al 01]	RR
	299±1	2.7 ± 0.5	[Cantrell et al 86] [d]	RR
	298±1	2.1 ± 0.5	[Atkinson et al 84] [d]	RR
	300	2.2 ± 0.6	[Morris and Niki 74] [d]	RR
C_2H_5	**300±3**	**5.8 ± 1.0**	**This work**	**AR**
	298±2	6.0 ± 0.6	[Cabañas et al 01]	AR
	298	$6.5\ ^{+\ 3.8}_{-\ 2.4}$	[IUPAC 05]	Review
	298±2	6.2 ± 0.6	[D'Anna et al 01]	RR
	296±2	7.5 ± 0.4	[Papagni et al 00] [d]	RR
	298±2	5.8 ± 0.5	[D'Anna and Nielsen 97]	RR
C_3H_7	**301±2**	**11.9 ± 1.4**	**This work**	**AR**
	298±2	14.6 ± 1.6	[Cabañas et al 01]	AR
	296	11.0 ± 1.0	[Ullerstam et al 00]	AR
	298	$11.0\ ^{+\ 4.6}_{-\ 3.2}$	[IUPAC 05]	Review
	298±2	12.3 ± 1.1	[D'Anna et al 01]	RR
	296±2	11.8 ± 0.6	[Papagni et al 00] [d]	RR
	297±2	10.4 ± 1.1	[Ullerstam et al 00]	RR
	298±2	10.9 ± 1.0	[D'Anna and Nielsen 97]	RR

[a] in units of 10^{-15} cm^3 s^{-1}

[b] Method

[c] Re-evaluated data from *Atkinson et al* [84]

[d] Re-evaluated by *IUPAC* [05]

re-evaluation of the *Atkinson et al* [84] value stated in *Atkinson* [91]. The recently published value by *Clifford et al* [05] exceeds the others by a factor of two (Table 5.4).
In the experiments with aliphatic aldehydes the number of GC data points is small due to the time consuming enrichment and sample processing of 50 min. In this thesis 9 to 10 points acquired within 6 to 8 hours were considered for the fit. The upper right panel of Figure 5.19 shows the fit of model result to measured ethanal data. The propanal data in the lower left panel show a slightly greater scatter, particularly among the first points after NO_3 radical production began. An effect, which disappeared in the last four hours. In the butanal plot model and measurement match almost perfectly except the second data point exhibiting detectable butanal abundance. The enrichment interval of this measurement point coincided with the injection of NO_2, so that an interference due to sampling of inhomogeneous air can be assumed. The result of the calculation of the rate coefficient does not depend on the presence of this outlier, so that it was not excluded.
All in all, the rate coefficients determined in this thesis fit well into the general picture established by other absolute and relative rate studies within the uncertainty limits and therefore confirm current recommendations as made by *IUPAC* [05]. Since most of the other studies were performed under laboratory conditions at high reactant concentrations and low pressures, this study corroborates the validity of the rate coefficients for typical atmospheric conditions.

5.6.2 Product Studies of the NO_3-Degradation of Propanal and Butanal

In the SAPHIR experiments the GC concurrently detected the product ethanal in the propanal experiment and the products propanal and ethanal in the butanal experiment. Under the experimental conditions two degradation processes applied to the aldehydes, viz dilution and the NO_3 reaction (cf reaction (5.7)). To reproduce the experiments numerically, MCM modules (Appendices A.2 and A.3) describing the degradation of propanal and butanal were used to calculate yields of the product aldehydes.
A carbon budget was established by calculating the total conversion figures over the measurement period of 6 to 8 hours. Contributions came from the difference of final to initial value of the GC measurement (observed) and from the integrated degradation turnovers by NO_3 and dilution, which were computed from the measured data using reaction (5.7). Summing up differential concentrations and integrated degradations over the measurement time resulted in the total integrated production of a reaction product. The budgets of the two experiments are shown in Tables 5.5 and 5.7.

NO_3-Propanal

After the injection procedure in the propanal experiment small contaminations of 1.5 ppbv 2-methyl-propane and 1 ppbv 2-propanone were detected by the GC. As these did not affect the NO_3-propanal experiment, they were neglected in the model calculations. 3 of 14 units (1 unit = 10^{10} cm^{-3}) propanal were lost due to dilution (upper segment of Table 5.5). The remaining 11 units reacted with NO_3 radicals. Ethanal concentrations rose by 10 units over the measurement period (left panel of Figure 5.20). At the same time the formed ethanal was diluted (1 unit) and reacted with NO_3 (2 units). Therefore, net production of ethanal is 13 ± 1 units, which must have come from the NO_3-propanal conversion. The ethanal yield accounting for the NO_3 reaction and the dilution in this reaction is (118 ± 22) % and agrees with unity within the uncertainty limits. Production of ethanal, as a molecule containing two carbon atoms, already accounts for about 79 ± 15 % of the chemically converted carbon from propanal, containing three carbon atoms. During degradation a C_1-fragment must have been separated from the propionyl peroxy radical. Reviewing Figure 2.5 separation should have occurred during the conversion from propionyl peroxy to ethyl peroxy radicals on three possible paths (equations (2.29a), (2.29b) and (2.29c), here $R = C_2H_5$) yielding CO_2. Although the CO_2 monitor at SAPHIR is not sensitive enough to detect the increase in CO_2, the carbon budget can be assumed closed with these findings.
A 100 % conversion from precursor to product aldehyde contradicts the results of a model calculation based on the MCMv3 propanal module. The model was run imposing data of the dilution coefficient, temperature, pressure, and the concentrations of O_3, NO_2 and NO_3. Ethanal production in the model underestimates the actual observation significantly (left panel of Figure 5.20). This is a consequence of an integrated peroxypropionyl nitrate (PPN) production of 8×10^{10} cm^{-3}, which accounts for 73 % of the converted carbon in the model and thus results to be the dominant product. However, the sum of the concentration-time profiles of model PPN and model ethanal matches the measured ethanal quite well.

Discussion of the NO_3-Propanal Experiment

The gas chromatograph used for the aliphatic aldehyde detection is discussed first. The sum of modelled ethanal and PPN reproduced well the measured ethanal concentrations. Assuming that the model assumptions are correct, this would be so, if at some point in the GC's analytical process the reservoir PPN had been decomposed into its precursors NO_2 and propionyl peroxy radicals, whereby the latter would then have reacted further to form the product aldehyde ethanal (according to Figure 2.5) before the air sample was analysed on the column.

Table 5.5: *Integrated conversions (in units of 10^{10} cm^{-3}) of the reactant propanal and the observed product ethanal. Excess significant figures have been given to avoid round-off errors.*

REACTANT PROPANAL	
Observed	-14 ± 1.5
Conversion by NO_3 [a]	-11 ± 2.3
Conversion by dilution [a]	-3 ± 0.3
PRODUCT ETHANAL	
Observed	$+10\pm0.9$
Conversion by NO_3 [b]	$(-)2\pm0.4$
Conversion by dilution [b]	$(-)1\pm0.1$
Total production	**13 ± 1**

[a] Calculated from the measured propanal data, cf equation (5.7)
[b] Calculated from the measured ethanal data, cf equation (5.7)

From the chamber an air flow is guided through a 10 m Teflon tubing kept at 55° C before reaching the analysis cell. The residence time of an air parcel in the tubing is 6 s. Since the temperature in the tubing is significantly higher than in the chamber, reservoirs like PPN could have been decomposed during sampling, changing the chemical composition of the air sample on its way. However, model calculations demonstrated that having passed the heated sample line concentrations of PPN were lower by 5 % only. Even if the whole additionally decomposed PPN fraction had been turned into ethanal, it would not be sufficient to explain the observed discrepancy.
At one point during further processing in the GC the enriched sample is heated up to 250° C for desorption. At 250° C the lifetime of PPN is significantly less than a millisecond compared to 40 min at 25° C. However, a conversion of PPN to ethanal at that point in the GC would have degraded the quality of the recorded gas chromatograms visibly, which was not observed. In conclusion from the two points discussed above, the hypothesis of PPN detected as ethanal in the GC due to a thermal artifact is not very probable.
The second part of the discussion covers the atmospheric chemistry model. The MCM describes PPN chemistry with three reactions. One is the formation of PPN via reaction of propionyl peroxy radicals and NO_2 (reaction (2.27)). The second is the thermal decomposition of PPN (back reaction (2.27)) and the third is the reaction with OH radicals (reaction (2.28)) where $R = C_2H_5$. As degradation of PPN by OH radicals is suppressed by CO, thermal decomposition back to NO_2 and the propionyl peroxy radical remains the single degradation path. To date four independent kinetic studies ad-

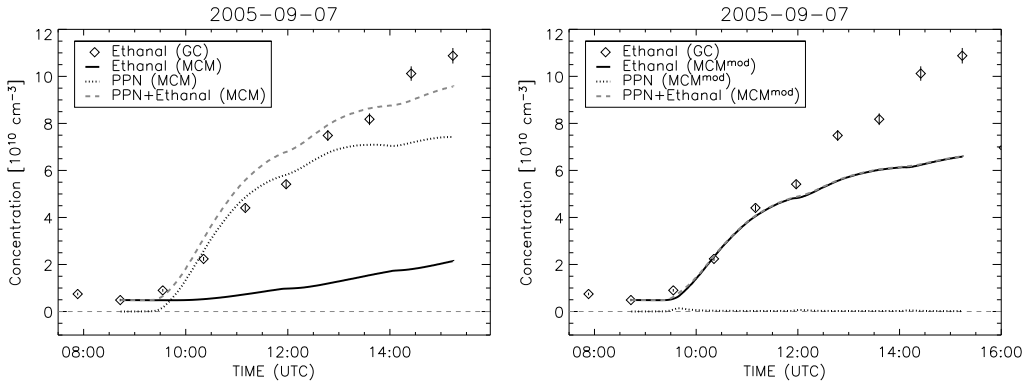

Figure 5.20: *Left panel: time profiles of the product pairs ethanal / PPN in the NO_3-propanal experiment as measured by the GC (diamonds) and as modelled using the MCMv3 (lines). Modelled and detected ethanal differ by a factor of 7. Right panel: results of a modified MCMv3 propanal module where PPN formation is suppressed.*

dressed the thermal decomposition of PPN [Schurath and Wipprecht 79, Mineshos and Glavas 91, Grosjean et al 94a, Kirchner et al 99]. Their decay rates range from 3.4×10^{-4} to 5.1×10^{-4} s^{-1} at 298 K and atmospheric pressure corresponding to a variation of $\pm$20 % around the mean. In conclusion, this reaction is known with reasonable accuracy. The rate coefficient ratio of $k_{(2.27)}$ / $k_{(2.29b)}$ with $R = C_2H_5$ was determined by *Kerr and Stocker* [85], *Becker and Kirchner* [94] and *Seefeld and Kerr* [97], and was in accord with the ratio for $R = CH_3$. Not investigated to date, for reaction (2.29a) ($R = C_2H_5$) the MCM adopted kinetic data from the well-investigated mechanism of the acetyl peroxy radicals under the assumption that reaction kinetics are not altered distinctively by an additional methyl group.

In the model run PPN is identified as the dominant reservoir compound under the experimental conditions. In order to make the experimental findings comply with the model, the latter had to be altered such that either PPN formation was suppressed or PPN decomposition was accelerated. One approach to avoid formation would be to bias the reaction of propionyl peroxy radicals and NO_3 against that with NO_2 by increasing the rate coefficient of reaction (2.29a).

Decomposition and formation of PPN are known quite accurately. However, as peroxypropionyl nitrate is assumed to generally react with OH, it appears reasonable to also propose a reaction with NO_3. A stoichiometrically possible path would be the formation of N_2O_5 and the corresponding precursor propionyl peroxy radical.

$$NO_3 + RCO_3NO_2 \longrightarrow N_2O_5 + RCO_3 \tag{5.8}$$

Table 5.6: *Standard enthalpies of formation (H_f^0) and entropies (S^0) of reactants and products in reaction* (5.8) *for R=CH_3 at 298 K and standard pressure. Errors with respect to the last digits in parentheses when stated in the reference.*

COMPOUND	H_f^0 [kJ mol^{-1}]	REF.	S^0 [kJ mol^{-1} K^{-1}]	REF.
NO_2	34(1)	A	0.24	A
NO_3	74(1)	A	0.258(1)	A
N_2O_5	13(2)	A	0.356(7)	A
CH_3CO_3	−172(20)	B	0.32	C
$CH_3CO_3NO_2$	−258(22)	B	0.384(>8)	D

A: [JPL (02-25) 03]
B: [IUPAC 05]
C: [Tyndall et al 01]
D: Calculated from ΔS^0 = (0.176±0.008) kJ mol^{-1} K^{-1} proposed by *Hendry and Kenley* [77] and *Mhin et al* [00] for the reaction $CH_3CO_3NO_2 \xrightarrow{M} NO_2 + CH_3CO_3$

($R = C_2H_5$). With data only available for PAN and acetyl peroxy radicals the change of the Gibbs free energy [††] in reaction (5.8) for $R = CH_3$ is calculated from the standard enthalpies of formation (H_f^0) and the corresponding entropies (S^0) taken from the literature (Table 5.6) and results in 15 kJ mol^{-1} at 298 K and standard pressure. However, due to the uncertainties of the source data the error of this calculation is estimated to be larger than ±30 kJ mol^{-1}. Although thermochemically not favoured, it cannot be excluded that the proposed reaction with $R = CH_3$ occurs spontaneously under atmospheric conditions. Due to structural similarities the higher homologues of the peroxyacyl nitrates and acyl peroxy radicals are expected to feature similar thermochemical properties. To affect the PPN reservoir the rate coefficient of reaction (5.8) should be of the order of 10^{-11} cm^3 s^{-1}. So far, this reaction has never been proposed nor investigated. To visualise the effect of a model modification, model calculations were repeated

- multiplying the rate coefficient of reaction (2.29a) by a factor of 10 for all present acyl peroxy radical homologues [‡‡] and
- introducing a reaction of the type (5.8) assuming a rate constant of 10^{-11} cm^3 s^{-1} for all present peroxyacyl nitrate homologues.

[††] $\Delta G = \Delta H_f^0 - T\Delta S^0$
[‡‡] Raising the coefficient close to the limit given by the gas-kinetic collision rate

Table 5.7: *Integrated conversions (in units of 10^{10} cm^{-3}) of the reactant butanal and the observed products propanal, ethanal and acetone. Excess significant figures have been given to avoid round-off errors.*

REACTANT BUTANAL			
Observed		-24 ± 2.2	
Conversion by NO_3 [a]		-21 ± 3.4	
Conversion by dilution [a]		-3 ± 0.3	
	PRODUCTS		
	PROPANAL	ETHANAL	ACETONE
Observed	$+6.2\pm0.6$	$+4.8\pm0.4$	$+0.8\pm0.1$
Conversion by NO_3 [b]	$(-)3\pm0.6$	$(-)1.4\pm0.3$	–
Conversion by dilution [b]	$(-)0.8\pm0.1$	$(-)0.8\pm0.1$	$(-)0.2\pm0.02$
Total production	**10 ± 1**	**7 ± 0.5**	**1 ± 0.1**

[a] Calculated from the measured butanal data, cf equation (5.7)
[b] Calculated from the measured product data, cf equation (5.7)

The result of this modified mechanism is shown in the right panel of Figure 5.20. The modifications keep PPN concentrations close to zero. Ethanal formation rises accordingly. However, whereas modified model data and measurement agree quite well in the first three hours of the experiment, the two time profiles diverge considerably towards the end of the experimental period resulting in a difference of approximately 4.5×10^{10} cm^{-3} (about 2 ppbv). The main part of the missing carbon causing this discrepancy is stored in the reservoir C_2H_5OOH (cf vertical degradation path in Figure 2.5) in the modified model. In conclusion, simple modifications of the mechanism intended to suppress the influence of the PPN reservoir do not suffice to bring measurement and model into better agreement. As the propanal module is a part in the NO_3 degradation of butanal, the discussion is resumed in the following section.

NO_3-Butanal

Time profiles of the detected products are displayed in the left panels of Figure 5.21. The precursor aldehyde butanal provides much more reaction pathways as does propanal in the NO_3-degradation process. In contrast to the propanal experiment, the detected products do not suffice to close the carbon budget (lower segment of Table 5.7). In total, 24 units of butanal, the precursor aldehyde, are degraded. 3 units are diluted. 21 units reacted with NO_3 radicals. Integrated production of propanal accounts for 10 units. Since butanal is supposed to be converted the same way as propanal, 10 units of CO_2 should have been generated in the reaction from butyryl

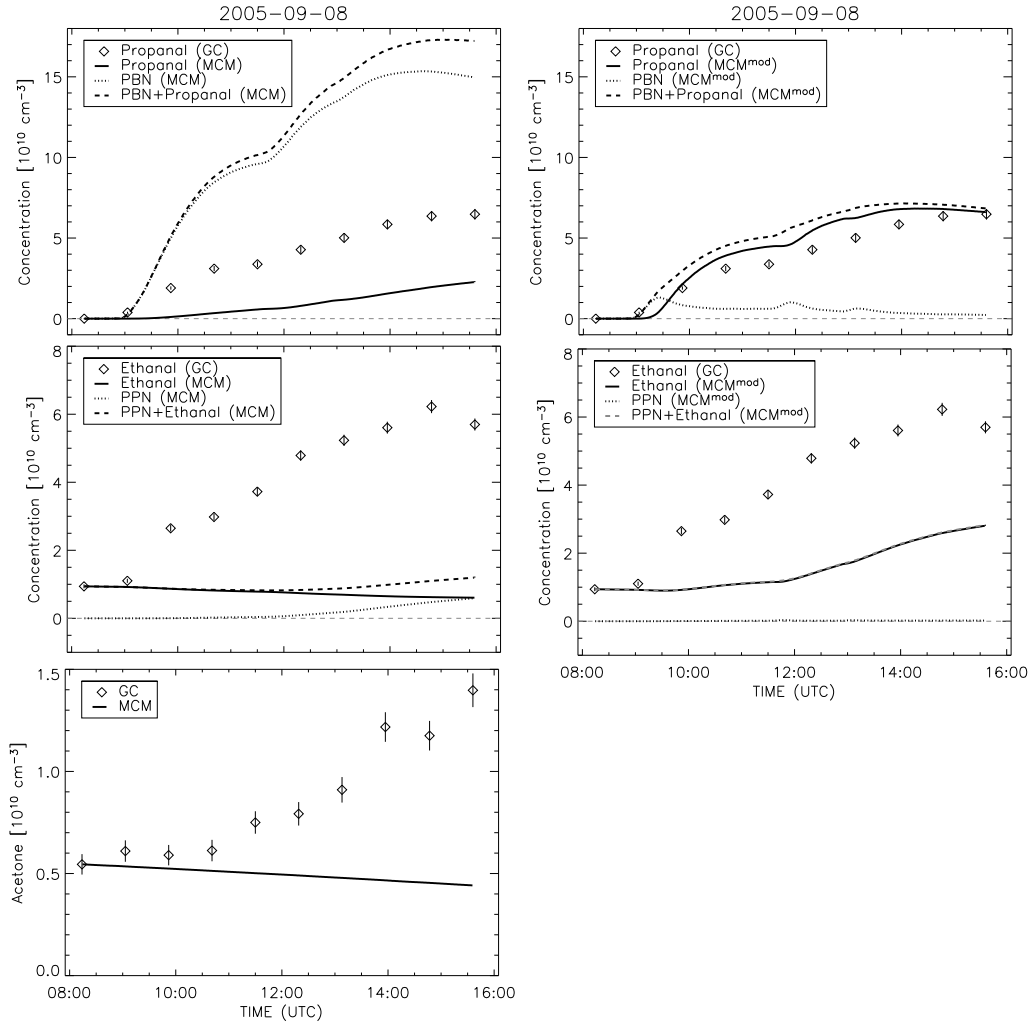

Figure 5.21: *Upper left panel: time profiles of the product pairs propanal / PBN in the NO_3-butanal experiment as measured by the GC (diamonds) and as modelled by the MCMv3 (lines). Measured and calculated propanal differ by a factor of 4. Upper right: propanal results of a modified MCMv3 butanal module. Centre left: product pair ethanal / PPN. Model degradation exceeded model production. Centre right: ethanal results from the modified MCM. Lower left: product acetone. Acetone formation was not predicted by the MCM in this experiment, so that acetone data were not affected by the modifications applied to the model.*

to propyl peroxy radicals. The NO_3 reaction is the only chemical sink of propanal. Translating the results of the propanal experiment, 100 % of this reaction lead to ethanal. Assuming that the rate coefficient is correct, which has been confirmed in the kinetic study, 3 units of the total produced ethanal could have come from the NO_3-propanal reaction, although in total 7 units of ethanal were formed. Hence, about 4 units of ethanal must have been generated via a reaction path, which led from butanal to ethanal more directly.
Unexpectedly, a build up of 0.8 units of acetone was observed. According to the MCM acetone could have been formed only via the precursor aldehyde 2-methyl-propanal whose chemical formula is identical to the one of butanal. However, the purity certified by the producer of the butanal source excludes a sufficient abundance to account for the acetone formation.
Adding up the total integrated productions of propanal, ethanal and acetone yields 18$\pm$1 units, whereas 21$\pm$3.4 units where provided by the NO_3-butanal reaction, which shows reasonable agreement within the uncertainty. However, the integrated conversions of the three observed products cannot simply be summed up, as theoretically one C_4 molecule of butanal could account for a maximum of 2 C_2 molecules of ethanal. Adding up the carbon found within the observed products results in 56$\pm$10 % of the carbon converted in the primary reaction.
Modelling the experiment using the corresponding MCM module revealed similar strong discrepancies as met in the propanal experiment. Peroxyacyl nitrate production, peroxybutyryl nitrate (PBN) in this case, was found to be favoured against the cascading path (upper left panel in Figure 5.21) and yielded 16.4$\times 10^{10}$ cm^{-3} over the measurement period being 78 % of the total converted carbon. Ethanal is not formed significantly in the model calculations.

Discussion of the NO_3-Butanal Experiment

In the NO_3-propanal experiment the sum of modelled ethanal and PPN agreed well with the measured ethanal. The possible accelerated decomposition of PPN in the GC adding to the overall ethanal yield was discussed above. Assuming that such a process existed, it should also apply to the higher homologues of peroxyacyl nitrates in the NO_3-butanal experiment. However, the sum of modelled PBN and propanal did not match the measured propanal in that experiment, but exceeded it by a factor of two. Furthermore, the measured ethanal did not match the sum of modelled PPN and ethanal either. From this, an interference of the GC measurement with the reaction products must be assumed to be unlikely. Nonetheless, studies of interferences with the GC's analytical processing are hard to find. As this kind of gas chromatography is widely used for the detection of atmospheric aldehydes, and peroxyacyl nitrates are usually found in detectable quan-

tities in the atmosphere, possible interferences with this detection method should be studied in more detail in the future.
PBN chemistry studies are less numerous than studies of PPN and PAN. Kinetic parameters of the PBN decay were verified once [Grosjean et al 94b]. The decay rate results in a value comparable to that of PPN and PAN. For the butanal module, the MCM again included kinetic data adopted from the PAN chemistry. As in the NO_3-propanal product study model calculations were repeated applying the same modifications outlined in the previous section (increasing the rate coefficient of reaction (2.29a) by a factor of 10 and adding reaction (5.8)). The results are presented in the right panels of Figure 5.21.
The modifications do not suppress PBN formation completely. This can be attributed to the reaction of butanal and NO_3, which refills butyryl peroxy radicals faster than these are converted into propyl peroxy radicals. In this model run propanal levels align quite well quantitatively with the measured GC values. However, the next lower aldehyde, ethanal, is not correctly described by the modified model. As before in the modified propanal module, PPN formation is prevented, but the rise in ethanal concentration is too slow as to account for the measurement.
In conclusion, by simply increasing the rate coefficient of a secondary reaction and introducing a new reaction path, the MCM could not be modified to bring measurement and model into better agreement. The 100 % yield of ethanal from the NO_3-propanal reaction encountered in the experiment on 7 Sep 2005 was not found in the experiment on 8 Sep 2005 (NO_3-butanal). In the latter the ethanal yield based on propanal consumption is larger by a factor of 2.3, which is mechanistically not possible, indicating that a more direct degradation path from butanal to ethanal in presence of NO_3 exists. Generally, the reaction of NO_3 and propionyl and butyryl peroxy radicals has been rarely studied so far, which introduces a fairly high uncertainty level in model calculations of aldehyde degradation by NO_3. Furthermore, it was suggested that a reaction of peroxyacyl nitrates and NO_3 might occur under atmospheric conditions. Hitherto ignored, this proposed reaction path should be investigated in the future.

Chapter 6

Conclusions

In the course of this thesis the atmosphere simulation chamber SAPHIR was equipped with a multiple reflection system of the White type, which allowed the measurement of trace gases at atmospheric concentrations. High quality measurements were assured performing internal instrument intercomparisons. The XDOAS reproduced, within the uncertainty limits, measurements of a chemiluminescence instrument of NO_2, a long path absorption photometer of $HONO$, an ultraviolet absorption instrument of O_3, two dewpoint hygrometers of H_2O vapour and a gas chromatograph with flame ionisation detector of benzene and m-xylene (Table 6.1).

During the OVOC campaign at SAPHIR in Jan 2005 the XDOAS detected the aromatic compounds benzaldehyde and toluene. Due to the time resolution of about 20 s evidence for a possible memory effect of the injection lines at SAPHIR within the benzaldehyde data was found. This feature was observed in winter, when temperatures were comparatively low.

During the HO_xCOMP campaign at SAPHIR in July 2005 the XDOAS provided measurements of m-xylene and benzene in an experiment designed for the determination of an average OH radical concentration using a simple chemical system. Results obtained in this thesis agreed perfectly with the mean OH concentration concurrently measured by the Laser-DOAS instrument.

$HCHO$ was of interest to a great number of experiments during this thesis. In experiments, where $HCHO$ was formed by thermolysis of paraformaldehyde powder, the Hantzsch monitor exhibited good linearity towards the XDOAS measurement but underestimated it significantly by a factor of 0.8. However, $HCHO$ concentrations in the chamber calculated from simple assumptions turned out to be consistent with the XDOAS data. In three experiments performed over a period of seven months it was demonstrated that the thermolysis preparation procedure yielded reproducible $HCHO$ levels in the gas-phase. In order to exclude interferences

Table 6.1: *Correlation and regression parameters of the internal instrument intercomparisons at SAPHIR for XDOAS vs reference instrument (BENZ: benzene, MXYL: m-xylene).*

SPECIES	REF [a]	SLOPE [b]	INTERCEPT [ppbv] [b]	N χ^2	R [c] q [d]	REL. ACCUR.[e]
NO_2	CL	1.05	0.26	124	1.000	0.12
		±0.002	±0.04	306	0.000	
O_3	UV-A	1.05	−0.56	72	0.988	0.09
[f]		±0.02	±0.71	40	0.999	
O_3		0.89	2.02	2353	0.999	
[g]		±0.001	±0.05	2460	0.053	
H_2O	DPH-1	1.02	5×10^3	880	0.996	≈ 0.04 [h]
		±0.002	$\pm 5 \times 10^3$	2720	0.000	
	DPH-2	1.03	-22×10^3	492	0.996	
		±0.003	$\pm 6 \times 10^3$	1460	– [i]	
HONO	LOPAP	0.94	−0.05	354	0.918	0.12
		±0.03	±0.01	182	1.000	
BENZ	GC	0.96	0.07	7	0.998	0.11
		±0.19	±0.74	1	0.985	
MXYL	GC	1.13	0.12	7	0.984	0.09
		±0.05	±0.09	12	0.030	
HCHO	Hantzsch	1.25	0.08	574	0.996	0.11
[j]		±0.004	±0.02	492	0.993	
HCHO		1.18	0.06	1616	0.996	
[k]		±0.003	±0.01	1250	1.000	

[a] Reference instrument
[b] ±Error of the fit
[c] Pearson linear correlation coefficient
[d] Quality of fit parameter
[e] Combining the accuracies of the individual instruments
[f] Ozone intercomparison only, 11 Aug 2004
[g] Ethene-Ozone experiments, see section 5.1.2
[h] Accuracy of a DPH; personal communication from Franz Rohrer
[i] Errors of DPH-2 not available
[j] Thermolysis experiments, see section 5.4.1
[k] Ethene-Ozone experiments, see section 5.4.2

of the preparation procedure with the Hantzsch monitor, in ethene-ozone experiments $HCHO$ was generated chemically. There, the Hantzsch underestimated the XDOAS significantly by a factor of 0.85, which is not in accord with the first observed discrepancy. Model calculations based on the ethene module of the MCMv3 being calibrated on measured reactant data of ethene (GC) and ozone (UV-A) agreed with the XDOAS in an experiment at low CO levels. In an experiment performed at high CO levels, to scavenge OH radicals, the $HCHO$ yield in the model overestimated the yield derived from measured data of both instruments distinctively. The discrepancy originates from a proposed reaction of Criegee intermediates and CO in the MCM, which at least must be assumed incorrect in the magnitude of the reaction rate coefficient. From all considerations, the correct scaling of the differential absorption cross section by *Meller and Moortgat* [00], crucial to the DOAS retrieval of $HCHO$, was confirmed.

NO_3 radical studies provided insights into characteristics of the SAPHIR chamber. A loss process of NO_3 radicals in the purged and dry chamber was identified and characterised with a lifetime of 42 minutes. The explicit mechanism of this loss remains unclear to the present day. These measurements and additional model studies revealed that a possible thermal decay of NO_3 as well as a NO_3-O_3 reaction could occur only at rates lower than previously assumed, leaving these processes unimportant in the atmosphere. Furthermore, due to their photolytical sensitivity evidence was found in NO_3 measurements that a small fraction of daylight enters the chamber volume, even when the shutters are closed. This finding should initiate the mechanical improvement of the shutter system. It was estimated, however, that only a small fraction of 1 % of the chamber volume was affected by this daylight leakage, which renders it to be a negligible effect.

Absolute rate studies of NO_3-aldehyde reactions were performed for ethanal, propanal, butanal and benzaldehyde. The rate coefficient of the NO_3-benzaldehyde reaction was determined on an absolute basis for the first time. Furthermore, the experiments at SAPHIR presented here were the only laboratory studies conducted under near-atmospheric conditions, and reproduced well the current recommendations in the scientific community [IUPAC 05]. Studies of product aldehydes in the propanal-NO_3 and butanal-NO_3 experiments revealed that the measured yields were much larger than anticipated by model calculations based on the MCMv3. A GC artifact in the measured data of the product aldehydes caused by enforced thermal decomposition of peroxyacyl nitrates is assumed to be unlikely. An analysis of thermochemical data from the literature revealed that a, so far unconsidered, reaction of NO_3 and peroxyacyl nitrates might occur under atmospheric conditions possibly forming N_2O_5 and the corresponding acyl peroxy radicals. The ethanal yield based on propanal consumption in the NO_3-butanal experiment resulted in 2.3 being significantly larger than

unity, although the MCM mechanism expects ethanal formation only by the NO_3-propanal reaction. In conclusion, a more direct degradation path from butanal to ethanal initiated by NO_3 is proposed, although the exact mechanism of this path could not be devised from the measurements at SAPHIR. In general, NO_3 reactions within the degradation mechanisms of higher aldehydes have been barely studied to the present day leaving chemistry models with a considerable uncertainty. Future investigations should repeat experiments described in this thesis. Additional instruments like a peroxyacyl nitrate monitor or a sensitive CO_2 sensor could indicate what the reasons for the deviations are.

Chapter 7

Acknowledgements

- Prof Dr Ulrich Platt for accepting the scientific supervision of this thesis
- Prof Dr Andreas Wahner for making possible the performance of this thesis at the ICG-II
- Dr Theo Brauers for his guidance and support at the ICG-II as executive supervisor
- Dr Hans-Peter Dorn for his readiness to share his experience with youngsters
- Dr Eric Schlosser for several enlightening communications, his experimental dedication during DOAS experiments, and proofreading parts of the manuscript
- Rolf Häseler for being the first address when anything at the chamber had to be done
- Franz-Josef Johnen for his contributions to the experimental XDOAS set-up
- Dr Franz Rohrer for his help in modelling matters and the provision of support data
- Cornelia Richter for providing very helpful modelling tools
- Dr Birger Bohn for fruitful discussions
- Dr Robert Wegener for contributing several support data to this thesis
- Ralf Tillmann for his dedication during the formaldehyde experiments

- Prof Dr Dirk Poppe, Dr Frank Holland, Dr Lutz Rupp, Dr Manfred Siese, Dr Matthias Karl and Hendrik Fuchs for interesting discussions during lunchtime walks
- Fellows from the ICG mechanics and electronics workshop without whom the XDOAS set-up would not have been possible
- Claudia Hak, André Merten, Dr Sebastian Trick from the University of Heidelberg, at least at the time when I started to work on this thesis
- My parents for supporting me in all decisions I made

Bibliography

[Atkinson et al 84] Atkinson, R, WPL Carter, CN Plum, AM Winer, and JN Pitts Jr (1984): Kinetics of the Gas-Phase Reactions of NO_3 Radicals with a Series of Aromatics at 296 $\pm$ 2 K. *Inter. J. Chem. Kinet.*, *16*, 887-898

[Atkinson 86] Atkinson, R (1986): Kinetics and Mechanisms of the Gas-Phase Reactions of the Hydroxyl Radical with Organic Compounds under Atmospheric Conditions. *Chem. Rev.*, *85*, 69-201

[Atkinson and Aschmann 89] Atkinson, R, and SM Aschmann (1989): Rate Constants for the Gas-Phase Reactions of the OH Radical with a Series of Aromatic-Hydrocarbons at 296 $\pm$ 2 K. *Inter. J. Chem. Kinet.*, *21*, *5*, 355-365

[Atkinson 91] Atkinson, R (1991): Kinetics and Mechanisms of the Gas-Phase Reactions of the NO_3 Radical with Organic Compounds. *J. Phys. Chem. Ref. Data*, *20*, *3*, 461-507

[Atkinson 97] Atkinson, R (1997): Gas-Phase Tropospheric Chemistry of Volatile Organic Compounds: 1. Alkanes and Alkenes. *J. Phys. Chem. Ref. Data*, *26*, *2*, 215-290

[Bass et al 80] Bass, AM, LC Glasgow, C Miller, JP Jesson, and DL Filkin (1980): Temperature dependent absorption cross sections for formaldehyde (CH_2O): The effect of formaldehyde on stratospheric chlorine chemistry. *Planet. Space Sci.*, *28*, 675-679

[Becker and Kirchner 94] Becker, KH, and F Kirchner (1994): *Kinetische Untersuchungen an Peroxynitraten und Peroxy-Radikalen.* Bericht, Bergische Universität, Gesamthochschule Wuppertal, Fachbereich 9, Physikalische Chemie, 29

[Bloss et al 05] Bloss, C, V Wagner, A Bonzanini, ME Jenkin, K Wirtz, M Martin-Reviejo, and MJ Pilling (2005): Evaluation of detailed aromatic mechanisms (MCMv3 and MCMv3.1) against environmental chamber data. *Atmos. Chem. Phys.*, *5*, 623-639

[Bobrowski et al 03] Bobrowski, N, G Hönninger, B Galle, and U Platt (2003): Detection of bromine monoxide in a volcanic plume. *Nature*, *423*, 273-276

[Bogumil et al 03] Bogumil, K, J Orphal, T Homann, S Voigt, P Spietz, OC Fleischmann, A Vogel, M Hartmann, H Bovensmann, J Frerick, and JP Burrows (2003): Measurements of molecular absorption spectra with the SCIAMACHY pre-flight model: Instrument characterization and reference data for atmospheric remote sensing in the 230-2380 nm region. *J. Photochem. Photobiol. A*, *157*, 167-184

[Bohn and Zilken 05] Bohn, B, and H Zilken (2005): Model-aided radiometric determination of photolysis frequencies in a sunlit atmosphere simulation chamber. *Atmos. Chem. Phys.*, *5*, 191-206

[Brauers et al 95] Brauers, T, M Hausmann, U Brandenburger, and H-P Dorn (1995): Improvement of differential optical absorption spectroscopy with a multichannel scanning technique. *Appl. Optics*, *34*, *21*, 4472-4479

[Brauers and Rohrer 99] Brauers, T, and F Rohrer (1999): *Easy Atmo-Spheric chemistrY (Ver. 2).* Forschungszentrum Jülich, FZJ-ICG3-BHB-1234, Version 2.9

[Cabañas et al 01] Cabañas, B, P Martín, S Salgado, B Ballesteros, and E Martínez (2001): An Experimental Study on the Temperature Dependence for the Gas-Phase Reactions of NO_3 Radicals with a Series of Aliphatic Aldehydes. *J. Atmos. Chem.*, *40*, 23-39

[Cantrell et al 86] Cantrell, CA, JA Davidson, KL Busarow, and JG Calvert (1986): The $CH_3CHO - NO_3$ Reaction and Possible Nighttime PAN Generation. *J. Geophys. Res.*, *91 (D5)*, 5347-5353

[Cantrell et al 90] Cantrell, CA, JA Davidson, AH McDaniel, RE Shetter, and JG Calvert (1990): Temperature-Dependent Formaldehyde Cross Sections in the Near-Ultraviolet Spectral Region. *J. Phys. Chem.*, *94*, 3902-3908

[Cárdenas et al 00] Cárdenas, LM, DJ Brassington, BJ Allan, H Coe, B Alicke, U Platt, KM Wilson, JMC Plane, and SA Penkett (2000): Intercomparison of Formaldehyde Measurements in Clean and Polluted Atmospheres. *J. Atmos. Chem.*, *37*, 53-80

[Carlier et al 86] Carlier, P, H Hannachi, and G Mouvier (1986): The Chemistry of Carbonyl Compounds in the Atmosphere - A Review. *Atmos. Env.*, *20*, *11*, 2079-2099

[Clifford et al 05] Clifford, GM, LP Thüner, JC Wenger, and DE Shallcross (2005): Kinetics of the gas-phase reactions of OH and NO_3 radicals with aromatic aldehydes. *J. Photochem. Photobio. A*, *176*, *1-3*, 172-182

[Co et al 05] Co, DT, TF Hanisco, JG Anderson, FN Keutsch (2005): Rotationally Resolved Absorption Cross Sections of Formaldehyde in the 28100-28500 cm^{-1} (351-356 nm) Spectral Region: Implications for in Situ LIF Measurements. *J. Phys. Chem. A*, *109*, 10675-10682

[Czerny and Turner 30] Czerny, M, and AF Turner (1930): Über den Astigmatismus bei Spiegelspektrometern. *Z. f. Physik*, *61*, 792-797

[D'Anna and Nielsen 97] D'Anna, B, and CJ Nielsen (1997): Kinetic study of the vapour-phase reaction between aliphatic aldehydes and the nitrate radical. *J. Chem. Soc.*, *Faraday Trans.*, *93*, *19*, 3479-3483

[D'Anna et al 01] D'Anna, B, Ø Andresen, Z Gefen, and CJ Nielsen (2001): Kinetic study of OH and NO_3 radical reactions with 14 aliphatic aldehydes. *Phys. Chem. Chem. Phys.*, *3*, 3057-3063

[Dlugokencky and Howard 89] Dlugokencky, EJ, and CJ Howard (1989): Studies of NO_3 Radical Reactions with Some Atmospheric Organic Compounds at Low Pressures. *J. Phys. Chem.*, *93*, 1091-0196

[Dong and Dasgupta 87] Dong, S, and PK Dasgupta (1987): Fast Fluorometric Flow Injection Analysis of Formaldehyde in Atmospheric Water. *Env. Sci. Tech.*, *21*, 581-588

[Etzkorn et al 99] Etzkorn, T, B Klotz, S Sørensen, IV Patroescu, I Barnes, KH Becker, and U Platt (1999): Gas-phase absorption cross sections of 24 monocyclic aromatic hydrocarbons in the UV and IR spectral ranges. *Atmos. Env.*, *33*, 525-540

[Fayt and Roozendael 01] Fayt, C, and M van Roozendael (2001): *WinDoas 2.1 - Software User Manual.* Brussels: BIRA-IASB

[Finlayson-Pitts and Pitts 00] Finlayson-Pitts, BJ, and JN Pitts (2000): *Chemistry of the Upper and Lower Atmosphere. Theory, Experiments and Applications.* Academic Press, San Diego

[Geyer 00] Geyer, A (2000): *The Role of the Nitrate Radical in the Boundary Layer - Observations and Modeling Studies.* PhD thesis, Institut für Umweltphysik, University of Heidelberg

[Gomer et al 93] Gomer, T, T Brauers, F Heintz, J Stutz, and U Platt (1993): *MFC User Manual V 1.98.* Institut für Umweltphysik, University of Heidelberg

[Grassi and Guzzi 01] Grassi, L, and R Guzzi (2001): Theoretical and practical consideration of the constrution of a zero-geometric-loss multiple-pass cell based on the use of monolithic multiple-face retroreflectors. *Appl. Optics*, *40*, *33*, 6062-6071

[Grosjean et al 94a] Grosjean, D, E Grosjean, and EL Williams II (1994): Thermal Decomposition of PAN, PPN and Vinyl-PAN. *J. Air & Waste Manage. Assoc.*, *44*, 391-396

[Grosjean et al 94b] Grosjean, D, EL Williams II, and E Grosjean (1994): Communication: Gas-Phase Thermal Decomposition of Peroxy-N-Butyryl Nitrate. *Int. J. Chem. Kinet.*, *26*, 381-387

[Grossmann et al 03] Grossmann, D, GK Moortgat, M Kibler, S Schlomski, K Bächmann, B Alicke, A Geyer, U Platt, MU Hammer, B Vogel (2003): Hydrogen peroxide, organic peroxides, carbonyl compounds, and organic acids measured at Pabsthum during BERLIOZ. *J. Geophys. Res.*, *108*, *D4*, 8250, doi:10.1029/2001JD001096

[Gutbrod et al 97] Gutbrod, R, S Meyer, MM Rahman, RN Schindler (2003): On the use of CO as Scavenger for OH Radicals in the Ozonolysis of Simple Alkenes and Isoprene. *Int. J. Chem. Kinet.*, *29*, *9*, 717-723

[Hak et al 05] Hak, C, I Pundt, S Trick, C Kern, U Platt, J Dommen, C Ordóñez, ASH Prévôt, W Junkermann, C Astorga-Lloréns, BR Larsen, J Mellqvist, A Strandberg, Y Yu, B Galle, J Kleffmann, JC Lörzer, GO Braathen, and R Volkamer (2005): Intercomparison of four different in-situ techniques for ambient formaldehyde measurements in urban air. *Atmos. Chem. Phys.*, *5*, 2881-2900

[Hausmann et al 97] Hausmann, M, U Brandenburger, T Brauers, and H-P Dorn (1997): Detection of tropospheric OH radicals by long-path differential-optical-absorption spectroscopy: Experimental setup, accuracy, and precision. *J. Geophys. Res.*, *102*, 16011-16022

[Hausmann et al 99] Hausmann, M, U Brandenburger, T Brauers, and H-P Dorn (1999): Simple Monte Carlo methods to estimate the spectra evaluation error in differential-optical-absorption spectroscopy. *Appl. Optics*, *38*, *3*, 462-475

[Heintz et al 96] Heintz, F, U Platt, H Flentje, and R Dubois (1996): Long-term observation of nitrate radicals at the Tor station, Kap Arkona (Rügen). *J. Geophys. Res.*, *101*, *D17*, 22891-22910

[Heland et al 01] Heland, J, J Kleffmann, R Kurtenbach, and P Wiesen (2001): A New Instrument to Measure Gaseous Nitrous Acid (HONO) in the Atmosphere. *Env. Sci. Tech.*, *35*, 3207-3212

[Hendry and Kenley 77] Hendry, DG, RA Kenley (1977): Generation of Peroxy Radicals from Peroxy Nitrates (RO_2NO_2). Decomposition of Peroxyacyl Nitrates. *J. Am. Chem. Soc.*, *99*, *9*, 3198-3199

[IUPAC 05] IUPAC Subcommittee on Gas Kinetic Data Evaluation for Atmospheric Chemistry (2005): *Summary of Evaluated Kinetic and Photochemical Data for Atmospheric Chemistry.* Web version, available at http://www.iupac-kinetic.ch.cam.ac.uk/, March 2005

[Jenkin et al 97] Jenkin, ME, SM Saunders and MJ Pilling (1997): The tropospheric degradation of volatile organic compounds: a protocol for mechanism development. *Atmos. Env.*, *31*, *1*, 81-104

[Jenkin et al 03] Jenkin, ME, SM Saunders, V Wagner, and MJ Pilling (2003): Protocol for the development of the Master Chemical Mechanism, MCMv3 (Part B): troposheric degradation of aromatic volatile organic compounds. *Atmos. Chem. Phys.*, *3*, 181-193

[Johnston et al 86] Johnston, HS, CA Cantrell, JG Calvert (1986): Unimolecular Decomposition of NO_3 to Form NO and O_2 and a Review of N_2O_5/NO_3 Kinetics . *J. Geophys. Res.*, *91*, 5159-5172

[JPL (02-25) 03] NASA Panel for Data Evaluation (2003): *Chemical Kinetics and Photochemical Data for Use in Atmospheric Studies, Evaluation Number 14.* Web version, available at http://jpldataeval.jpl.nasa.gov/, February 2003

[Karl 04] Karl, M (2004): *Modellierung atmosphärisch-chemischer Reaktionen in der Tageslicht-Atmosphären-Simulationskammer SAPHIR.* PhD thesis, Westfälische Wilhelms-Universität Münster

[Kerr and Stocker 85] Kerr, JA, and DW Stocker (1985): The Kinetics and Mechanism of the Photo-Oxidation of Propionaldehyde under Simulated Atmospheric Conditions. *J. Photochem.*, *28*, 475-489

[Kirchner et al 99] Kirchner, F, A Mayer-Figge, F Zabel, KH Becker (1999): Thermal Stability of Peroxynitrates. *Int. J. Chem. Kinet.*, *31*, *2*, 127-144

[Kraus and Geyer 01] Kraus, S, and A Geyer (2001): *DOASIS Jscript programming description.* Institut für Umweltphysik, University of Heidelberg

[Krinke 99] Krinke, SMW (1999): *Experimentelle Bestimmung der Depositionsgeschwindigkeit von Formaldehyd und Ozon über einem Laubwaldbestand.* PhD thesis, School of Chemistry, University of Stuttgart

[Kurucz et al 84] Kurucz, R L, I Furenlid, J Brault, and L Testerman (1984): *Solar flux atlas from 296 to 1300 nm.* Technical report, National Solar Observatory

[Lawson et al 90] Lawson, K, HW Biermann, EC Tuazon, AM Winer, GI Mackay, HI Schiff, GL Kok, PK Dasgupta, K Fung (1990): Formaldehyde Measurement Method Evaluation and Ambient Concentrations During the Carbonaceous Species Methods Comparison Study. *Aerosol Sci. Tech.*, *12*, 64-76

[Levenberg 44] Levenberg, K (1944): A method for the solution of certain non-linear problems in least squares. *Quart. Appl. Math.*, *2*, 164-168

[Marquardt 63] Marquardt, DW (1963): An algorithm for least-squares estimation of non-linear parameters. *J. Soc. Indust. Appl. Math.*, *11*, 431-441

[McNaught and Wilkinson 97] McNaught, AD, and A Wilkinson (1997): *Compendium of Chemical Terminology, 2nd edition.* Blackwell Science, ISBN 0865426848

[Meller and Moortgat 00] Meller, R, and GK Moortgat (2000): Temperature dependence of the absorption cross sections of formaldehyde between 223 and 323 K in the wavelength range 225-375 nm. *J. Geophys. Res.*, *105*, *D6*, 7089-7101

[Mhin et al 00] Mhin, BJ, WY Chang, JY Lee, KS Kim (2000): Ab Initio Study of Peroxyacetic Nitric Anhydride and Peroxyacetyl Radical: Characteristic Infrared Band of Peroxyacetyl Radical. *J. Phys. Chem.*, *104*, 2613-2617

[Mineshos and Glavas 91] Mineshos, G, and S Glavas (1991): Thermal Decomposition of Peroxypropionyl Nitrate: Kinetics of the Formation of Nitrogenous Products. *React. Kinet. Catal. Lett.*, *45*, *2*, 305-312

[Moortgat 80] Moortgat, GK (1980): Personal communication to E-P Röth, R Ruhnke, G Moortgat, R Meller, and W Schneider. Berichte des Forschungszentrums Jülich, jül-3341, 1997

[Morris and Niki 74] Morris, ED Jr, and H Niki (1974): Reaction of Nitrate Radical with Acetaldehyde and Propylene. *J. Phys. Chem.*, *78*, *13*, 1337-1338

[Neeb et al 98] Neeb, P, O Horie, and GK Moortgat (1998): The Ethene-Ozone Reaction in the Gas Phase. *J. Phys. Chem. A*, *102*, 6778-6785

[Neuroth et al 91] Neuroth, R, H-P Dorn, U Platt (1991): High resolution spectral features of a series of aromatic hydrocarbons and BrO: Potential interferences in atmospheric OH-measurements. *J. Atmos. Chem.*, *12*, *3*, 287-298

[Orphal 03] Orphal, J (2003): A critical review of the absorption cross-sections of O_3 and NO_2 in the ultraviolet and visible. *J. Photochem. Photobio. A*, *157*, 185-209

[Papagni et al 00] Papagni, C, J Arey, and R Atkinson (2000): Rate Constants for the Gas-Phase Reactions of a Series of $C_3 - C_6$ Aldehydes with OH and NO_3 Radicals. *Int. J. Chem. Kinet.*, *32*, *2*, 79-84

[Perner and Platt 79] Perner, D, and U Platt (1979): Detection of Nitrous Acid in the Atmosphere by Differential Optical Absorption. *Geophys. Res. Lett.*, *6*, 917-920

[Pfeilsticker et al 03] Pfeilsticker, K, A Lotter, C Peters, H Bösch (2003): Atmospheric Detection of Water Dimers via Near-Infrared Absorption. *Science*, *300*, 2078-2080

[Platt et al 80] Platt, U, D Perner, AM Winer, GW Harris, and JN Pitts (1980): Detection of NO_3 in the Polluted Troposphere by Differential Optical Absorption. *Geophys. Res. Lett.*, *7*, 89-92

[Platt et al 90] Platt, U, G LeBras, G Poulet, JP Burrows and GK Moortgat (1990): Peroxy radicals from night-time reaction of NO_3 with organic compounds. *Nature*, *348*, *6297*, 147-149

[Platt 00] Platt, U (2000): *Differential Optical Absorption Spectroscopy, Air Monitoring by.* In: Meyers, RA (Ed.), Encyclopedia of Analytical Chemistry, John Wiley & Sons Ltd, Chichester, 1936-1959

[Pope et al 05] Pope, FD, CA Smith, MNR Ashfold, and J Orr-Ewing (2005): High-resolution absorption cross sections of formaldehyde at wavelengths from 313 to 320 nm. *Phys. Chem. Chem. Phys.*, *7*, 79-84

[Press et al 92] Press, WH, SA Teukolsky, WT Vetterling, BP Flannery (1992): *Numerical Recipes in C – The Art of Scientific Computing.* 2^{nd} edition, Cambridge University Press

[Ritz et al 92] Ritz, D, M Hausmann, and U Platt (1992): *An Improved Open Path Multi-Reflection Cell for the Measurement of* NO_2 *and* NO_3. In: Optical Methods in Atmospheric Chemistry, SPIE, 1715, 200-211

[Rodríguez-Bares 03] Rodríguez-Bares, S (2003): *Untersuchungen zur Ozonolyse einfacher Alkene in der Atmosphären-Simulationskammer SAPHIR*. PhD thesis, Universität zu Köln

[Rogers 90] Rogers, JD (1990): Ultraviolet absorption cross sections and atmospheric photodissociation rate constants of formaldehyde. *J. Phys. Chem.*, *94*, 4011-4015

[Rohrer and Brüning 92] Rohrer, F, and D Brüning (1992): Surface NO and NO_2 mixing ratios measured between 30° N and 30° S in the Atlantic region. *J. Atmos. Chem.*, *15 (3-4)*, 253-267

[Rohrer et al 05] Rohrer, F, B Bohn, T Brauers, D Brüning, F-J Johnen, A Wahner, and J Kleffmann (2005): Characterisation of the photolytic HONO-source in the atmosphere simulation chamber SAPHIR. *Atmos. Chem. Phys.*, *5*, 2189-2201

[Rothman et al 05] Rothman, LS, D Jacquemart, A Barbe, D Chris Benner, M Birk, LR Brown, MR Carleer, C Chackerian Jr, K Chance, LH Coudert, V Dana, VM Devi, J-M Flaud, RR Gamache, A Goldman, J-M Hartmann, KW Jucks, AG Maki, J-Y Mandin, ST Massie, J Orphal, A Perrin, CP Rinsland, MAH Smith, J Tennyson, RN Tolchenov, RA Toth, J Vander Auwera, P Varanasi, G Wagner (2005): The HITRAN 2004 molecular spectroscopic database. *J. of Quant. Spec. & Rad. Transfer*, *96*, 139-204

[Sander 86] Sander, SP (1986): Temperature Dependence of the NO_3 Absorption Spectrum. *J. Phys. Chem.*, *90*, 4135-4142

[Saunders et al 03] Saunders, SM, ME Jenkin, RG Derwent, and MJ Pilling (2003): Protocol for the development of the Master Chemical Mechanism, MCMv3 (Part A): tropospheric degradation of non-aromatic volatile organic compounds. *Atmos. Chem. Phys.*, *3*, 161-180

[Schlosser et al 06] Schlosser, E, B Bohn, T Brauers, H-P Dorn, H Fuchs, R Häseler, A Hofzumahaus, F Holland, F Rohrer, LO Rupp, M Siese, R Tillmann, and A Wahner (2006): Intercomparison of Two Hydroxyl Radical Measurement Techniques at the Atmosphere Simulation Chamber SAPHIR. *J. Atmos. Chem.*, submitted

[Schurath and Wipprecht 79] Schurath, U, and V Wipprecht (1979): *Reactions of Peroxiacyl Radicals*. In: 1st European Symposium on Physico-Chemical Behaviour of Atmospheric Pollutants; Versino, B, and H Ott (Eds.), Commission of the European Communities, Brussels, 157-166

[Seefeld and Kerr 97] Seefeld, S, and JA Kerr (1997): Kinetics of the Reactions of Propionylperoxy Radicals with NO and NO_2: Peroxypropionyl Nitrate Formation under Laboratory Conditions Related to the Troposphere. *Env. Sci. Tech.*, *31*, 2949-2953

[Seinfeld and Pandis 97] Seinfeld, JH, and SN Pandis (1997): *Atmospheric Chemistry and Physics. From Air Pollution to Climate Change.* John Wiley & Sons Inc., New York

[Stutz 96] Stutz, J (1996): *Messung der Konzentration troposphärischer Spurenstoffe mittels Differentieller-Optischer-Absorptionsspektroskopie: Eine neue Generation von Geräten und Algorithmen.* PhD thesis, Institut für Umweltphysik, University of Heidelberg

[Stutz and Platt 96] Stutz, J, and U Platt (1996): Numerical analysis and estimation of the statistical error of differential optical absorption spectroscopy measurements with least-squares methods. *Appl. Optics*, *35 (30)*, 6041-6053

[Stutz et al 00] Stutz, J, ES Kim, U Platt, P Bruno, C Perrino, and A Febo (2000): UV-visible absorption cross sections of nitrous acid. *J. Geophys. Res.*, *105*, *D11*, 14585-14592

[Su et al 80] Su, F, JG Calvert, and H Shaw (1980): A FT IR Spectroscopic Study of the Ozone-Ethene Reaction Mechanism in O_2-Rich Mixtures. *J. Phys. Chem.*, *84*, *3*, 239-246

[Tyndall et al 01] Tyndall, GS, RA Cox, C Granier, R Lesclaux, GK Moortgat, MJ Pilling, AR Ravishankara, and TJ Wallington (2001): Atmospheric chemistry of small organic peroxy radicals. *J. Geophys. Res.*, *106*, *D11*, 12157-12182

[Ullerstam et al 00] Ullerstam, M, S Langer, E Ljungström (2000): Gas Phase Rate Coefficients and Activation Energies for the Reaction of Butanal and 2-Methyl-Propanal with Nitrate Radicals. *Inter. J. Chem. Kinet.*, *32*, 294-303

[Veitel 02] Veitel, HJ (2002): *Vertical Profiles of* NO_2 *and* $HONO$ *in the Boundary Layer.* PhD thesis, Institut für Umweltphysik, University of Heidelberg

[Voigt et al 01] Voigt, S, J Orphal, K Bogumil, and JP Burrows (2001): The temperature dependence (203-293 K) of the absorption cross sections of O_3 in the 230 - 850 nm region measured by Fourier-transform spectroscopy. *J. Photochem. Photobio. A*, *143*, 1-9

[Voigt et al 02] Voigt, S, J Orphal, and JP Burrows (2002): The temperature and pressure dependence of the absorption cross-sections of NO_2 in the 250 - 800 nm region measured by Fourier-transform spectroscopy. *J. Photochem. Photobio. A*, *149*, 1-7

[Wayne et al 91] Wayne, RP, I Barnes, P Biggs, JP Burrows, CE Canosa-Mas, J Hjorth, G Le Bras, GK Moortgat, D Perner, G Poulet, G Restelli, and H Sidebottom (1991): The Nitrate Radical: Physics, Chemistry, and the Atmosphere. *Atmos. Env.*, *25A*, *1*, 1-203

[White 42] White, J (1942): Long Optical Paths of Large Aperture. *J. Opt. Soc. Am.*, *32*, 285-288

[White 76] White, J (1976): Very long optical paths in air. *J. Opt. Soc. Am.*, *66*, *5*, 411-416

[Witte et al 86] Witte, F, E Urbanik, C Zetzsch (1986): Temperature-Dependence of the Rate Constants for the Addition of OH to Benzene and to some Monosubstituted Aromatics (Aniline, Bromobenzene, and Nitrobenzene) and the Unimolecular Decay of the Adducts - Kinetics into a Quasi-Equilibrium. *J. Phy. Chem.*, *90*, *14*, 3251-3259

[Zádor et al 05] Zádor, J, V Wagner, K Wirtz, MJ Pilling (2005): Quantitative assessment of uncertainties for a model of tropospheric ethene oxidation using the European Photoreactor (EUPHORE). *Atmos. Env.*, *39*, 2805-2817

Appendix A

The Master Chemical Mechanism v3

The MCM * [Jenkin et al 03, Saunders et al 03] describes the gas-phase degradation of a series of emitted VOCs. Particularly, the formation of O_3 and other secondary pollutants under typical lower tropospheric conditions for integration in photochemical trajectory models is covered. Available information on the kinetics and products of elementary reactions relevant to VOC oxidation is used. Thereby, kinetics and products of reactions, which were not studied so far, were derived from a comparatively small number of similar chemical species utilising analogy and structure-reactivity correlations [Jenkin et al 97]. Given the uncertainties that arise from unconfirmed kinetic data, an atmosphere simulation chamber is especially suited to confirm the predictions made by the model, as neither transport processes nor unknown species interfere with the chemical system [Bloss et al 05, Zádor et al 05]. The MCM is updated regularly. The modules of the MCM are presented here to preserve the mechanism at the time when they were used for calculations in the course of this thesis.

A.1 The Ethene Module

Chemical Reactions with Corresponding Rate Coefficients

The following list shows all reactions with the respective rate coefficients of the ethene module from the MCMv3 in the EASY † format [Brauers and Rohrer 99]. Inorganic reactions are also displayed. A semicolon denotes reactions that were excluded due to missing reactants (eg light) in this particular application. Thus, the extent of the mechanism and the computation time were reduced.

*Data available at *http://mcm.leeds.ac.uk/MCM/*

†Easy AtmoSpheric chemistrY

```
; k[C2H4+NO3-->ETHENO3O2]=CONST(2.10D-16)
; k[CH2OO+NO-->HCHO+NO2]=CONST(1.00D-14)
; k[CH2OO+NO2-->HCHO+NO3]=CONST(1.00D-15)
; k[CH2OO+SO2-->HCHO+SO3]=CONST(7.00D-14)
; k[ETHENO3O-->NO2+HCHO+HCHO]=CONST(7.00D+03)
; k[ETHENO3O-->NO3CH2CHO+HO2]=CONST(KROPRIM*O2)
; k[ETHENO3O2+HO2-->ETHO2HNO3]=CONST(KRO2HO2*0.387)
; k[ETHENO3O2+NO-->ETHENO3O+NO2]=CONST(KRO2NO)
; k[ETHENO3O2+NO3-->ETHENO3O+NO2]=CONST(KRO2NO3)
; k[ETHENO3O2-->ETHENO3O]=CONST(6.00D-13*0.6*RO2)
; k[ETHENO3O2-->ETHOHNO3]=CONST(6.00D-13*0.2*RO2)
; k[ETHENO3O2-->NO3CH2CHO]=CONST(6.00D-13*0.2*RO2)
; k[ETHO2HNO3+OH-->ETHENO3O2]=CONST(1.90D-12*EXP(190/(T)))
; k[ETHO2HNO3+OH-->NO3CH2CHO+OH]=CONST(1.62D-12)
; k[ETHOHNO3+OH-->HOCH2CHO+NO2]=CONST(8.40D-13)
; k[GLYPAN-->HCOCO3+NO2]=CONST(KBPAN)
; k[HCOCH2O-->HCHO+CO+HO2]=CONST(KDEC)
; k[HCOCO3+NO-->HO2+CO+NO2]=CONST(KAPNO)
; k[HCOCO3+NO2-->GLYPAN]=CONST(KFPAN)
; k[HCOCO3+NO3-->HO2+CO+NO2]=CONST(KRO2NO3*1.60)
; k[HO2+NO-->OH+NO2]=CONST(3.60D-12*EXP(270/(T)))
; k[HO2+NO2-->HO2NO2]=CONST(KMT09)
; k[HO2+NO3-->OH+NO2]=CONST(4.00D-12)
; k[HO2NO2-->HO2+NO2]=CONST(KMT10)
; k[HOCH2CH2O2+NO-->ETHOHNO3]=CONST(KRO2NO*0.005)
; k[HOCH2CH2O2+NO-->HOCH2CH2O+NO2]=CONST(KRO2NO*0.995)
; k[HOCH2CH2O2+NO3-->HOCH2CH2O+NO2]=CONST(KRO2NO3)
; k[HOCH2CHO+NO3-->HOCH2CO3+HNO3]=CONST(KNO3AL)
; k[HOCH2CO3+NO-->NO2+HO2+HCHO]=CONST(KAPNO)
; k[HOCH2CO3+NO2-->PHAN]=CONST(KFPAN)
; k[HOCH2CO3+NO3-->NO2+HO2+HCHO]=CONST(KRO2NO3*1.60)
; k[HSO3-->HO2+SO3]=CONST(1.30D-12*EXP(-330/(T))*O2)
; k[N2O5-->NO2+NO3]=CONST( KMT04 )
; k[NO+NO-->NO2+NO2]=CONST(3.30D-39*EXP(530/(T))*O2)
; k[NO+NO3-->NO2+NO2]=CONST(1.80D-11*EXP(110/(T)))
; k[NO+O3-->NO2]=CONST(1.40D-12*EXP(-1310/(T)))
; k[NO2+NO3-->N2O5]=CONST( KMT03 )
; k[NO2+NO3-->NO+NO2]=CONST(4.50D-14*EXP(-1260/(T)))
; k[NO2+O3-->NO3]=CONST(1.40D-13*EXP(-2470/(T)))
; k[NO3+GLYOX-->CO+CO+HO2+HNO3]=CONST(KNO3AL*0.6)
; k[NO3+GLYOX-->HCOCO3+HNO3]=CONST(KNO3AL*0.4)
; k[NO3+HCHO-->HNO3+CO+HO2]=CONST(5.80D-16)
; k[NO3CH2CHO+NO3-->NO3CH2CO3+HNO3]=CONST(KNO3AL)
; k[NO3CH2CHO+OH-->NO3CH2CO3]=CONST(3.40D-12)
; k[NO3CH2CO2H+OH-->HCHO+NO2]=CONST(1.68D-13)
; k[NO3CH2CO3+HO2-->NO3CH2CO2H+O3]=CONST(KAPHO2*0.29)
; k[NO3CH2CO3+HO2-->NO3CH2CO3H]=CONST(KAPHO2*0.71)
; k[NO3CH2CO3+NO-->HCHO+NO2+NO2]=CONST(KAPNO)
; k[NO3CH2CO3+NO2-->NO3CH2PAN]=CONST(KFPAN)
; k[NO3CH2CO3+NO3-->HCHO+NO2+NO2]=CONST(KRO2NO3*1.60)
; k[NO3CH2CO3-->HCHO+NO2]=CONST(1.00D-11*0.7*RO2)
; k[NO3CH2CO3-->NO3CH2CO2H]=CONST(1.00D-11*0.3*RO2)
; k[NO3CH2CO3H+OH-->NO3CH2CO3]=CONST(3.63D-12)
; k[NO3CH2PAN+OH-->HCHO+CO+NO2+NO2]=CONST(1.12D-14)
; k[NO3CH2PAN-->NO3CH2CO3+NO2]=CONST(KBPAN)
; k[O+NO-->NO2]=CONST( KMT01 )
; k[O+NO2-->NO]=CONST(5.50D-12*EXP(188/(T)))
; k[O+NO2-->NO3]=CONST( KMT02 )
; k[O+O3-->]=CONST(8.00D-12*EXP(-2060/(T)))
; k[O+SO2-->SO3]=CONST(4.00D-32*EXP(-1000/(T))*N2)
; k[O-->O3]=CONST(5.60D-34*O2*N2*(((T)/300)@-2.6 + 6.00D-34*O2*O2*(((T)/300)@-2.6)))
; k[O1D-->O]{SUM}=CONST(1.80D-11*N2*EXP(107/(T))+3.20D-11*O2*EXP(67/(T)) )
; k[O1D-->OH+OH]=CONST(2.20D-10*H2O)
; k[OH+GLYPAN-->CO+CO+NO2]=CONST(1.22D-11)
; k[OH+H2-->HO2]=CONST(7.70D-12*EXP(-2100/(T)))
; k[OH+HNO3-->NO3]=CONST(KMT11)
; k[OH+HO2NO2-->NO2]=CONST(1.90D-12*EXP(270/(T)))
; k[OH+HONO-->NO2]=CONST(2.50D-12*EXP(260/(T)))
; k[OH+NO-->HONO]=CONST(KMT07)
; k[OH+NO2-->HNO3]=CONST(KMT08)
; k[OH+NO3-->HO2+NO2]=CONST(2.20D-11)
; k[OH+SO2-->HSO3]=CONST(KMT12)
; k[PHAN+OH-->HCHO+CO+NO2]=CONST(1.12D-12)
; k[PHAN-->HOCH2CO3+NO2]=CONST(KBPAN)
k[C2H4+O3-->HCHO+CH2OOA]=CONST(9.14D-15*EXP(-2580/(T)))
k[C2H4+OH-->HOCH2CH2O2]=CONST(KMT15)
k[CH2OO+CO-->HCHO]=CONST(1.20D-15)
k[CH2OO-->HCHO+H2O2]=CONST(6.00D-18*H2O)
k[CH2OO-->HCOOH]=CONST(1.00D-17*H2O)
k[CH2OOA-->CH2OO]=CONST(KDEC*0.37)
k[CH2OOA-->CO]=CONST(KDEC*0.50)
k[CH2OOA-->HO2+CO+OH]=CONST(KDEC*0.13)
k[ETHGLY+OH-->HOCH2CHO+HO2]=CONST(7.70D-12)
k[HCOCO3+HO2-->HCOCO2H+O3]=CONST(KAPHO2*0.29)
k[HCOCO3+HO2-->HCOCO3H]=CONST(KAPHO2*0.71)
k[HCOCO3-->CO+HO2]=CONST(1.00D-11*0.7*RO2)
k[HCOCO3-->HCOCO2H]=CONST(1.00D-11*0.3*RO2)
k[HCOOH+OH-->HO2]=CONST(4.50D-13)
k[HO2+HO2-->H2O2]=CONST(2.20D-13*KMT06*EXP(600/(T)) + 1.90D-33*M*KMT06*EXP(980/(T)))
k[HO2+O3-->OH]=CONST(2.03D-16*(((T)/300)@4.57*EXP(693/(T))))
k[HOCH2CH2O-->HO2+HCHO+HCHO]=CONST(9.50D+13*EXP(-5988/(T)))
k[HOCH2CH2O-->HO2+HOCH2CHO]=CONST(KROPRIM*O2)
```

```
k[HOCH2CH2O2+HO2-->HYETHO2H]=CONST(2.00D-13*EXP(1250/(T)))
k[HOCH2CH2O2-->ETHGLY]=CONST(2.00D-12*0.2*RO2)
k[HOCH2CH2O2-->HOCH2CH2O]=CONST(2.00D-12*0.6*RO2)
k[HOCH2CH2O2-->HOCH2CHO]=CONST(2.00D-12*0.2*RO2)
k[HOCH2CHO+OH-->GLYOX+HO2]=CONST(1.00D-11*0.200)
k[HOCH2CHO+OH-->HOCH2CO3]=CONST(1.00D-11*0.800)
k[HOCH2CO2H+OH-->HCHO+HO2]=CONST(2.73D-12)
k[HOCH2CO3+HO2-->HOCH2CO2H+O3]=CONST(KAPHO2*0.29)
k[HOCH2CO3+HO2-->HOCH2CO3H]=CONST(KAPHO2*0.71)
k[HOCH2CO3-->HCHO+HO2]=CONST(1.00D-11*0.7*RO2)
k[HOCH2CO3-->HOCH2CO2H]=CONST(1.00D-11*0.3*RO2)
k[HOCH2CO3H+OH-->HOCH2CO3]=CONST(6.19D-12)
k[HYETHO2H+OH-->HOCH2CH2O2]=CONST(1.90D-12*EXP(190/(T)))
k[HYETHO2H+OH-->HOCH2CHO+OH]=CONST(1.38D-11)
k[OH+CO-->HO2+CO2]{APPEND_CO2}=CONST(1.30D-13*KMT05)
k[OH+GLYOX-->CO+CO+HO2]=CONST(1.14D-11*0.6)
k[OH+GLYOX-->HCOCO3]=CONST(1.14D-11*0.4)
k[OH+H2O2-->HO2]=CONST(2.90D-12*EXP(-160/(T)))
k[OH+HCHO-->HO2+CO]=CONST(1.20D-14*(T)*EXP(287/(T)))
k[OH+HCOCO2H-->CO+HO2]=CONST(1.23D-11)
k[OH+HCOCO3H-->HCOCO3]=CONST(1.58D-11)
k[OH+HO2-->]=CONST(4.80D-11*EXP(250/(T)))
k[OH+O3-->HO2]=CONST(1.70D-12*EXP(-940/(T)))
```

Constants and Other Settings

Some more constants and settings of the ethene–ozone model.

```
;KFPAN=COMPRC( 2.70D-28*(T/300)@-7.1*M, 1.20D-11*(T/300)@-0.9, 0.3)
;KBPAN=COMPRC( 4.90D-03*EXP(-12100/T)*M, 5.40D+16*EXP(-13830/T), 0.3)
;KMT01=COMPRC( 1.00D-31*N2*(T/300)@-1.6, 3.00D-11*(T/300)@0.3, 0.85 )
;KMT02=COMPRC( 1.30D-31*N2*(T/300)@-1.5,2.30D-11*(T/200)@0.24, 0.6 )
;KMT03=COMPRC( 3.60D-30*N2*(T/300)@-4.1, 1.90D-12*(T/300)@0.2, 0.35 )
;KMT04=COMPRC( 1.00D-03*N2*(T/300)@-3.5*EXP(-11000/T), 9.70D+14*(T/300)@0.1*EXP (-11080/T),0.35)
KMT05=CONST( 1 + ((0.6*M)/(2.652D+19*(300/T))))
KMT06=CONST(1.+1.4D-21*H2O*EXP(2200/T))
;KMT07=COMPRC( 7.40D-31*N2*(T/300)@-2.4, 3.30D-11*(T/300)@-0.3, EXP(-T/1420))
;KMT08=COMPRC( 3.30D-30*N2*(T/300)@-3.0, 4.10D-11, 0.4 )
;KMT09=COMPRC( 1.80D-31*N2*(T/300)@-3.2,  4.70D-12, 0.6 )
;KMT10=COMPRC( 4.10D-05*N2*EXP(-10650/T), 4.80D+15*EXP(-11170/T), 0.5 )
;KMT11=CONST(2.40D-14*EXP(460/T)
 +(6.50D-34*EXP(1335/T)*M)/(1+(6.50D-34*EXP(1335/T)*M/2.70D-17*EXP(2199/T))))
;KMT12=COMPRC( 4.00D-31*N2*(T/300)@-3.3, 2.00D-12, 0.45)
KMT15=COMPRC( 7.00D-29*(T/300)@-3.1*M, 9.00D-12, 0.48 )
;KRO2NO3=CONST( 2.50D-12 )
;KRO2NO=CONST(2.54D-12*EXP(360/T) )
;KRO2HO2=CONST(2.91D-13*EXP(1300/T) )
KAPHO2=CONST(4.30D-13*EXP(1040/T) )
;KAPNO=CONST(8.10D-12*EXP(270/T))
;KNO3AL=CONST(1.44D-12*EXP(-1862/T))
KDEC=CONST(1.00D+06)
KROPRIM=CONST(6.00D-14*EXP(-550/T) )
```

A.2 The Propanal Module

Chemical Reactions with Corresponding Rate Coefficients

```
; k[HSO3-->HO2+SO3]=CONST(1.30D-12*EXP(-330/(T))*O2)
; k[O+NO-->NO2]=CONST( KMT01 )
; k[O+NO2-->NO]=CONST(5.50D-12*EXP(188/(T)))
; k[O+NO2-->NO3]=CONST( KMT02 )
; k[O+O3-->]=CONST(8.00D-12*EXP(-2060/(T)))
; k[O+SO2-->SO3]=CONST(4.00D-32*EXP(-1000/(T))*N2)
; k[O-->O3]=CONST(5.60D-34*O2*N2*(((T)/300)@-2.6 + 6.00D-34*O2*O2*(((T)/300)@-2.6)))
; k[O1D-->O]{SUM}=CONST(1.80D-11*N2*EXP(107/(T))+3.20D-11*O2*EXP(67/(T)) )
; k[O1D-->OH+OH]=CONST(2.20D-10*H2O)
; k[OH+H2-->HO2]=CONST(7.70D-12*EXP(-2100/(T)))
; k[OH+SO2-->HSO3]=CONST(KMT12)
k[C2H5CHO+NO3-->C2H5CO3+HNO3]=CONST(KNO3AL*2.4)
k[C2H5CHO+OH-->C2H5CO3]=CONST(1.96D-11)
k[C2H5CO3+HO2-->PERPROACID]=CONST(KAPHO2*0.71)
k[C2H5CO3+HO2-->PROPACID+O3]=CONST(KAPHO2*0.29)
k[C2H5CO3+NO-->NO2+C2H5O2]=CONST(KAPNO)
k[C2H5CO3+NO2-->PPN]=CONST(KFPAN)
k[C2H5CO3+NO3-->C2H5O2+NO2]=CONST(KRO2NO3*1.60)
k[C2H5CO3-->C2H5O2]=CONST(1.00D-11*0.7*RO2)
```

```
k[C2H5CO3-->PROPACID]=CONST(1.00D-11*0.3*RO2)
k[C2H5O-->CH3CHO+HO2]=CONST(6.00D-14*EXP(-550/(T))*O2)
k[C2H5O2+HO2-->C2H5OOH]=CONST(2.70D-13*EXP(1000/(T)))
k[C2H5O2+NO-->C2H5NO3]=CONST(2.60D-12*EXP(365/(T))*0.009)
k[C2H5O2+NO-->C2H5O+NO2]=CONST(2.60D-12*EXP(365/(T))*0.991)
k[C2H5O2+NO3-->C2H5O+NO2]=CONST(KRO2NO3)
k[C2H5O2-->C2H5O]=CONST(3.10D-13*0.6*RO2)
k[C2H5O2-->C2H5OH]=CONST(3.10D-13*0.2*RO2)
k[C2H5O2-->CH3CHO]=CONST(3.10D-13*0.2*RO2)
k[C2H5OH+OH-->CH3CHO+HO2]=CONST(6.18D-18*(T)@2*EXP(532/(T))*0.887)
k[C2H5OH+OH-->HOCH2CH2O2]=CONST(6.18D-18*(T)@2*EXP(532/(T))*0.113)
k[CH3CO2H+OH-->CH3O2]=CONST(8.00D-13)
k[CH3CO3+HO2-->CH3CO2H+O3]=CONST(KAPHO2*0.29)
k[CH3CO3+HO2-->CH3CO3H]=CONST(KAPHO2*0.71)
k[CH3CO3+NO-->NO2+CH3O2]=CONST(KAPNO)
k[CH3CO3+NO2-->PAN]=CONST(KFPAN)
k[CH3CO3+NO3-->NO2+CH3O2]=CONST(KRO2NO3*1.60)
k[CH3CO3-->CH3CO2H]=CONST(1.00D-11*0.3*RO2)
k[CH3CO3-->CH3O2]=CONST(1.00D-11*0.7*RO2)
k[CH3CO3H+OH-->CH3CO3]=CONST(3.70D-12)
k[CH3O-->HCHO+HO2]=CONST(7.20D-14*EXP(-1080/(T))*O2)
k[CH3O2+HO2-->CH3OOH]=CONST(3.80D-13*EXP(780/(T)))
k[CH3O2+NO-->CH3NO3]=CONST(3.00D-12*EXP(280/(T))*0.001)
k[CH3O2+NO-->CH3O+NO2]=CONST(3.00D-12*EXP(280/(T))*0.999)
k[CH3O2+NO2-->CH3O2NO2]=CONST(KMT13)
k[CH3O2+NO3-->CH3O+NO2]=CONST(KRO2NO3*0.40)
k[CH3O2-->CH3O]=CONST(1.82D-13*EXP(416/(T))*0.33*RO2)
k[CH3O2-->CH3OH]=CONST(1.82D-13*EXP(416/(T))*0.335*RO2)
k[CH3O2-->HCHO]=CONST(1.82D-13*EXP(416/(T))*0.335*RO2)
k[CH3O2NO2-->CH3O2+NO2]=CONST(KMT14)
k[CH3OH+OH-->HO2+HCHO]=CONST(6.01D-18*(T)@2*EXP(170/(T)))
k[ETHGLY+OH-->HOCH2CHO+HO2]=CONST(7.70D-12)
k[ETHOHNO3+OH-->HOCH2CHO+NO2]=CONST(8.40D-13)
k[GLYPAN-->HCOCO3+NO2]=CONST(KBPAN)
k[HCOCO3+HO2-->HCOCO2H+O3]=CONST(KAPHO2*0.29)
k[HCOCO3+HO2-->HCOCO3H]=CONST(KAPHO2*0.71)
k[HCOCO3+NO-->HO2+CO+NO2]=CONST(KAPNO)
k[HCOCO3+NO2-->GLYPAN]=CONST(KFPAN)
k[HCOCO3+NO3-->HO2+CO+NO2]=CONST(KRO2NO3*1.60)
k[HCOCO3-->CO+HO2]=CONST(1.00D-11*0.7*RO2)
k[HCOCO3-->HCOCO2H]=CONST(1.00D-11*0.3*RO2)
k[HO2+HO2-->H2O2]=CONST(2.20D-13*KMT06*EXP(600/(T)) + 1.90D-33*M*KMT06*EXP(980/(T)))
k[HO2+NO-->OH+NO2]=CONST(3.60D-12*EXP(270/(T)))
k[HO2+NO2-->HO2NO2]=CONST(KMT09)
k[HO2+NO3-->OH+NO2]=CONST(4.00D-12)
k[HO2+O3-->OH]=CONST(2.03D-16*(((T)/300)@4.57*EXP(693/(T))))
k[HO2NO2-->HO2+NO2]=CONST(KMT10)
k[HOCH2CH2O-->HO2+HCHO+HCHO]=CONST(9.50D+13*EXP(-5988/(T)))
k[HOCH2CH2O-->HO2+HOCH2CHO]=CONST(KROPRIM*O2)
k[HOCH2CH2O2+HO2-->HYETHO2H]=CONST(2.00D-13*EXP(1250/(T)))
k[HOCH2CH2O2+NO-->ETHOHNO3]=CONST(KRO2NO*0.005)
k[HOCH2CH2O2+NO-->HOCH2CH2O+NO2]=CONST(KRO2NO*0.995)
k[HOCH2CH2O2+NO3-->HOCH2CH2O+NO2]=CONST(KRO2NO3)
k[HOCH2CH2O2-->ETHGLY]=CONST(2.00D-12*0.2*RO2)
k[HOCH2CH2O2-->HOCH2CH2O]=CONST(2.00D-12*0.6*RO2)
k[HOCH2CH2O2-->HOCH2CHO]=CONST(2.00D-12*0.2*RO2)
k[HOCH2CHO+NO3-->HOCH2CO3+HNO3]=CONST(KNO3AL)
k[HOCH2CHO+OH-->GLYOX+HO2]=CONST(1.00D-11*0.200)
k[HOCH2CHO+OH-->HOCH2CO3]=CONST(1.00D-11*0.800)
k[HOCH2CO2H+OH-->HCHO+HO2]=CONST(2.73D-12)
k[HOCH2CO3+HO2-->HOCH2CO2H+O3]=CONST(KAPHO2*0.29)
k[HOCH2CO3+HO2-->HOCH2CO3H]=CONST(KAPHO2*0.71)
k[HOCH2CO3+NO-->NO2+HO2+HCHO]=CONST(KAPNO)
k[HOCH2CO3+NO2-->PHAN]=CONST(KFPAN)
k[HOCH2CO3+NO3-->NO2+HO2+HCHO]=CONST(KRO2NO3*1.60)
k[HOCH2CO3-->HCHO+HO2]=CONST(1.00D-11*0.7*RO2)
k[HOCH2CO3-->HOCH2CO2H]=CONST(1.00D-11*0.3*RO2)
k[HOCH2CO3H+OH-->HOCH2CO3]=CONST(6.19D-12)
k[HYETHO2H+OH-->HOCH2CH2O2]=CONST(1.90D-12*EXP(190/(T)))
k[HYETHO2H+OH-->HOCH2CHO+OH]=CONST(1.38D-11)
k[N2O5-->NO2+NO3]=CONST( KMT04 )
k[NO+NO-->NO2+NO2]=CONST(3.30D-39*EXP(530/(T))*O2)
k[NO+NO3-->NO2+NO2]=CONST(1.80D-11*EXP(110/(T)))
k[NO+O3-->NO2]=CONST(1.40D-12*EXP(-1310/(T)))
k[NO2+NO3-->N2O5]=CONST( KMT03 )
k[NO2+NO3-->NO+NO2]=CONST(4.50D-14*EXP(-1260/(T)))
k[NO2+O3-->NO3]=CONST(1.40D-13*EXP(-2470/(T)))
k[NO3+CH3CHO-->HNO3+CH3CO3]=CONST(KNO3AL)
k[NO3+GLYOX-->CO+CO+HO2+HNO3]=CONST(KNO3AL*0.6)
k[NO3+GLYOX-->HCOCO3+HNO3]=CONST(KNO3AL*0.4)
k[NO3+HCHO-->HNO3+CO+HO2]=CONST(5.80D-16)
k[OH+C2H5NO3-->CH3CHO+NO2]=CONST(4.40D-14*EXP(720/(T)))
k[OH+C2H5OOH-->C2H5O2]=CONST(1.90D-12*EXP(190/(T)))
k[OH+C2H5OOH-->CH3CHO+OH]=CONST(8.01D-12)
k[OH+CH3CHO-->CH3CO3]=CONST(5.55D-12*EXP(311/(T)))
k[OH+CH3NO3-->HCHO+NO2]=CONST(1.00D-14*EXP(1060/(T)))
k[OH+CH3OOH-->CH3O2]=CONST(1.90D-12*EXP(190/(T)))
k[OH+CH3OOH-->HCHO+OH]=CONST(1.00D-12*EXP(190/(T)))
k[OH+CO-->HO2+CO2]{APPEND_CO2}=CONST(1.30D-13*KMT05)
k[OH+GLYOX-->CO+CO+HO2]=CONST(1.14D-11*0.6)
k[OH+GLYOX-->HCOCO3]=CONST(1.14D-11*0.4)
k[OH+GLYPAN-->CO+CO+NO2]=CONST(1.22D-11)
```

```
k[OH+H2O2-->HO2]=CONST(2.90D-12*EXP(-160/(T)))
k[OH+HCHO-->HO2+CO]=CONST(1.20D-14*(T)*EXP(287/(T)))
k[OH+HCOCO2H-->CO+HO2]=CONST(1.23D-11)
k[OH+HCOCO3H-->HCOCO3]=CONST(1.58D-11)
k[OH+HNO3-->NO3]=CONST(KMT11)
k[OH+HO2-->]=CONST(4.80D-11*EXP(250/(T)))
k[OH+HO2NO2-->NO2]=CONST(1.90D-12*EXP(270/(T)))
k[OH+HONO-->NO2]=CONST(2.50D-12*EXP(260/(T)))
k[OH+NO-->HONO]=CONST(KMT07)
k[OH+NO2-->HNO3]=CONST(KMT08)
k[OH+NO3-->HO2+NO2]=CONST(2.20D-11)
k[OH+O3-->HO2]=CONST(1.70D-12*EXP(-940/(T)))
k[PAN+OH-->HCHO+CO+NO2]=CONST(9.50D-13*EXP(-650/(T)))
k[PAN-->CH3CO3+NO2]=CONST(KBPAN)
k[PERPROACID+OH-->C2H5CO3]=CONST(4.42D-12)
k[PHAN+OH-->HCHO+CO+NO2]=CONST(1.12D-12)
k[PHAN-->HOCH2CO3+NO2]=CONST(KBPAN)
k[PPN+OH-->CH3CHO+CO+NO2]=CONST(1.27D-12)
k[PPN-->C2H5CO3+NO2]=CONST(KBPAN)
k[PROPACID+OH-->C2H5O2]=CONST(1.16D-12)
```

A.3 The Butanal Module

Chemical Reactions with Corresponding Rate Coefficients

```
; k[C2H4+NO3-->ETHENO3O2]=CONST(2.10D-16)
; k[C2H4+O3-->HCHO+CH2OOA]=CONST(9.14D-15*EXP(-2580/(T)))
; k[C2H4+OH-->HOCH2CH2O2]=CONST(KMT15)
; k[CH2OO+CO-->HCHO]=CONST(1.20D-15)
; k[CH2OO+NO-->HCHO+NO2]=CONST(1.00D-14)
; k[CH2OO+NO2-->HCHO+NO3]=CONST(1.00D-15)
; k[CH2OO+SO2-->HCHO+SO3]=CONST(7.00D-14)
; k[CH2OO-->HCHO+H2O2]=CONST(6.00D-18*H2O)
; k[CH2OO-->HCOOH]=CONST(1.00D-17*H2O)
; k[CH2OOA-->CH2OO]=CONST(KDEC*0.37)
; k[CH2OOA-->CO]=CONST(KDEC*0.50)
; k[CH2OOA-->HO2+CO+OH]=CONST(KDEC*0.13)
; k[CH3COCH3+OH-->CH3COCH2O2]=CONST(5.34D-18*(T)@2*EXP(-230/(T)))
; k[ETHENO3O-->NO2+HCHO+HCHO]=CONST(7.00D+03)
; k[ETHENO3O-->NO3CH2CHO+HO2]=CONST(KROPRIM*O2)
; k[ETHENO3O2+HO2-->ETHO2HNO3]=CONST(KRO2HO2*0.387)
; k[ETHENO3O2+NO-->ETHENO3O+NO2]=CONST(KRO2NO)
; k[ETHENO3O2+NO3-->ETHENO3O+NO2]=CONST(KRO2NO3)
; k[ETHENO3O2-->ETHENO3O]=CONST(6.00D-13*0.6*RO2)
; k[ETHENO3O2-->ETHOHNO3]=CONST(6.00D-13*0.2*RO2)
; k[ETHENO3O2-->NO3CH2CHO]=CONST(6.00D-13*0.2*RO2)
; k[ETHO2HNO3+OH-->ETHENO3O2]=CONST(1.90D-12*EXP(190/(T)))
; k[ETHO2HNO3+OH-->NO3CH2CHO+OH]=CONST(1.62D-12)
; k[HCOOH+OH-->HO2]=CONST(4.50D-13)
; k[HSO3-->HO2+SO3]=CONST(1.30D-12*EXP(-330/(T))*O2)
; k[IC3H7O-->CH3COCH3+HO2]=CONST(1.50D-14*EXP(-200/(T))*O2)
; k[IC3H7O2+HO2-->IC3H7OOH]=CONST(KRO2HO2*0.520)
; k[IC3H7O2+NO-->IC3H7NO3]=CONST(2.70D-12*EXP(360/(T))*0.042)
; k[IC3H7O2+NO-->IC3H7O+NO2]=CONST(2.70D-12*EXP(360/(T))*0.958)
; k[IC3H7O2+NO3-->IC3H7O+NO2]=CONST(KRO2NO3)
; k[IC3H7O2-->CH3COCH3]=CONST(4.00D-14*0.2*RO2)
; k[IC3H7O2-->IC3H7O]=CONST(4.00D-14*0.6*RO2)
; k[IC3H7O2-->IPROPOL]=CONST(4.00D-14*0.2*RO2)
; k[IPROPOL+OH-->CH3COCH3+HO2]=CONST(4.06D-18*(T)@2*EXP(788/(T))*0.861)
; k[IPROPOL+OH-->IPROPOLO2]=CONST(4.06D-18*(T)@2*EXP(788/(T))*0.139)
; k[NO3CH2CHO+NO3-->NO3CH2CO3+HNO3]=CONST(KNO3AL)
; k[NO3CH2CHO+OH-->NO3CH2CO3]=CONST(3.40D-12)
; k[NO3CH2CO2H+OH-->HCHO+NO2]=CONST(1.68D-13)
; k[NO3CH2CO3+HO2-->NO3CH2CO2H+O3]=CONST(KAPHO2*0.29)
; k[NO3CH2CO3+HO2-->NO3CH2CO3H]=CONST(KAPHO2*0.71)
; k[NO3CH2CO3+NO-->HCHO+NO2+NO2]=CONST(KAPNO)
; k[NO3CH2CO3+NO2-->NO3CH2PAN]=CONST(KFPAN)
; k[NO3CH2CO3+NO3-->HCHO+NO2+NO2]=CONST(KRO2NO3*1.60)
; k[NO3CH2CO3-->HCHO+NO2]=CONST(1.00D-11*0.7*RO2)
; k[NO3CH2CO3-->NO3CH2CO2H]=CONST(1.00D-11*0.3*RO2)
; k[NO3CH2CO3H+OH-->NO3CH2CO3]=CONST(3.63D-12)
; k[NO3CH2PAN+OH-->HCHO+CO+NO2+NO2]=CONST(1.12D-14)
; k[NO3CH2PAN-->NO3CH2CO3+NO2]=CONST(KBPAN)
; k[O+NO-->NO2]=CONST( KMT01 )
; k[O+NO2-->NO]=CONST(5.50D-12*EXP(188/(T)))
; k[O+NO2-->NO3]=CONST( KMT02 )
; k[O+O3-->]=CONST(8.00D-12*EXP(-2060/(T)))
; k[O+SO2-->SO3]=CONST(4.00D-32*EXP(-1000/(T))*N2)
; k[O-->O3]=CONST(5.60D-34*O2*N2*(((T)/300)@-2.6 + 6.00D-34*O2*O2*(((T)/300)@-2.6)))
; k[O1D-->O]{SUM}=CONST(1.80D-11*N2*EXP(107/(T))+3.20D-11*O2*EXP(67/(T)) )
; k[O1D-->OH+OH]=CONST(2.20D-10*H2O)
; k[OH+H2-->HO2]=CONST(7.70D-12*EXP(-2100/(T)))
; k[OH+IC3H7NO3-->CH3COCH3+NO2]=CONST(4.90D-13)
```

```
; k[OH+IC3H7OOH-->CH3COCH3+OH]=CONST(1.66D-11)
; k[OH+IC3H7OOH-->IC3H7O2]=CONST(1.90D-12*EXP(190/(T)))
; k[OH+SO2-->HSO3]=CONST(KMT12)
k[ACETOL+OH-->MGLYOX+HO2]=CONST(3.00D-12)
k[BUTACID+OH-->NC3H7O2]=CONST(2.40D-12)
k[BUTALNO3+OH-->CO2C3CHO+NO2]=CONST(2.25D-11)
k[BUTALO-->CH3CHO+HCOCH2O2]=CONST(2.70D+14*EXP(-7398/(T)))
k[BUTALO-->CO2C3CHO+HO2]=CONST(KROSEC*O2)
k[BUTALO2+HO2-->BUTALO2H]=CONST(KRO2HO2*0.625)
k[BUTALO2+NO-->BUTALNO3]=CONST(KRO2NO*0.083)
k[BUTALO2+NO-->BUTALO+NO2]=CONST(KRO2NO*0.917)
k[BUTALO2+NO3-->BUTALO+NO2]=CONST(KRO2NO3)
k[BUTALO2-->BUTALO]=CONST(2.50D-13*0.6*RO2)
k[BUTALO2-->CO2C3CHO]=CONST(2.50D-13*0.2*RO2)
k[BUTALO2-->HO2C3CHO]=CONST(2.50D-13*0.2*RO2)
k[BUTALO2H+OH-->BUTALO2]=CONST(1.90D-12*EXP(190/(T)))
k[BUTALO2H+OH-->CO2C3CHO+OH]=CONST(1.27D-10)
k[C2H5CHO+NO3-->C2H5CO3+HNO3]=CONST(KNO3AL*2.4)
k[C2H5CHO+OH-->C2H5CO3]=CONST(1.96D-11)
k[C2H5CO3+HO2-->PERPROACID]=CONST(KAPHO2*0.71)
k[C2H5CO3+HO2-->PROPACID+O3]=CONST(KAPHO2*0.29)
k[C2H5CO3+NO-->NO2+C2H5O2]=CONST(KAPNO)
k[C2H5CO3+NO2-->PPN]=CONST(KFPAN)
k[C2H5CO3+NO3-->C2H5O2+NO2]=CONST(KRO2NO3*1.60)
k[C2H5CO3-->C2H5O2]=CONST(1.00D-11*0.7*RO2)
k[C2H5CO3-->PROPACID]=CONST(1.00D-11*0.3*RO2)
k[C2H5O-->CH3CHO+HO2]=CONST(6.00D-14*EXP(-550/(T))*O2)
k[C2H5O2+HO2-->C2H5OOH]=CONST(2.70D-13*EXP(1000/(T)))
k[C2H5O2+NO-->C2H5NO3]=CONST(2.60D-12*EXP(365/(T))*0.009)
k[C2H5O2+NO-->C2H5O+NO2]=CONST(2.60D-12*EXP(365/(T))*0.991)
k[C2H5O2+NO3-->C2H5O+NO2]=CONST(KRO2NO3)
k[C2H5O2-->C2H5O]=CONST(3.10D-13*0.6*RO2)
k[C2H5O2-->C2H5OH]=CONST(3.10D-13*0.2*RO2)
k[C2H5O2-->CH3CHO]=CONST(3.10D-13*0.2*RO2)
k[C2H5OH+OH-->CH3CHO+HO2]=CONST(6.18D-18*(T)@2*EXP(532/(T))*0.887)
k[C2H5OH+OH-->HOCH2CH2O2]=CONST(6.18D-18*(T)@2*EXP(532/(T))*0.113)
k[C3H7CHO+NO3-->HNO3+C3H7CO3]=CONST(KNO3AL*4.0)
k[C3H7CHO+OH-->BUTALO2]=CONST(5.26D-12*EXP(446/(T))*0.151)
k[C3H7CHO+OH-->C3H7CO3]=CONST(5.26D-12*EXP(446/(T))*0.849)
k[C3H7CO3+HO2-->BUTACID+O3]=CONST(KAPHO2*0.29)
k[C3H7CO3+HO2-->PERBUACID]=CONST(KAPHO2*0.71)
k[C3H7CO3+NO-->NO2+NC3H7O2]=CONST(KAPNO)
k[C3H7CO3+NO2-->PBN]=CONST(KFPAN)
k[C3H7CO3+NO3-->NC3H7O2+NO2]=CONST(KRO2NO3*1.60)
k[C3H7CO3-->BUTACID]=CONST(1.00D-11*0.3*RO2)
k[C3H7CO3-->NC3H7O2]=CONST(1.00D-11*0.7*RO2)
k[C3PAN1-->HOC2H4CO3+NO2]=CONST(KBPAN)
k[C4PAN3-->HO2C3CO3+NO2]=CONST(KBPAN)
k[CH3CHOHCHO+NO3-->CH3CHOHCO3+HNO3]=CONST(KNO3AL*2.4)
k[CH3CHOHCHO+OH-->CH3CHOHCO3]=CONST(2.65D-11)
k[CH3CHOHCO3+HO2-->IPROPOLPER]=CONST(KAPHO2)
k[CH3CHOHCO3+NO-->CH3CHO+HO2+NO2]=CONST(KAPNO)
k[CH3CHOHCO3+NO2-->IPROPOLPAN]=CONST(KFPAN)
k[CH3CHOHCO3+NO3-->CH3CHO+HO2+NO2]=CONST(KRO2NO3*1.60)
k[CH3CHOHCO3-->CH3CHO+HO2]=CONST(1.00D-11*RO2)
k[CH3CO2H+OH-->CH3O2]=CONST(8.00D-13)
k[CH3CO3+HO2-->CH3CO2H+O3]=CONST(KAPHO2*0.29)
k[CH3CO3+HO2-->CH3CO3H]=CONST(KAPHO2*0.71)
k[CH3CO3+NO-->NO2+CH3O2]=CONST(KAPNO)
k[CH3CO3+NO2-->PAN]=CONST(KFPAN)
k[CH3CO3+NO3-->NO2+CH3O2]=CONST(KRO2NO3*1.60)
k[CH3CO3-->CH3CO2H]=CONST(1.00D-11*0.3*RO2)
k[CH3CO3-->CH3O2]=CONST(1.00D-11*0.7*RO2)
k[CH3CO3H+OH-->CH3CO3]=CONST(3.70D-12)
k[CH3COCH2O-->CH3CO3+HCHO]=CONST(KDEC)
k[CH3COCH2O2+HO2-->HYPERACET]=CONST(1.36D-13*EXP(1250/(T)))
k[CH3COCH2O2+NO-->CH3COCH2O+NO2]=CONST(KRO2NO)
k[CH3COCH2O2+NO3-->CH3COCH2O+NO2]=CONST(KRO2NO3)
k[CH3COCH2O2-->ACETOL]=CONST(2.00D-12*0.2*RO2)
k[CH3COCH2O2-->CH3COCH2O]=CONST(2.00D-12*0.6*RO2)
k[CH3COCH2O2-->MGLYOX]=CONST(2.00D-12*0.2*RO2)
k[CH3O-->HCHO+HO2]=CONST(7.20D-14*EXP(-1080/(T))*O2)
k[CH3O2+HO2-->CH3OOH]=CONST(3.80D-13*EXP(780/(T)))
k[CH3O2+NO-->CH3NO3]=CONST(3.00D-12*EXP(280/(T))*0.001)
k[CH3O2+NO-->CH3O+NO2]=CONST(3.00D-12*EXP(280/(T))*0.999)
k[CH3O2+NO2-->CH3O2NO2]=CONST(KMT13)
k[CH3O2+NO3-->CH3O+NO2]=CONST(KRO2NO3*0.40)
k[CH3O2-->CH3O]=CONST(1.82D-13*EXP(416/(T))*0.33*RO2)
k[CH3O2-->CH3OH]=CONST(1.82D-13*EXP(416/(T))*0.335*RO2)
k[CH3O2-->HCHO]=CONST(1.82D-13*EXP(416/(T))*0.335*RO2)
k[CH3O2NO2-->CH3O2+NO2]=CONST(KMT14)
k[CH3OH+OH-->HO2+HCHO]=CONST(6.01D-18*(T)@2*EXP(170/(T)))
k[CO2C3CHO+NO3-->CO2C3CO3+HNO3]=CONST(KNO3AL*4.0)
k[CO2C3CHO+OH-->CO2C3CO3]=CONST(7.15D-11)
k[CO2C3CO3+HO2-->CO2C3CO3H]=CONST(KAPHO2)
k[CO2C3CO3+NO-->CH3COCH2O2+NO2]=CONST(KAPNO)
k[CO2C3CO3+NO2-->CO2C3PAN]=CONST(KFPAN)
k[CO2C3CO3+NO3-->CH3COCH2O2+NO2]=CONST(KRO2NO3*1.60)
k[CO2C3CO3-->CH3COCH2O2]=CONST(1.00D-11*RO2)
k[CO2C3CO3H+OH-->CO2C3CO3]=CONST(4.18D-12)
k[CO2C3PAN+OH-->MGLYOX+CO+NO2]=CONST(5.93D-13)
k[CO2C3PAN-->CO2C3CO3+NO2]=CONST(KBPAN)
```

```
k[ETHGLY+OH-->HOCH2CHO+HO2]=CONST(7.70D-12)
k[ETHOHNO3+OH-->HOCH2CHO+NO2]=CONST(8.40D-13)
k[GLYPAN-->HCOCO3+NO2]=CONST(KBPAN)
k[HCOCH2O-->HCHO+CO+HO2]=CONST(KDEC)
k[HCOCH2O2+HO2-->HCOCH2OOH]=CONST(KRO2HO2*0.387)
k[HCOCH2O2+NO-->NO2+HCOCH2O]=CONST(KRO2NO)
k[HCOCH2O2+NO3-->HCOCH2O+NO2]=CONST(KRO2NO3)
k[HCOCH2O2-->GLYOX]=CONST(2.00D-12*0.2*RO2)
k[HCOCH2O2-->HCOCH2O]=CONST(2.00D-12*0.6*RO2)
k[HCOCH2O2-->HOCH2CHO]=CONST(2.00D-12*0.2*RO2)
k[HCOCH2OOH+OH-->GLYOX+OH]=CONST(2.91D-11)
k[HCOCH2OOH+OH-->HCOCH2O2]=CONST(1.90D-12*EXP(190/(T)))
k[HCOCO3+HO2-->HCOCO2H+O3]=CONST(KAPHO2*0.29)
k[HCOCO3+HO2-->HCOCO3H]=CONST(KAPHO2*0.71)
k[HCOCO3+NO-->HO2+CO+NO2]=CONST(KAPNO)
k[HCOCO3+NO2-->GLYPAN]=CONST(KFPAN)
k[HCOCO3+NO3-->HO2+CO+NO2]=CONST(KRO2NO3*1.60)
k[HCOCO3-->CO+HO2]=CONST(1.00D-11*0.7*RO2)
k[HCOCO3-->HCOCO2H]=CONST(1.00D-11*0.3*RO2)
k[HO1C3O-->HOC2H4CHO+HO2]=CONST(KROPRIM*O2)
k[HO1C3O2+HO2-->HO1C3OOH]=CONST(KRO2HO2*0.520)
k[HO1C3O2+NO-->HO1C3NO3]=CONST(KRO2NO*0.019)
k[HO1C3O2+NO-->HO1C3O+NO2]=CONST(KRO2NO*0.981)
k[HO1C3O2+NO3-->HO1C3O+NO2]=CONST(KRO2NO3)
k[HO1C3O2-->HO1C3O]=CONST(6.00D-13*0.6*RO2)
k[HO1C3O2-->HOC2H4CHO]=CONST(6.00D-13*0.2*RO2)
k[HO1C3O2-->HOC3H6OH]=CONST(6.00D-13*0.2*RO2)
k[HO2+HO2-->H2O2]=CONST(2.20D-13*KMT06*EXP(600/(T)) + 1.90D-33*M*KMT06*EXP(980/(T)))
k[HO2+NO-->OH+NO2]=CONST(3.60D-12*EXP(270/(T)))
k[HO2+NO2-->HO2NO2]=CONST(KMT09)
k[HO2+NO3-->OH+NO2]=CONST(4.00D-12)
k[HO2+O3-->OH]=CONST(2.03D-16*(((T)/300)@4.57*EXP(693/(T))))
k[HO2C3CO3+HO2-->HO2C3CO2H+O3]=CONST(KAPHO2*0.29)
k[HO2C3CO3+HO2-->HO2C3CO3H]=CONST(KAPHO2*0.71)
k[HO2C3CO3+NO-->IPROPOLO2+NO2]=CONST(KAPNO)
k[HO2C3CO3+NO2-->C4PAN3]=CONST(KFPAN)
k[HO2C3CO3+NO3-->IPROPOLO2+NO2]=CONST(KRO2NO3*1.60)
k[HO2C3CO3-->HO2C3CO3H]=CONST(1.00D-11*0.3*RO2)
k[HO2C3CO3-->IPROPOLO2]=CONST(1.00D-11*0.7*RO2)
k[HO2NO2-->HO2+NO2]=CONST(KMT10)
k[HOC2H4CO3+HO2-->HOC2H4CO2H+O3]=CONST(KAPHO2*0.29)
k[HOC2H4CO3+HO2-->HOC2H4CO3H]=CONST(KAPHO2*0.71)
k[HOC2H4CO3+NO-->HOCH2CH2O2+NO2]=CONST(KAPNO)
k[HOC2H4CO3+NO2-->C3PAN1]=CONST(KFPAN)
k[HOC2H4CO3+NO3-->HOCH2CH2O2+NO2]=CONST(KRO2NO3*1.60)
k[HOC2H4CO3-->HOC2H4CO2H]=CONST(1.00D-11*0.3*RO2)
k[HOC2H4CO3-->HOCH2CH2O2]=CONST(1.00D-11*0.7*RO2)
k[HOCH2CH2O-->HO2+HCHO+HCHO]=CONST(9.50D+13*EXP(-5988/(T)))
k[HOCH2CH2O-->HO2+HOCH2CHO]=CONST(KROPRIM*O2)
k[HOCH2CH2O2+HO2-->HYETHO2H]=CONST(2.00D-13*EXP(1250/(T)))
k[HOCH2CH2O2+NO-->ETHOHNO3]=CONST(KRO2NO*0.005)
k[HOCH2CH2O2+NO-->HOCH2CH2O+NO2]=CONST(KRO2NO*0.995)
k[HOCH2CH2O2+NO3-->HOCH2CH2O+NO2]=CONST(KRO2NO3)
k[HOCH2CH2O2-->ETHGLY]=CONST(2.00D-12*0.2*RO2)
k[HOCH2CH2O2-->HOCH2CH2O]=CONST(2.00D-12*0.6*RO2)
k[HOCH2CH2O2-->HOCH2CHO]=CONST(2.00D-12*0.2*RO2)
k[HOCH2CHO+NO3-->HOCH2CO3+HNO3]=CONST(KNO3AL)
k[HOCH2CHO+OH-->GLYOX+HO2]=CONST(1.00D-11*0.200)
k[HOCH2CHO+OH-->HOCH2CO3]=CONST(1.00D-11*0.800)
k[HOCH2CO2H+OH-->HCHO+HO2]=CONST(2.73D-12)
k[HOCH2CO3+HO2-->HOCH2CO2H+O3]=CONST(KAPHO2*0.29)
k[HOCH2CO3+HO2-->HOCH2CO3H]=CONST(KAPHO2*0.71)
k[HOCH2CO3+NO-->NO2+HO2+HCHO]=CONST(KAPNO)
k[HOCH2CO3+NO2-->PHAN]=CONST(KFPAN)
k[HOCH2CO3+NO3-->NO2+HO2+HCHO]=CONST(KRO2NO3*1.60)
k[HOCH2CO3-->HCHO+HO2]=CONST(1.00D-11*0.7*RO2)
k[HOCH2CO3-->HOCH2CO2H]=CONST(1.00D-11*0.3*RO2)
k[HOCH2CO3H+OH-->HOCH2CO3]=CONST(6.19D-12)
k[HYETHO2H+OH-->HOCH2CH2O2]=CONST(1.90D-12*EXP(190/(T)))
k[HYETHO2H+OH-->HOCH2CHO+OH]=CONST(1.38D-11)
k[HYPERACET+OH-->CH3COCH2O2]=CONST(1.90D-12*EXP(190/(T)))
k[HYPERACET+OH-->MGLYOX+OH]=CONST(8.39D-12)
k[HYPROPO-->CH3CHO+HCHO+HO2]=CONST(2.00D+14*EXP(-6410/(T)))
k[HYPROPO2+HO2-->HYPROPO2H]=CONST(KRO2HO2*0.520)
k[HYPROPO2+NO3-->HYPROPO+NO2]=CONST(KRO2NO3)
k[HYPROPO2-->ACETOL]=CONST(8.80D-13*0.2*RO2)
k[HYPROPO2-->HYPROPO]=CONST(8.80D-13*0.6*RO2)
k[HYPROPO2-->PROPGLY]=CONST(8.80D-13*0.2*RO2)
k[HYPROPO2H+OH-->ACETOL+OH]=CONST(2.44D-11)
k[HYPROPO2H+OH-->HYPROPO2]=CONST(1.90D-12*EXP(190/(T)))
k[IPROPOLO-->CH3CHO+HCHO+HO2]=CONST(2.00D+14*EXP(-5505/(T)))
k[IPROPOLO2+HO2-->IPROPOLO2H]=CONST(KRO2HO2*0.520)
k[IPROPOLO2+NO-->IPROPOLO+NO2]=CONST(KRO2NO*0.991)
k[IPROPOLO2+NO-->PROLNO3]=CONST(KRO2NO*0.009)
k[IPROPOLO2+NO3-->IPROPOLO+NO2]=CONST(KRO2NO3)
k[IPROPOLO2-->CH3CHOHCHO]=CONST(2.00D-12*0.2*RO2)
k[IPROPOLO2-->IPROPOLO]=CONST(2.00D-12*0.6*RO2)
k[IPROPOLO2-->PROPGLY]=CONST(2.00D-12*0.2*RO2)
k[IPROPOLO2H+OH-->CH3CHOHCHO+OH]=CONST(1.83D-11)
k[IPROPOLO2H+OH-->IPROPOLO2]=CONST(1.90D-12*EXP(190/(T)))
k[IPROPOLPAN+OH-->CH3CHO+CO+NO2]=CONST(2.34D-12)
k[IPROPOLPAN-->CH3CHOHCO3+NO2]=CONST(KBPAN)
```

```
k[IPROPOLPER+OH-->CH3CHOHCO3]=CONST(9.34D-12)
k[N2O5-->NO2+NO3]=CONST( KMT04 )
k[NC3H7O-->C2H5CHO+HO2]=CONST(KROPRIM*O2)
k[NC3H7O2+HO2-->NC3H7OOH]=CONST(KRO2HO2*0.520)
k[NC3H7O2+NO-->NC3H7NO3]=CONST(2.80D-12*EXP(360/(T))*0.020)
k[NC3H7O2+NO-->NC3H7O+NO2]=CONST(2.80D-12*EXP(360/(T))*0.980)
k[NC3H7O2+NO3-->NC3H7O+NO2]=CONST(KRO2NO3)
k[NC3H7O2-->C2H5CHO]=CONST(6.00D-13*0.2*RO2)
k[NC3H7O2-->NC3H7O]=CONST(6.00D-13*0.6*RO2)
k[NC3H7O2-->NPROPOL]=CONST(6.00D-13*0.2*RO2)
k[NO+HYPROPO2-->HYPROPO+NO2]=CONST(KRO2NO*0.977)
k[NO+HYPROPO2-->PROPOLNO3]=CONST(KRO2NO*0.023)
k[NO+NO-->NO2+NO2]=CONST(3.30D-39*EXP(530/(T))*O2)
k[NO+NO3-->NO2+NO2]=CONST(1.80D-11*EXP(110/(T)))
k[NO+O3-->NO2]=CONST(1.40D-12*EXP(-1310/(T)))
k[NO2+NO3-->N2O5]=CONST( KMT03 )
k[NO2+NO3-->NO+NO2]=CONST(4.50D-14*EXP(-1260/(T)))
k[NO2+O3-->NO3]=CONST(1.40D-13*EXP(-2470/(T)))
k[NO3+CH3CHO-->HNO3+CH3CO3]=CONST(KNO3AL)
k[NO3+GLYOX-->CO+CO+HO2+HNO3]=CONST(KNO3AL*0.6)
k[NO3+GLYOX-->HCOCO3+HNO3]=CONST(KNO3AL*0.4)
k[NO3+HCHO-->HNO3+CO+HO2]=CONST(5.80D-16)
k[NO3+HO2C3CHO-->HO2C3CO3+HNO3]=CONST(KNO3AL*4.0)
k[NO3+HOC2H4CHO-->HOC2H4CO3+HNO3]=CONST(KNO3AL*2.4)
k[NO3+MGLYOX-->CH3CO3+CO+HNO3]=CONST(KNO3AL*2.4)
k[NPROPOL+OH-->C2H5CHO+HO2]=CONST(5.53D-12*0.494)
k[NPROPOL+OH-->HO1C3O2]=CONST(5.53D-12*0.063)
k[NPROPOL+OH-->HYPROPO2]=CONST(5.53D-12*0.443)
k[OH+C2H5NO3-->CH3CHO+NO2]=CONST(4.40D-14*EXP(720/(T)))
k[OH+C2H5OOH-->C2H5O2]=CONST(1.90D-12*EXP(190/(T)))
k[OH+C2H5OOH-->CH3CHO+OH]=CONST(8.01D-12)
k[OH+C3PAN1-->HOCH2CHO+CO+NO2]=CONST(4.51D-12)
k[OH+C4PAN3-->CH3CHOHCHO+CO+NO2]=CONST(9.00D-12)
k[OH+CH3CHO-->CH3CO3]=CONST(5.55D-12*EXP(311/(T)))
k[OH+CH3NO3-->HCHO+NO2]=CONST(1.00D-14*EXP(1060/(T)))
k[OH+CH3OOH-->CH3O2]=CONST(1.90D-12*EXP(190/(T)))
k[OH+CH3OOH-->HCHO+OH]=CONST(1.00D-12*EXP(190/(T)))
k[OH+CO-->HO2+CO2]{APPEND_CO2}=CONST(1.30D-13*KMT05)
k[OH+GLYOX-->CO+CO+HO2]=CONST(1.14D-11*0.6)
k[OH+GLYOX-->HCOCO3]=CONST(1.14D-11*0.4)
k[OH+GLYPAN-->CO+CO+NO2]=CONST(1.22D-11)
k[OH+H2O2-->HO2]=CONST(2.90D-12*EXP(-160/(T)))
k[OH+HCHO-->HO2+CO]=CONST(1.20D-14*(T)*EXP(287/(T)))
k[OH+HCOCO2H-->CO+HO2]=CONST(1.23D-11)
k[OH+HCOCO3H-->HCOCO3]=CONST(1.58D-11)
k[OH+HNO3-->NO3]=CONST(KMT11)
k[OH+HO1C3NO3-->HOC2H4CHO+NO2]=CONST(4.44D-12)
k[OH+HO1C3OOH-->HO1C3O2]=CONST(1.90D-12*EXP(190/(T)))
k[OH+HO1C3OOH-->HOC2H4CHO+OH]=CONST(1.52D-11)
k[OH+HO2-->]=CONST(4.80D-11*EXP(250/(T)))
k[OH+HO2C3CHO-->CO2C3CHO+HO2]=CONST(4.88D-11*0.561)
k[OH+HO2C3CHO-->HO2C3CO3]=CONST(4.88D-11*0.439)
k[OH+HO2C3CO2H-->IPROPOLO2]=CONST(2.78D-11)
k[OH+HO2C3CO3H-->HO2C3CO3]=CONST(3.12D-11)
k[OH+HO2NO2-->NO2]=CONST(1.90D-12*EXP(270/(T)))
k[OH+HOC2H4CHO-->HOC2H4CO3]=CONST(3.06D-11)
k[OH+HOC2H4CO2H-->HOCH2CH2O2]=CONST(1.39D-11)
k[OH+HOC2H4CO3H-->HOC2H4CO3]=CONST(1.73D-11)
k[OH+HOC3H6OH-->HOC2H4CHO+HO2]=CONST(9.73D-12)
k[OH+HONO-->NO2]=CONST(2.50D-12*EXP(260/(T)))
k[OH+MGLYOX-->CH3CO3+CO]=CONST(1.72D-11)
k[OH+NC3H7NO3-->C2H5CHO+NO2]=CONST(7.30D-13)
k[OH+NC3H7OOH-->C2H5CHO+OH]=CONST(1.10D-11)
k[OH+NC3H7OOH-->NC3H7O2]=CONST(1.90D-12*EXP(190/(T)))
k[OH+NO-->HONO]=CONST(KMT07)
k[OH+NO2-->HNO3]=CONST(KMT08)
k[OH+NO3-->HO2+NO2]=CONST(2.20D-11)
k[OH+O3-->HO2]=CONST(1.70D-12*EXP(-940/(T)))
k[PAN+OH-->HCHO+CO+NO2]=CONST(9.50D-13*EXP(-650/(T)))
k[PAN-->CH3CO3+NO2]=CONST(KBPAN)
k[PBN+OH-->C2H5CHO+CO+NO2]=CONST(4.70D-12)
k[PBN-->C3H7CO3+NO2]=CONST(KBPAN)
k[PERBUACID+OH-->C3H7CO3]=CONST(8.29D-12)
k[PERPROACID+OH-->C2H5CO3]=CONST(4.42D-12)
k[PHAN+OH-->HCHO+CO+NO2]=CONST(1.12D-12)
k[PHAN-->HOCH2CO3+NO2]=CONST(KBPAN)
k[PPN+OH-->CH3CHO+CO+NO2]=CONST(1.27D-12)
k[PPN-->C2H5CO3+NO2]=CONST(KBPAN)
k[PROLNO3+OH-->CH3CHOHCHO+NO2]=CONST(1.71D-12)
k[PROPACID+OH-->C2H5O2]=CONST(1.16D-12)
k[PROPGLY+OH-->ACETOL+HO2]=CONST(1.20D-11*0.613)
k[PROPGLY+OH-->CH3CHOHCHO+HO2]=CONST(1.20D-11*0.387)
k[PROPOLNO3+OH-->ACETOL+NO2]=CONST(9.16D-13)
```

Appendix B

The FFT De-Convolution Method

Every spectroscopic device has an instrumental line shape function I of finite width. When a spectrum is recorded, the initially very narrow natural line width is convolved with I. In intensity space the absorption is represented by an exponential factor, as was shown in equation (2.5). Assuming weak absorption the spectrum is convolved directly in $\log(Intensity)$ space. Two different but finite resolution functions are adapted by calculating an effective function, which is then applied to the cross section to degrade its resolution. Thereby, FFT methods are used for the sake of simplicity and brevity.

$$\sigma_{\text{literature}} = \sigma_{\text{real}} \otimes I_{\text{literature}} \tag{B.1a}$$

$$\sigma_{\text{device}} = \sigma_{\text{real}} \otimes I_{\text{device}} \tag{B.1b}$$

The subscripts literature, real and device stand for reported, natural and measured data, respectively. A convolution turns to a simple multiplication when Fourier transformed. The Fourier operator here is denoted as $\mathcal{F}$.

$$\mathcal{F}(\sigma_{\text{literature}}) = \mathcal{F}(\sigma_{\text{real}}) \times \mathcal{F}(I_{\text{literature}}) \tag{B.2a}$$

$$\mathcal{F}(\sigma_{\text{device}}) = \mathcal{F}(\sigma_{\text{real}}) \times \mathcal{F}(I_{\text{device}}) \tag{B.2b}$$

Dividing the two equations (B.2a) and (B.2b) and re-arranging the quotient towards $\mathcal{F}(\sigma_{\text{device}})$ cancels σ_{real} and gives

$$\mathcal{F}(\sigma_{\text{device}}) = \frac{\mathcal{F}(I_{\text{device}})}{\mathcal{F}(I_{\text{literature}})} \times \mathcal{F}(\sigma_{\text{literature}}) \tag{B.3}$$

Applying the inverse Fourier transform makes finally

$$\sigma_{\text{device}} = \mathcal{F}^{-1}\left(\frac{\mathcal{F}(I_{\text{device}})}{\mathcal{F}(I_{\text{literature}})} \times \mathcal{F}(\sigma_{\text{literature}})\right) \tag{B.4}$$

The instrumental line shape function, $I_{\mathrm{literature}}$, must be known. In practice, all input data are interpolated on a wavelength grid of 10 nm using a cubic spline method. The boundaries of the data are expanded by zero values in order to avoid numerical errors within the Fourier transformation.

Appendix C

Formaldehyde

C.1 Conversion: Solid to Gas-Phase

The molecular weight of para-formaldehyde is stated as 30.03 amu. The atomic mass unit is 1.66×10^{-24} g. Assuming 100 % conversion the number of molecules, N, in the gas-phase is

$$N = \frac{W \times 10^{-3}}{30.03 \times 1.66 \times 10^{-24}} \tag{C.1}$$

where W is the weight of the sample in mg. The chamber volume is given as 270 m^3 = 2.7×10^8 cm^3. Turning the number of molecules into a number density leads to

$$[\mathrm{HCHO}](SAPHIR) = W \times 7.43 \times 10^{10}\ \mathrm{cm}^{-3} \tag{C.2}$$

Thus, 1 mg of para-formaldehyde corresponds to about 3 ppbv in the chamber. This result features the precision of the scales (0.05 mg), the relative accuracy of the chamber volume (3 %) and the purity of the solid para-formaldehyde (5 %). As the error of the scales can be neglected in most cases, the accuracy of the HCHO injection turns out as 6 %.

C.2 A Comparison of UV Absorption Cross Sections

Spectroscopic methods use the optical absorption features of a molecule to identify and quantify a compound. These are represented by the absorption cross section, which is a fundamental property of every absorber. The HCHO absorption cross section has been investigated several times in the past thirty years, with varying quality and, very important for spectroscopic methods, at different resolutions. However, absolute absorption cross sections of HCHO are difficult to obtain, as its experimental application is complicated due to polymerisation and wall adsorption effects. Seven reported cross sections are reviewed in this section. The cross sections were referenced against the one currently recommended by IUPAC * [Meller and Moortgat 00]. The comparison covered the wavelength range from 305 to 350 nm, since it contains the most prominent and strongest absorption structures and is therefore used in the spectral retrieval of HCHO. All cross sections were degraded to a resolution of 0.2 nm assuming a Gaussian line shape and considering initial finite resolutions. During convolution the cross sections were also interpolated to a common wavelength grid of 0.04 nm to provide comparability. A non-linear least squares fit of the *Meller and Moortgat* [00] differential absorption cross section, obtained by high-pass-filtering, was performed applying a scaling factor and a shift as parameters. Furthermore, a polynomial of second order was included in the fitting procedure to allow for baseline drifts. Some of the cross sections were reported in vacuum wavelengths [Bogumil et al 03, Cantrell et al 90, Rogers 90], others in air wavelengths [Meller and Moortgat 00]. The wavelength calibration was converted into air wavelengths when necessary. Results are shown in Table C.1.
Slight misalignments of the wavelength calibration are encountered within the cross section by *Cantrell et al* [90]. Apart from that, the wavelength calibration was consistent in that interval. The scaling of the differential absorption cross section tended to be lower in the past, with the highest being the highly resolved and recently published cross section by *Pope et al* [05]. Considering the variance of all published cross sections excluding that by *Bass et al* [80], which stands further out from the others, the HCHO cross section is known within 35 %, although accuracies stated in individual publications (eg 2 % given by *Rogers* [90]) are much smaller than that. However, assuming that measurement and HCHO preparation techniques have been improved with time and only the cross sections of the last five years are considered [Bogumil et al 03, Meller and Moortgat 00, Pope et al 05], an overall discrepancy of 9 % remains.

*International Union of Pure and Applied Chemistry [IUPAC 05]

Table C.1: *Comparison of adapted UV absorption cross sections of HCHO in the wavelength range from 305 to 350 nm against the one by* Meller and Moortgat *[00]. All cross sections were degraded to a resolution of 0.2 nm.*

REFERENCE	T [K]	FWHM [a] [nm]	FACTOR [b]	SHIFT [c] [nm]
[Pope et al 05] [d]	293	0.006	1.08	$\pm$0.00
[Bogumil et al 03]	293	0.11	0.99	$\pm$0.00
[Meller and Moortgat 00]	298	0.04	–	–
[Cantrell et al 90]	293	0.011	0.91	$+$0.11
[Rogers 90]	296	0.016	0.80	$-$0.04
[Bass et al 80]	296	0.025	0.53	$-$0.03
[Moortgat 80]	285	0.08	0.80	$\pm$0.00

[a] Full width at half maximum resolution as stated in the reference
[b] σ'(Reference) = Factor $\times$ σ'([Meller and Moortgat 00])
[c] Shift of σ'([Meller and Moortgat 00]) with respect to reference
[d] Cross section available only from 313 to 320 nm

C.3 Correction for the Temperature Dependence

A differential absorption cross section be temperature dependent featuring a scaling factor f between the two temperatures T_1 and T_2.

$$\sigma'(T_1) = f \times \sigma'(T_2) \tag{C.3}$$

Under these conditions the correct concentration is extracted from the measured spectrum only, when the temperatures, at which the measurement was done and the absorption cross section was determined, agree.

$$C(T_1) = \frac{\tau'(T_1)}{\sigma'(T_1) \times L} \tag{C.4}$$

However, evaluating spectra measured at T_1 using a cross section measured at T_2 scales the correct result for T_1 by a factor of f^{-1}.

$$C' = \frac{\tau'(T_1)}{\sigma'(T_2) \times L} = \frac{\tau'(T_1)}{f \times \sigma'(T_1) \times L} = f^{-1} \times C(T_1) \tag{C.5}$$

For HCHO f results in 0.99 [Meller and Moortgat 00] and 0.93 [Cantrell et al 90] at 0.2 nm FWHM for $T_2 - T_1$ = 25° C. That is, concentrations from spectra measured at low T (eg 273 K) evaluated with a high T cross section (eg 298 K) have to be downscaled by 1 or 7 %, respectively.

Date	Type	*T* [K]	H_2O [mbar]	O_3 [ppbv]	NO_X [ppbv]	hν	HCHO [ppbv]	CO	Others
2004									
3 Jun	NO_2 comparison	286-293	0.8	0-14	0-43	temporarily	/	no	/
16 Jun	HONO comparison	289-298	7-21	0-11	0-22	yes			
6 Jul	HCHO comparison	291-297	0.6	0	0.1	no	0-33		
10 Aug		296-299	dry				0-8		
11 Aug	O_3 comparison	296-304		0-60	0.04		0.4		
2005									
24 Jan	OVOC comparison	275-279	0-6	0-54	0	no	0	no	/
25 Jan		274-276	0.5	0-1			/		Benzaldehyde Toluene other OVOCs
26 Jan		274-278	0-6	0			/		
27 Jan		274-276	0-5	0-50			0-4		
28 Jan		275-278	3-5	0	0-40		0-3		
14 Feb	HCHO yield from ethene ozonolysis	277-279	0.4	0-120	0.1	no	0.1	no	Ethane Propane
15 Feb		274-277			0		0-9		Ethene Propane
16 Feb		273-276					0-15		/
17 Feb		274-277					0-10	yes	Ethene Propane
18 Feb		273-278	dry	50-75			10-12		
7 Apr	H_2O comparison	281-289	0-1	1	/	temporarily	/	no	/
8 Apr		279-282	0-7			no			
23 Jul	HOxCOMP comparison	289-297	0-11	0-28	0-1	yes	0-4	no	Benzene m-Xylene other VOCs
29 Aug	NO_3 + Benzalde-hyde	296-303	dry	0-120	0-10	no	/	no	Benzaldehyde
31 Aug	Dry $\tau(NO_3)$	296-305		5000	/				/
6 Sep	NO_3 + C_2-C_4 aldehyde	295-304		0-150	0-10			yes	Ethanal
7 Sep		295-304							Propanal
8 Sep		297-303			0-13				Butanal

Forschungszentrum Jülich
in der Helmholtz-Gemeinschaft

Jül-4218
Mai 2006
ISSN 0944-2952